ALMA MATER STUDIORUM · UNIVERSITY OF BOLOGNA

School of Science
Department of Physics and Astronomy
Master Degree in Physics

Direct Detection of Dark Matter through Electronic Recoil: Theory and Simulations

Supervisor: Submitted by:
Prof. Fabio Maltoni   Gian Marco Lucchetti

Co-supervisor:
Dr. Chiara Arina

Academic Year 2021/2022

The most exciting phrase to hear in science, the one that heralds the most discoveries, is not "Eureka!" (I found it!) but "That's funny ..."

Isaac Asimov

Abstract

Revealing the nature of dark matter (DM) is among the most puzzling issues of today's particle physics, astrophysics and cosmology. Given the striking pieces of evidence for DM at all astrophysical scales, starting from galactic and going to cosmological scales, a widespread and well-motivated assumption on the nature of the DM is that it is made by a new particle that extends the Standard Model (SM) of particle physics content. Direct detection of DM is a crucial probe to look for DM interactions with SM particles by searching for nuclear recoils generated by the elastic scattering of DM particles in Earth-based underground detectors. If such a signal is measured, it could provide insights into the underlying particle physics model and the DM mass scale. More precisely, usual direct detection methods are mostly sensitive to DM masses above 6 GeV, with a maximum of sensitivity around 50-100 GeV. Below 6 GeV, the signal produced by the nuclear recoil is below the experimental threshold. In the past few years, a new detection method has attracted a lot of attention: the search for electronic recoils that can be induced by light DM particles, around the GeV or sub-GeV scale. In this master thesis project, we will focus on developing the phenomenology of electronic recoils induced by DM particles. The main scope is to implement such signal within the MADDM package, which is so far capable of computing nuclear recoils for generic DM models.

We consider a specific class of electronic recoils, namely ionization signals, that arise in dual-phase liquid/gas detectors like XENON1T. Following the same procedure employed for coding the nuclear recoil signal, we will implement the dominant interaction term of electronic recoil rate for spin 0 and spin 1/2 DM particles. There are several building blocks needed to achieve the automatic computation of the scattering rate. The first step is the computation of the scattering matrix element square: it requires the building of simplified DM electron models as well as models with four-fermion interactions in FeynRules and the generation of UFO files for all models, as MADDM takes those as input files. At the MADDM level, these files are then read to generate the elastic scattering amplitudes for the simplified and effective models and take the interference term in such a way to single out the dominant DM-electron scattering term. The second step is to embed the electron, which is supposed to be free in the previous calculation, into the atom: this is achieved by encoding the ionization form factor for the xenon atom.

Finally, the expected rate in the XENON1T detector can be computed by encoding

its likelihood. This is the first time that the functionality of predicting the electronic recoils for generic high energy DM models in the UFO format will be made public in a numerical tool such as MADDM. The user is able to compute the expected DM electron rate for his/her favourite model and set automatically bounds on light DM from direct detection searches. We proceed further on this thesis by categorizing and implementing all possible dominant terms describing the scattering of a DM particle of spin 0 or 1/2 and an electron. In the last chapter we describe a scalar dark QED model, and we make constraints on its parameters using the new MADDM extension.

Contents

Chapter 1

Current State of Art of DM

1.1 Evidences of DM

DM is one of the biggest mysteries in modern physics. Even with the most advanced technologies and precise machines humanity has been able to build, DM has always found a way to elude us. But DM is not a new topic; it has been around for many decades. It was studied even by Lord Kelvin, who made an estimation of the mass of the Milky Way from the measurements of the velocity dispersion of visible stars. In a talk given in 1884, he stated: "Many of our supposed thousand million stars, perhaps a great majority of them, may be dark bodies" [1]. In this chapter, we will briefly review the current knowledge about DM, showing the constraints placed on its properties from cosmology and astrophysics and presenting the role DM plays in theories beyond the Standard Model (BSM).

1.1.1 Galaxies rotation curves

The problem of DM started in the 20th Century, when astronomers calculated with high precision the total mass of galaxies and galaxy clusters by using dynamics and their understanding of gravity, and then compared this total mass with the amount of luminous matter belonging to the studied system: this is known as the *mass-to-light ratio*. Even if more accurate methods were used, the mass-to-light ratio still showed that something "dark" must exist inside galaxies [2, 3]. After a considerable amount of time, advancements in radio astronomy and spectroscopy made it feasible to obtain accurate calculations of stars and neutral hydrogen rotational rates, which displayed obvious indications that the matter distribution in galaxies was not consistent with the luminous matter [4, 5]. Entities located in the outer regions of spiral galaxies revolve around a central point, with a circular velocity denoted as v_c. According to Newtonian gravity, this is given by

$$v_c^2(r) = \frac{M(r)G}{r}, \tag{1.1}$$

where G is the gravitational constant and $M(r)$ represents the mass enclosed within a distance r from the galactic centre. The mass distribution is assumed to be spherically symmetric, such that

$$M(r) = \int_0^r 4\pi r'^2 \rho(r') \, dr', \tag{1.2}$$

where ρ is the matter density. Astronomers used the rotation curve, which shows the measured velocity v_c of objects at different distances, to infer the mass distribution of a galaxy. For many galaxies, the rotation curve is observed to be approximately flat at large distances, far beyond where the majority of stars are located, indicating a constant circular velocity $v_c(r) = \text{const.}$, as illustrated in Fig. 1.1.
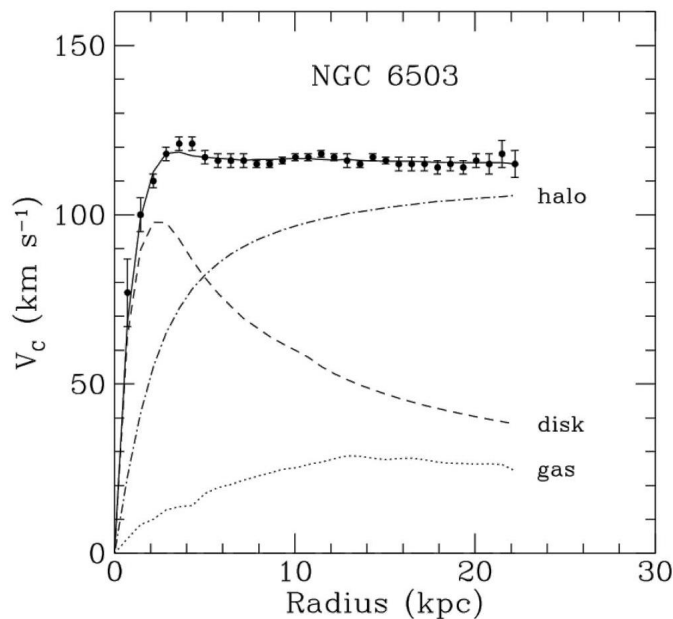
Figure 1.1: Rotation curve for the NGC 6503 galaxy. Also shown is the predicted rotation curve from different components of the galaxy. Figure from Ref. [12].

This implies a mass density given by

$$\rho(r) = \frac{\text{const.}^2}{4\pi G r^2}, \tag{1.3}$$

which has no luminous counterpart in either gaseous or stellar matter. The assumption of spherical symmetry, used to derive this equation, is a good first approximation for the mass distribution of galaxies.

The development of N-body simulations provided further evidence for the existence of a large symmetrical structure in galaxies, known as the DM halo [6–8]. These simulations showed that rotating spiral galaxies would be unstable without the addition of a DM halo. The amount of non-luminous matter in galaxies was uncertain, but many mass-to-light ratios were reported between $3-10$ [9], highlighting the need for a significant amount of DM.

Another solution to the missing mass problem is the Modified Newtonian Dynamics (MOND) [10, 11], which affects small acceleration scales. Although initially introduced as a phenomenological model, researchers have attempted to incorporate MOND into a more fundamental theoretical framework. However, the initial formulation of MOND was non-relativistic and therefore inconsistent with General Relativity (GR).

The phenomenon of gravitational lensing, where the light from distant stars is bent by a massive object, is one of the successful predictions of GR. By using this phenomenon, the total mass of the foreground galaxy or cluster can be determined and compared with the luminous matter measured in the object [12]. However, modified gravity theories, such as TeVeS (Tensor-Vector-Scalar gravity [13]), struggle to reproduce the gas density distributions found in galaxy clusters, especially during cluster mergers [14]. For instance, the Bullet Cluster collision shows a discrepancy between gravitational lensing and X-ray astronomy observations; while lensing shows that the two clusters passed through each other unaffected, X-ray images depict a violent collision. We can see the difference between the two measurements in Fig. 1.2
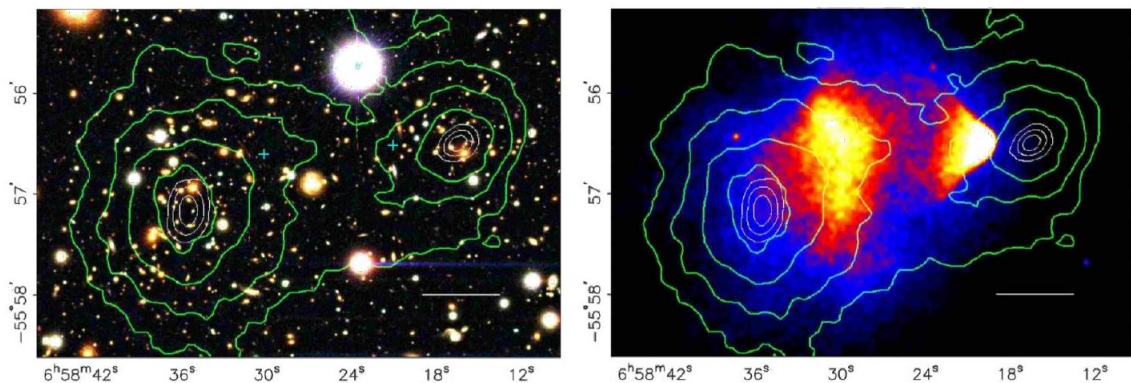
Figure 1.2: Collision of the bullet cluster. The left side shows stellar matter, while the right side displays the distribution of hot gas observed through X-rays and represented by a range of colours. The green outlines illustrate the density of matter determined by gravitational lensing. It is evident that most of the mass in the clusters passes through each other without any impact. Figure from Ref. [15].

With more and more studies of cluster mergers [16] it became clear that the TeVeS approach was not the right one.

MACHOs (massive astronomical compact halo objects) have been suggested as another possible explanation for these phenomena, and experimental studies searching for micro-lensing effects were conducted [17, 18]. Those studies constrained MACHOs in the mass range 10^{-7} to 1 M_{sun}, and conclude that this type of MACHOs constitutes about the 8% of DM halo mass, therefore the DM mystery still was not solved. Fortunately, it is possible to get stronger evidences for DM by studying the Big Bang Cosmology.

1.1.2 Cosmological evidences for DM

The existence of DM also plays a crucial role in the evolution of the Universe. This phenomenon can be inferred for instance by using Hubble's law and by analysing the Cosmic Microwave Background (CMB).

The Universe that we observe today is both homogeneous and isotropic at very large scales ($>$Mpc[1]). We refer to this fact as Cosmological Principle [19]. In this assumption, it is possible to solve the Einstein's field equations, obtaining the Friedman-Lemaître-Robertson-Walker (FLRW) metric:

$$ds^2 = dt^2 - a^2(t)\left(\frac{dr^2}{1-kr^2} + r^2 d\theta^2 + r^2 \sin^2\theta d\phi^2\right). \tag{1.4}$$

The term $a(t)$ is a scale factor, and $a(t_0) = 1$, where t_0 is the present time. The term k is the curvature, which is > 0, 0 or < 0 for respectively a closed, flat or open Universe. We can define the Hubble parameter as

$$H(t) = \frac{\dot{a}}{a}, \tag{1.5}$$

that is frequently expressed in terms of the dimensionless parameter $h(t)$, which is defined as

$$h(t) = \frac{H(t)}{100 \text{ km s}^{-1}\text{Mpc}^{-1}}. \tag{1.6}$$

Substituting the FLRW metric into Einstein's field equation, and considering the time-component, we obtain the Friedmann equation, which describes the evolution of the scale factor $a(t)$:

$$\dot{a}^2 + k = \frac{8}{3}\pi G \rho a^2, \tag{1.7}$$

where ρ is the energy density of the Universe. Substituting the definition of the Hubble parameter, we obtain

---

[1]1 pc $= 3.086 \times 10^{16}$ m

$$1 + \frac{k}{H(t)^2 a(t)^2} = \frac{\rho(t)}{\rho_c(t)}, \tag{1.8}$$

where ρ_c is the critical density, defined as

$$\rho_c = \frac{3H(t)^2}{8\pi G}. \tag{1.9}$$

If we assume a flat Universe ($k = 0$), we obtain that the energy density ρ must be equal to the critical energy

$$\rho = \rho_c = 1.054 \times 10^{-5} h^2 \text{ GeV cm}^{-2}, \tag{1.10}$$

and we introduce the dimensionless density parameters

$$\Omega_i(t) \equiv \frac{\rho_i(t)}{\rho_c(t)}, \tag{1.11}$$

where $i = m, r, \Lambda$ stands for matter, radiation and dark energy.

The density and flux of energy and momentum of the Universe is described by the energy-momentum tensor $T^{\mu\nu}$, which appears inside the Einstein's field equation. We consider the approximation of perfect fluid, therefore

$$T^{\mu\nu} = \text{diag}(\rho, -P, -P, -P), \tag{1.12}$$

where P is the pressure that characterises normal stress. Taking the time component of the continuity equation, $\Delta_\mu T^{\mu\nu} = 0$, where Δ_μ is the covariant derivative, we obtain the conservation of energy

$$\frac{\partial \rho}{\partial t} + 3\frac{\dot{a}}{a}(\rho + P) = 0. \tag{1.13}$$

The equation of state $p = w\rho$ could be applied to different forms of energy density, such as matter ($w = 0$) or radiation ($w = 1/3$). Applying the conservation of energy, we obtain the following equation

$$\dot{\rho}/\rho = -3(1 + w)H. \tag{1.14}$$

Solving this equation we obtain that $\rho_m \propto a^{-3}$ for matter, $\rho_r \propto a^{-4}$ for radiation and $\rho_\Lambda = \text{const.}$ for dark energy. Hence, by measuring the densities of today, one can solve

$$H(a) = H_0 \left[\frac{\Omega_{m0}}{a^3} + \frac{\Omega_{r0}}{a^4} + \Omega_{\Lambda 0} \right]^{1/2}, \tag{1.15}$$

to calculate how the scale factor has changed over time.

The early Universe was not only very dense, but also very hot; this high temperature initially produced quarks, which then hadronized into baryons at lower temperatures. A few minutes after the Big Bang, the Universe cooled enough to support simple nuclei forming in a process known as Big Bang Nucleosynthesis (BBN) [20]. These light elements were formed from the primordial plasma, first forming protons and neutrons, then deuterium, helium-3, helium-4, and lithium. The abundance of deuterium is the cleanest prediction to test BBN; in fact, it is not known to be produced by any astrophysical source, therefore the only way it can be produced in the Universe was during BBN. The observed abundance of deuterium $D/H \sim 10^{-5}$ can be explained by a baryon density of $\Omega_b h^2 \sim 0.02$ [21, 22]. Figure 1.3 shows the consistency between measurements of the baryon density Ω_b coming from the CMB [23] and the deuterium abundance [24].
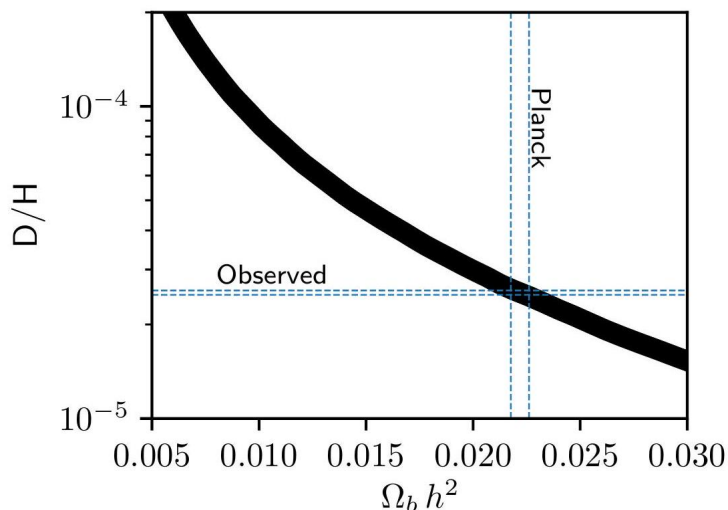
Figure 1.3: Concordance between Deuterium to Hydrogen abundance found in Ref. [24] and the Planck collaborations result reported in Ref. [23]. The black curve corresponds to BBN calculations of primordial abundances as a function of baryon density

The CMB is the afterglow that came from the recombination epoch, approximately $380,000$ years after the big bang [25, 26]. In this epoch, electrons and protons begin to bind electrically, forming hydrogen atoms. Before this period, photons were trapped between the baryonic matter due to Thompson scattering with charged ions, but after recombination, neutral hydrogen atoms were formed, therefore photons began to travel freely through the Universe, which indeed became transparent.

Because the CMB happened a long time ago, to this day the temperature distribution that we measure is incredibly homogeneous. The small temperature fluctuations in the CMB provide important information about the structure of the early Universe.

It is possible to analyse the CMB using the angular power spectrum, in which the

multipole order ℓ can be related to the angular size. Figure 1.4 shows the power spectrum, where $\mathcal{D}_l$ is the variance in temperature.
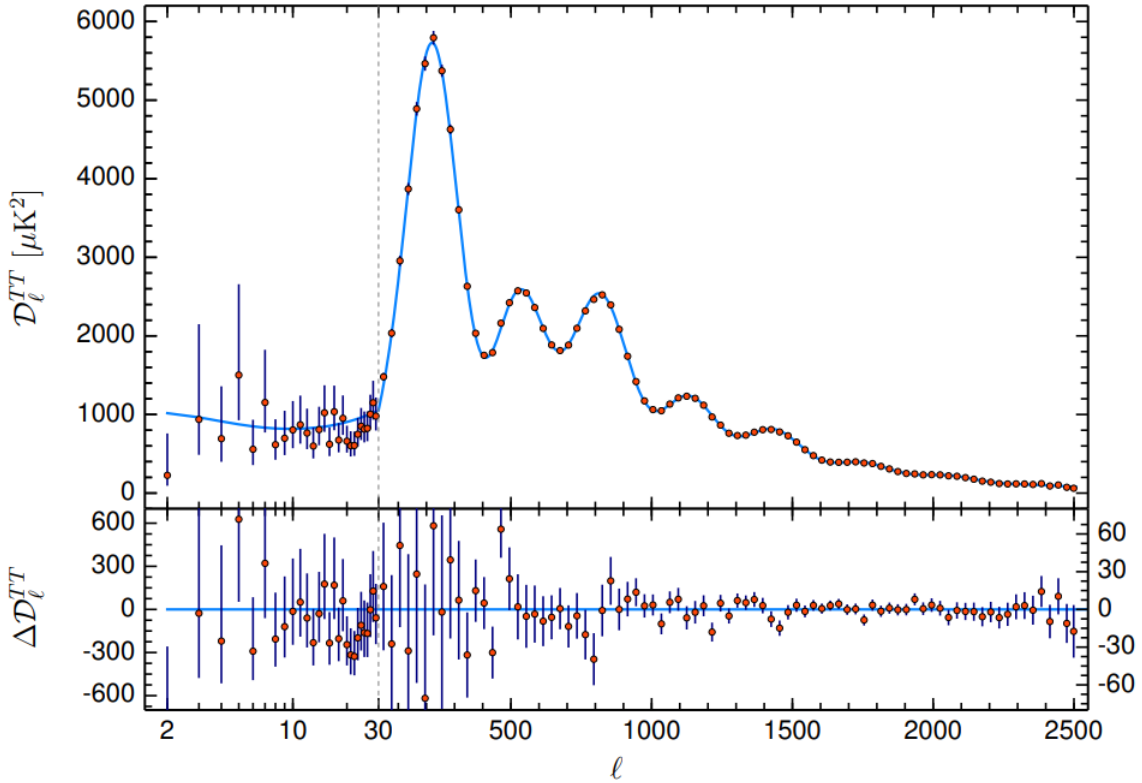
Figure 1.4: Angular power spectrum of the CMB temperature fluctuations taken from Ref. [27]. The curve represents the best assuming ΛCDM topological model. Residuals are shown in the bottom panel.

The first peak was measured by WMAP, where they reported a flat curvature [28, 29]. By measuring subsequent peaks, it is possible to extract the values of the density parameters Ω_i; in the case of Ω_{DM}, only the first peaks are sufficient. This is due to the fact that by using the relative heights of the peaks, one can disentangle multiple effects. While the relative baryon density produces an enhancement of odd peaks due to baryon loading in oscillations, the total matter density can be inferred by observing which perturbations entered the horizon before equality. This is a consequence of Gravitational Driving [30]. Thanks to the experimental measurement of Planck, we can finally get the most stringent measurements on the total DM density [27],

$$\Omega_{\mathrm{DM}}h^2 = 0.1199 \pm 0.0027. \tag{1.16}$$

By comparing the value of the DM density to the baryon one, we see that, even at very early times, baryons were a sub-dominant component of matter in the Universe.

Based on the experimental evidence, it is clear that DM plays a fundamental role in the evolution of the Universe. However, the nature of DM remains unknown. The prevailing hypothesis is that DM is a new fundamental particle that isn't described by the SM. In this scenario, based on the measurements of mass-to-light ratio of galaxies, we deduce that DM must be a massive particle, and because we have not observed light emission from DM, we deduce that it is a neutral particle, or at least couples weakly with photons. In the case in which DM particles interacts weakly with SM particles, they are also referred to as WIMPs (weakly interacting massive particles), and is the scenario that we will consider in this thesis. Thanks to the measurements of cluster collision, we also conclude that DM particles does not interact, or interact weakly with themselves. Using the experimental data, we can put bounds on the strength of DM self-interaction [31]:

$$\frac{\sigma_{\text{self}}}{m_{\text{DM}}} < 1 \text{ cm}^2 \text{ g}^{-1}, \tag{1.17}$$

where σ_{self} is the DM self-interaction cross-section and m_{DM} is the DM mass. In a first approximation, we can assume that DM is a collisionless particle. Another propriety that characterize DM is that it is non-relativistic. For this reason, we say the DM particle is "cold". This last propriety can be obtained by studying the effect of DM particles on structure formation in the Universe [32, 33].

1.2 Boltzmann's equation and freeze-out

If DM is a particle, it should have been formed during the early Universe, and it should have produced the relic abundance measured by Planck. We can use thermodynamic principles to describe the DM as a particle in the early Universe. If there is a non-gravitational coupling between DM and SM matter, we can describe the DM number density n_χ using Boltzmann equations:

$$\dot{n}_\chi + 3H n_\chi = \frac{g_\chi}{(2\pi)^3} \int C[f] \frac{d^3 p_\chi}{E_\chi}, \tag{1.18}$$

where g_χ is the internal degrees of freedom, p_χ is the DM three-momentum and E_χ is the DM energy. C is the collisional operator, which depends on the specific BSM model, and modifies the number density n_χ through its action. For instance, if a DM particle χ and SM particles f annihilate only via $2 \to 2$ processes, the Boltzmann equation becomes

$$\dot{n}_\chi + 3H n_\chi = n_f^2 \langle \sigma v \rangle_{f\bar{f} \to \chi\bar{\chi}} - n_\chi^2 \langle \sigma v \rangle_{\chi\bar{\chi} \to f\bar{f}}, \tag{1.19}$$

where $\langle \sigma v \rangle$ is the thermally averaged cross-section defined by

$$\langle \sigma v \rangle_{\chi\bar{\chi}\to f\bar{f}} \equiv \frac{1}{n_{\chi,\text{Eq}}n_{\bar{\chi},\text{Eq}}} \int \frac{d^3p_{\bar{\chi}}}{2E_{\bar{\chi}}} \frac{d^3p_{\chi}}{2E_{\chi}} \sigma_{\chi\chi\to ff} \exp\left[-\left(E_{\chi}+E_{\bar{\chi}}\right)/T\right], \qquad (1.20)$$

where T is temperature. Assuming that $\mathcal{CP}$ is not violated, $\langle \sigma v \rangle_{ff\to\chi\chi} = \langle \sigma v \rangle_{\chi\chi\to ff}$, that leads to the following simplification

$$\dot{n}_{\chi} + 3Hn_{\chi} = \langle \sigma v \rangle \left(n_f^2 - n_{\chi}^2\right). \qquad (1.21)$$

Because SM particles in the early Universe are in equilibrium, they follow the corresponding thermal number densities, that are different for relativistic (rel) and non-relativistic (nr) particles

$$\begin{aligned}
n_{\text{rel}} &= g\varepsilon_{\text{FB}}\frac{\zeta(3)}{\pi^2}T^3, \\
n_{\text{nr}} &= g\left(\frac{m_{\chi}T}{2\pi}\right)^{3/2} e^{(\mu-m)/T},
\end{aligned} \qquad (1.22)$$

where ε_{FB} is a numerical factor equal to $3/4$ for fermions and 1 for bosons. For a particle species to be in thermal equilibrium, it must satisfy the condition that its particle interaction rate, which, in the case of our $2 \to 2$ example, is the annihilation rate $n_{\chi}\langle \sigma v \rangle$, is greater than the expansion rate $H(t)$. As the Universe expands and cools, the annihilation rate can decrease below $H(T)$, at which point the particle will no longer interact quickly enough. This results the comoving number density $Y = n/T^3$ to become constant, or, in other words, the comoving number density "freezes-out". This fact can be seen by modifying Eq. (1.21), obtaining

$$\frac{dY}{dT} = \frac{\langle \sigma v \rangle s}{HT}\left(Y_{\chi}^2 - Y_{\text{eq},\chi}^2\right). \qquad (1.23)$$

In this calculation, we utilized the principle of entropy conservation, which states that sR^3 remains constant. We also made the assumption that the process occurred during the radiation dominant era, where $\dot{T} = -HT$.

When dealing with relativistic particles, the quantity $Y_{\text{eq},\chi}$ is not dependent on temperature. Therefore, the final value of Y at a later time is equal to the equilibrium value at the moment of freeze-out. The number density of a species that remains in equilibrium and one that becomes decoupled differ in the present day because the number of radiation degrees of freedom that contribute to the radiation energy density, g_*, and the radiation degrees of freedom that contribute to the radiation entropy density, g_{s*}, change over time. The number of degrees of freedom are approximately given by

$$g_* = \sum_{\text{bosons}} g_i \left(\frac{T_i}{T}\right)^4 + \frac{7}{8} \sum_{\text{fermions}} g_i \left(\frac{T_i}{T}\right)^4,$$

$$g_{*s} = \sum_{\text{bosons}} g_i \left(\frac{T_i}{T}\right)^3 + \frac{7}{8} \sum_{\text{fermions}} g_i \left(\frac{T_i}{T}\right)^3,$$

(1.24)

where T_i is the temperature of decoupled relativistic particle species i, that are no longer in thermal equilibrium. The behaviour of g_{*s}^2/g_* over temperature is shown in Fig. 1.5.
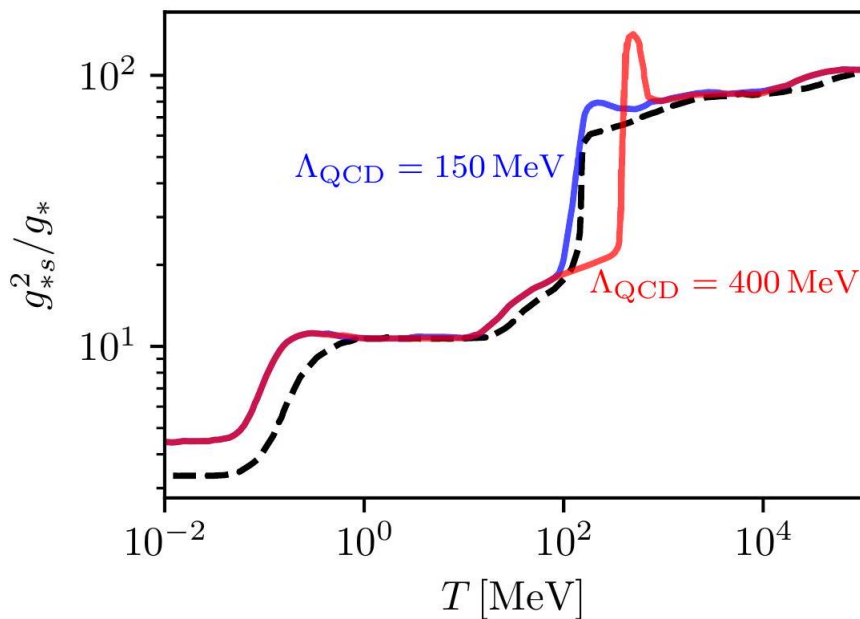
Figure 1.5: Ratio between the squared radiation energy density, g_*, and the radiation degrees of freedom that contribute to the radiation entropy density, g_{s*} [34]. The dashed line comes from simply counting both relativistic degrees of freedom in Eq. (1.24) as contributions to the energy and entropy density, respectively. Ref. [35] calculates these contributions more precisely and considers the QCD phase transition at different temperatures, which we show with solid lines. The level of agreement between the dashed line and the solid lines appears to be within an acceptable range.

As a concrete example, we could try to explain the DM density using only neutrinos, because they are the only SM particle that could mimic the DM behaviour, given that it is a neutral massive particle that interacts weakly with SM particles. Knowing that the neutrinos freeze out at $T \sim 1\text{MeV}$, it is possible to compute their density as

$$\Omega_\nu h^2 = \frac{\sum_i s_0 Y_{\text{eq}}(T_f) h^2 m_{\nu_i}}{\rho_c} = \frac{\sum_i m_{\nu_i}}{91\text{eV}},$$

(1.25)

15

where we have summed over different generations of active neutrinos. In the case in which the neutrinos exclusively contribute to the DM density, i.e. $\Omega_\nu h^2 = 0.11$ we would need the sum of the masses of the three generations to be ~ 9 eV, which is of orders of magnitude higher than experimental upper bounds of 0.12eV [36].

Another reason for which neutrinos can not contribute entirely to the DM density is that, by studying structure formations, we know that DM must be a cold particle, while neutrinos are relativistic. In the non-relativistic case, the equilibrium comoving number density is

$$Y_{\text{eq,nr}} = \frac{45g}{2\pi^4 g_*} \sqrt{\frac{\pi}{8}} \left(\frac{m}{T}\right)^{3/2} e^{-m_\chi/T}. \tag{1.26}$$

If we define the variable $x = m_\chi/T$, Eq.(1.23) becomes

$$\frac{dY}{dx} = -\lambda x^{-2} \left(Y_\chi^2 - Y_{\text{eq},\chi}^2\right), \tag{1.27}$$

where

$$\lambda \simeq 0.264 \left(g_{*s}/g_*^{1/2}\right) M_{\text{Pl}} m_\chi \langle\sigma v\rangle, \tag{1.28}$$

in which we plug the values of g_{*s}^2/g_* shown in Fig. 1.5. After freeze-out, $Y_{\text{eq}}(x)$ is exponentially suppressed, therefore Eq. (1.27) becomes

$$\frac{dY}{dx} = -\lambda x^{-2} \left(Y_\chi^2\right). \tag{1.29}$$

In the-non relativistic limit, we can expand $\langle\sigma v\rangle$ in powers of v via the plane-wave expansion,

$$\langle\sigma v\rangle \approx \langle\sigma v\rangle_{\text{s}} + \langle\sigma v\rangle_{\text{p}} v^2 + \dots, \tag{1.30}$$

where the subscripts names are given using plane-wave scattering nomenclature. Since $v^2 \sim T/m$, the highest order of $\lambda(x)$ is independent of velocity, i.e. x^0. We can solve Eq. (1.29), and the solution is shown in Fig. 1.6. We see that the comoving number density drops exponentially until the freeze out point, at which it becomes constant. For increasing values of λ the relic density becomes lower, due to a later freeze-out.

For a broad range of masses and cross sections, the temperature at which freeze-out occurs is roughly $T_f \sim 20m_\chi$. Although Y_∞ is quite sensitive to the mass m_χ, the CMB constraint is not particularly sensitive to it, since $\rho_\chi = s_0 Y_\infty/m_\chi$. This leads to an approximate value of $\langle\sigma v\rangle \simeq 1 \times 10^{-26}$ cm^3 s^{-1} for a DM mass across the GeV to TeV range. This value for σ is very similar to that of electroweak processes. This coincidence has been named the "WIMP miracle", which was initially quite promising for the numerous extensions of the SM that predicted new physics at the weak scale.
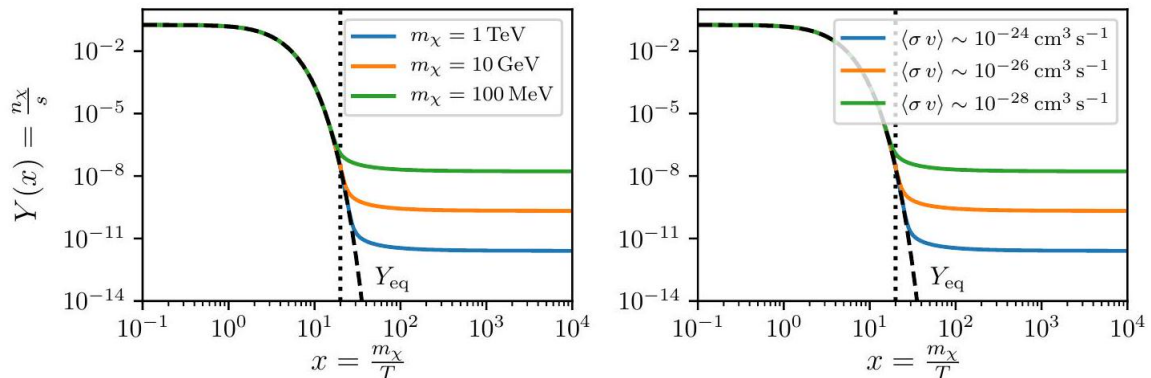
16

Figure 1.6: Numerical solutions to Eq.(1.29) for different values of m_χ on the left and $\langle \sigma v \rangle$ on the right. We see that a sub-GeV DM freezes-out at approximately $x = 20$, drawn with a dotted line [34].

If we approximate the annihilation cross-section of a weak-scale interaction as $\sigma \sim G_F^2 m_\chi^2$, we arrive at the Lee-Weinberg bound, which states that the DM mass m_χ must be above few GeV [37, 38]. Additionally, requiring that unitarity is respected gives an upper bound of $m_\chi \lesssim 100\,\text{TeV}$ [39]. However, both of these bounds can be avoided. For instance, they can be alleviated for composite DM candidates, in which the DM particle content is given by more than one species of DM, with a certain hierarchy of masses like in the SM [40], and the lower bound can be circumvented for specific scalar models [41]. Nonetheless, these two bounds typically define the mass range that is considered when discussing WIMPs. This range is where numerous experiments are most sensitive and therefore capable of investigating these thermally generated candidates.

1.2.1 Freeze-in mechanism

It is not necessary to assume that DM was in thermal equilibrium with the SM at some point to achieve the correct relic abundance. If the coupling to the SM is weak enough that equilibrium is never reached, DM will be produced effectively through a one-way process in the thermal bath. This results in a slow approach to a stable abundance, which is referred to as Freeze-in mechanism. FIMPs (Feebly Interacting Massive Particles) are DM candidates that couple extremely weakly to the SM and can produce the correct relic abundance for a broad range of masses, usually ranging from eV to TeV [42, 43]. Although FIMPs have never reached thermal equilibrium, they have been generated with some energy from the SM bath. If scattering is feasible among the FIMPs, they may thermalize and reach equilibrium [44]. Other types of FIMPs may be metastable and decay into a thermal DM candidate, such as the scenario of SuperWIMPs [45]. SuperWIMPs increase their abundance through metastable decay, implying that their

connection to the SM can be limited.

1.3   The DM search

There are numerous ways in which DM could exist in our Universe. The above-mentioned production mechanisms demonstrate that we have not restricted the possibilities significantly, which motivates further experimentation. Many or most of the experimental searches focus on WIMPs, that is the case considered in this thesis.

In this section, we will briefly describe the main three approaches for detecting DM: indirect detection, production at collider, and direct detection.
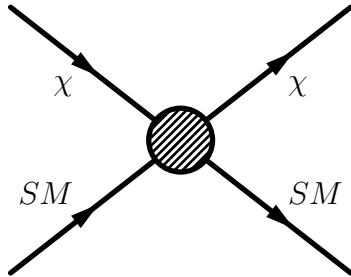
Figure 1.7: Diagram representing schematically the interaction between a DM particle χ and a SM particle. Reading it from top to bottom, the DM particles annihilate into two SM particles. From bottom to top, DM particles are produced from SM ones. From left to right, a SM particle scatters with a DM one.

1.3.1   Indirect detection

This method of detection is used for models where DM can decay or annihilate into SM particles. This process can be seen by reading Fig. 1.7 from top to bottom. Many thermal freeze-out models would generate detectable signals, but only for those with S-wave thermal cross sections, given that the other cross sections are suppressed by powers of the DM velocity v, as shown in Eq. (1.30). If the products of annihilation or decay are photons or neutrinos, they would travel to Earth mostly undisturbed. Satellites or ground-based telescopes look for regions of high DM density such as the Milky Way centre to test DM models. The Fermi Large Area Telescope (Fermi LAT) [46] can constrain the annihilation into photons for a vast DM mass range. Dwarf spheroidal galaxies are ideal DM structures to look for signals [47] because they have fewer sources of gamma-ray background, but their DM structure uncertainties are higher. For masses above 1 TeV, HESS [48] and HAWC [49] experiments are more sensitive. Neutrino detectors such as IceCube [50] and Antares [51] can detect high-energy neutrinos and identify the direction

of the source, allowing them to restrict certain sources like the Galactic centre or the Sun, which may contain a higher DM density within it [52].

The detection of antiprotons and positrons in the interstellar medium provides valuable information for constraining DM models. In models where DM can annihilate or decay into SM particles, equal amounts of DM and anti-DM, as seen in the case of WIMPs, could result in an excess of SM antiparticles beyond astrophysical predictions. The AMS-02 [53] and PAMELA [54] experiments have successfully constrained DM models within the mass range of $100\text{MeV} - 1\text{TeV}$.

1.3.2 Collider searches

Collider searches focus on the processes wherein DM is generated via collisions of SM particles. This process is described in Fig. 1.7 by reading it from bottom to top. If the mediator particles that connect DM to SM are heavy, as is the case in many scenarios, high-energy collisions are necessary for an efficient production of DM. Currently, the LHC is actively searching for such signals [55, 56].

In terms of detection, DM particles are similar to neutrinos, as they lack any electromagnetic or colour charge. If DM is the lightest and most stable particle of new states, then the collider signature would be a cascade decay of the heavier new states, ultimately yielding multi-parton or multi-lepton final states alongside missing energy.

Colliders have several advantages for DM searches. Firstly, they are equipped with multipurpose detectors capable of measuring numerous observables and reconstructing the kinematics of the DM production process. Secondly, colliders possess high luminosities, which is a crucial parameter in collider experiments that expresses the rate of events per second. High luminosity implies a vast amount of data, which may contain many DM-related events. Finally, simulations can be used to thoroughly examine background processes.

The combination of these three features renders colliders a promising method for DM searches. If we discover a new particle with DM properties through colliders, we will acquire a plethora of information about that particle. Nevertheless, detecting the signature of DM is a challenging task, and revealing a particle that does not decay within the detector volume does not necessarily imply that it is stable on a cosmological timescale. This is the primary prerequisite for DM in order to explain the DM relic density.

Collider searches have not yet detected any non-SM signals, leading to only constraints on DM models.

1.3.3 Direct detection

The direct detection method aims to observe scattering interactions between DM from the galactic halo of the Milky Way and ordinary matter by measuring the energy deposited from the scattering, as shown in Fig. 1.7 by reading it from left to right. Typ-

ically, elastic scattering is assumed. Direct detection experiments are placed in underground facilities [57, 58] in order to avoid cosmic ray background. There has been a worldwide experimental effort to achieve extremely sensitive experiments, which have probed DM interactions with ordinary matter with unprecedented precision. Even if we made huge progresses, the sensitivity of DM detectors will be hindered by unavoidable backgrounds from astronomical neutrinos [59–61]. Initially labelled as the "neutrino floor", this phenomenon is now commonly referred to as the "neutrino fog" to better represent that, rather than being an inflexible limit on the sensitivity of direct detection, the neutrino background imposes a gradual penalty that we can overcome only by increasing the exposure of the experiments.

So far, no signals of DM have been detected, therefore stringent upper bounds on the DM elastic scattering cross section with nuclei have been reported. For DM-nucleus interactions, we distinguish between spin-independent and spin-dependent cross sections: in the first case, the DM scattering with the nucleus isn't dependent on the spin of the two particles, and the DM scatters coherently with the whole nucleus, therefore the cross section is proportional to the mass number A of the nucleus. In the second case, the interaction depends on the spin of the two particles, so DM scatters only with the unpaired nucleons in the nuclear shell, given that nucleon pairs have spin 0, therefore SD cross section is generally suppressed with respect to the SI one.

Figure 1.8 provides a summary of the current status of spin-independent DM cross section limits and the projected sensitivity of future experiments. The blue contour map of Fig 1.8 presents the neutrino fog for a xenon target, indicating that neutrino backgrounds are a significant challenge for direct detection experiments. At contour n, obtaining a $10\times$ lower cross section sensitivity requires an increase in exposure of at least 10^n. The black wide-dashed line shows the $n = 2$ fog contour for argon.

Currently, the spin-dependent case is mainly dominated by xenon for interactions between DM and neutrons, as well as fluorine for interactions between DM and protons, for technologies that are in use or planned for the near future. Fluorine is also much less sensitive to coherent neutrino interactions than xenon, which enables it to reach much lower spin-dependent cross sections [73].

Dual-phase time projection chambers (TPCs) are currently being used in direct detection experiments to search for DM with masses above 6 GeV. Some examples of these detectors include LUX [69], XENON1T [74], and PandaX [62]. These detectors rely on two types of signals: a prompt photon signal from scintillation in the liquid xenon and a proportional charge signal amplified in the gas phase. By comparing the ratio of these signals, it is possible to recognize the recoiling particle. The position of the interaction in the TPC can be determined from the drift times and light pattern of the signals, allowing for a background-free fiducial volume to be defined due to self-shielding.

The next generation of liquid noble gas detectors, using xenon (LZ [75], XENONnT [76], and DARWIN [77]) or argon (DarkSide20k [78]), will further probe the parameter space of WIMPs with unprecedented precision. These detectors, using either xenon or argon,
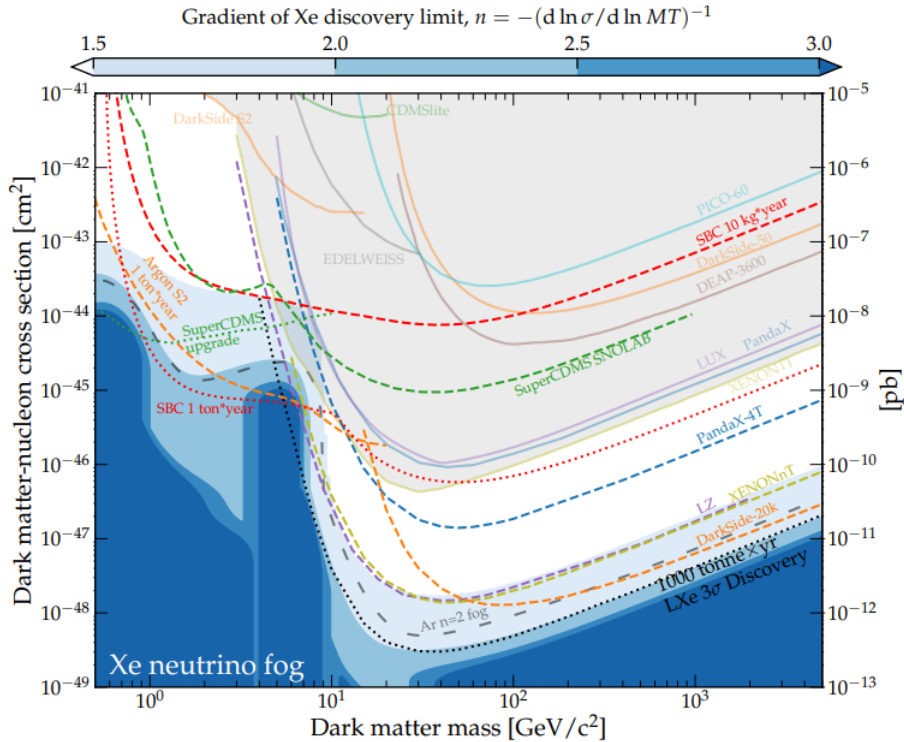
Figure 1.8: Exclusion limits for spin-independent dark-matter nucleon scattering cross section vs DM mass. The gray area shows the currently excluded space [62–71] (data points taken from [72]). The dashed lines indicate the projected 90% confidence level exclusion sensitivity of upcoming experiments. The blue contour map of Fig 1.8 presents the neutrino fog for a xenon target. Figure from Ref. [73].

are expected to have improved sensitivity and lower background levels, allowing for the detection of even weaker DM interactions.

Direct detection experiments typically have an energy threshold of a few keV, making it difficult to constrain lower mass DM, except for the DarkSide-50 result [68]. Crystal detectors such as SuperCDMS [79] and CRESST [66] have made significant progress in lowering the energy threshold of direct detection experiments, detecting energy deposition via phonons. CDMS is capable of detecting ionization, while CRESST detects scintillation signals [80]. Additionally, the NEWS-G experiment [81] uses new spherical proportional counters and light noble gases to search for light DM. These experiments have relatively light nuclei and low thresholds, making them prominent in constraining DM masses below 6 GeV. However, these collaborations have less exposure compared to their heavier counterparts and do not reach the same level of sensitivity.

In recent times, there have been significant advancements in both theoretical and experimental aspects of DM detection, with an emphasis on exploring alternative technologies

for direct detection, especially for low-mass DM models. While, as we said, by analysing DM-nucleon recoil it is possible to be sensitive to DM masses of the order of the GeV, by using the same data it is also possible to constrain DM with masses on the order of the MeV. This can be done by considering models in which DM couples to electrons. Given that the electrons are orders of magnitude lighter than the nuclei used in direct detection experiments, a lighter DM could scatter an electron off the target atom with sufficient energy to produce a detectable signal. The current experimental status of direct detection trough electronic recoil is shown in Fig. 1.9.
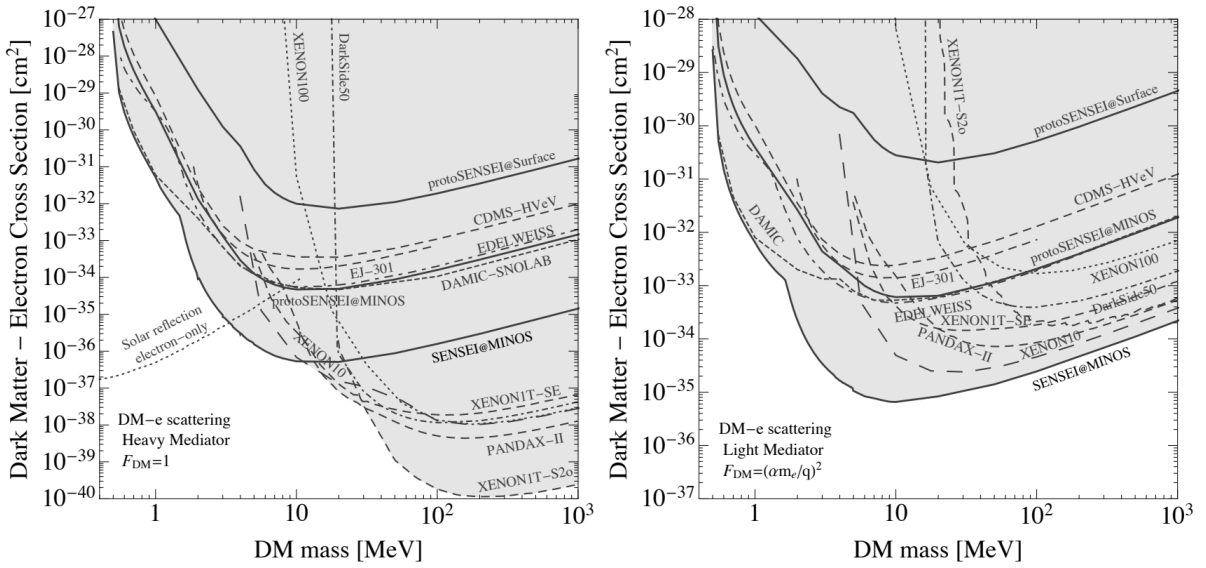
Figure 1.9: Left: Current 90% C.L. limits on DM-electron scattering mediated by a heavy mediator from SENSEI [82–84], CDMS-HVeV [85, 86], DAMIC at SNOLAB [87], EDELWEISS [88], DarkSide-50 [89], XENON10 [90–92], XENON100 [93], XENON1T (S2-only ("S2o") and single-electron ("SE") analyses) [94, 95], PandaX-II [96], and EJ-301 [97]. Right: Same as for top left plot, but assuming scattering mediated by an ultralight mediator. Figure from Ref. [98]

In this thesis, I will focus on direct detection analysis of DM, focusing on the XENON10 and XENON1T experiments.

Chapter 2

Direct Detection of DM

In this chapter, we will describe the aspects of DM scattering useful to compute the theoretical rates in direct detection experiments, focusing on the DM scattering with bound electrons.

We start with the description of the DM velocity distribution in the Solar System, followed by describing the kinematics of the DM-e scattering. We describe then the non-relativistic effective theory for DM-electron interaction, useful to compute the interaction matrix element. Once we have computed the matrix element of the scattering, in order to compute the ionization rate, we need to take into account the fact that the electron is bound to an atom. This is encoded in the atomic response functions presented in the following section. The computation of the atomic response functions is reported following Ref. [99], and the numerical evaluation of those functions, showed in Fig. 2.3 and 2.6, was done using the software in Ref. [100].

2.1   DM velocity distribution

For direct detection experiments, it is important to know the DM density and how it is distributed close to the Sun. We refer to it as the "local" DM density and the "local" DM distribution.

The local DM density is typically assumed to be $\rho_\chi = 0.4\mathrm{GeV/cm^3}$, which is obtained from models of the local gravitational potential within a distance of 1 kpc. However, various techniques yield different results, with differences ranging from $10 - 50\%$ of ρ. A comprehensive review of the measurements and methods can be found in Ref. [101].

Determining the velocity distribution of DM is a challenging task, as even small variations in the distribution can have significant effects on the rates of direct detection. A commonly used approximation for the velocity distribution of DM in the solar neighbourhood is a truncated Maxwellian distribution, as it is expected that DM is mostly virialized in this region. In the frame of the Galaxy, this distribution is isotropic and is

represented by the following formula:

$$f_{\text{Galaxy}}(\mathbf{v}) = \frac{1}{N(v_0)} \exp\left(-\frac{\mathbf{v}^2}{v_0^2}\right) \Theta(v_{\text{esc}} - |\mathbf{v}|), \tag{2.1}$$

where v_0 is approximately equal to 220 km/s ($\sim 10^3$ c) [102]. The distribution is truncated at the local escape speed, which is estimated to be $v_{\text{esc}} \simeq 544$ km/s [103]. The normalization factor $N(v_0)$ ensures that $f(\mathbf{v})$ is normalized

$$N(v_0) = \pi^{3/2} v_0^3 \left[\text{erf}\left(\frac{v_{\text{esc}}}{v_0}\right) - \frac{2}{\sqrt{\pi}} \frac{v_{\text{esc}}}{v_0} \exp\left(-\frac{v_{\text{esc}}^2}{v_0^2}\right)\right]. \tag{2.2}$$

This is known as the Standard Halo Model. We need then to boost Eq. (2.1) in the Earth (laboratory) frame:

$$f_{\text{Earth}}(\mathbf{v}) = \frac{1}{N(v_0)} \exp\left(-\frac{(\mathbf{v} + \mathbf{V}_e(t))^2}{v_0^2}\right) \Theta(v_{esc} - |\mathbf{v} + \mathbf{V}_e(t)|), \tag{2.3}$$

where $\mathbf{V}_e$ is the Earth's velocity, that we can decompose into the Sun's motion in the Galaxy ($\mathbf{V}_\odot$) and the orbit of the Earth about the Sun ($\mathbf{V}_\oplus$) :

$$\mathbf{V}_e(t) = \mathbf{V}_\odot + \mathbf{V}_\oplus(t). \tag{2.4}$$

When computing rates, the Earth's orbital motion can be neglected due to the fact that its velocity $|\mathbf{V}_\oplus| \approx 29.8$ km/s is significantly less than the Sun's rotational velocity $|\mathbf{V}_\odot| \approx 232$ km/s [104]. The Sun's motion has a fixed direction relative to the Milky Way, which is towards the Cygnus constellation, therefore the DM velocity distribution seems to be approaching us on average from the opposite direction $-\mathbf{V}_\odot$. This leads us to refer to the incoming DM as a "wind" from Cygnus, although in reality there is a distribution of DM arrival directions.

We now define the following function, which we will use later to compute the DM interaction rate

$$\begin{aligned}
\eta(v_{\text{min}}) &= \int d^3 v g_\chi(\vec{v}) \frac{1}{v} \Theta(v - v_{\text{min}}) \\
&= \frac{1}{K} \int 2\pi d\cos\theta dv v e^{-\left(v^2 + V_e^2 - 2vV_e c_\theta\right)/v_0^2} \Theta(v - v_{\text{min}}) \Theta(v_{esc} - |\mathbf{v} + \mathbf{V}_e(t)|),
\end{aligned} \tag{2.5}$$

where v is the DM velocity, $V_E = |\mathbf{V}_E|$ is the velocity of the Earth, $c_\theta = \cos\theta$ is the angle between the velocity and the velocity of the Earth and v_{min} is the minimum velocity defined in Eq. (2.24). We can explicitly solve Eq. (2.5) considering the two following cases:

1. $v_{\text{min}} < v_{\text{esc}} - V_E$,

2. $v_{\text{esc}} - V_E < v_{\min} < v_{\text{esc}} + V_E$,

where $v_{\text{esc}}, V_E, v_{\min} > 0$. In these two cases, we obtain the following solutions [105]:

$$\eta_1\left(v_{\min}\right) = \frac{v_0^2\pi}{2V_E K}\left(-4e^{-v_{\text{esc}}^2/v_0^2}V_E + \sqrt{\pi}v_0\left[\text{Erf}\left(\frac{v_{\min}+V_E}{v_0}\right) - \text{Erf}\left(\frac{v_{\min}-V_E}{v_0}\right)\right]\right),$$

$$\eta_2\left(v_{\min}\right) = \frac{v_0^2\pi}{2V_E K}\left(-2e^{-v_{\text{esc}}^2/v_0^2}\left(v_{\text{esc}} - v_{\min} + V_E\right) + \sqrt{\pi}v_0\left[\text{Erf}\left(\frac{v_{\text{esc}}}{v_0}\right) - \text{Erf}\left(\frac{v_{\min}-V_E}{v_0}\right)\right]\right),$$

(2.6)

where the subscript corresponds to the case number. Note that the two cases converge to the same value for $v_{\min} = v_{\text{esc}} - V_E$.

It is important to know that the assumption of a Maxwellian velocity distribution may not hold for the entire range of DM velocities. Simulations suggest that the true distribution is more complex, possibly anisotropic within the Galaxy, and may have un-virialized components [106–108]. Additionally, the sharp cut-off at the escape velocity is not physically realistic. As a result, using the Maxwellian distribution to calculate elastic scattering rates for DM may affect the recoil spectrum and have a certain impact on total rates. This impact is larger for light DM because direct detection experiments are more sensitive to DM with high velocity, therefore it is important to have a detailed knowledge of the velocity distribution tail. Although we lack direct means of measuring the velocity distribution, recent studies have examined the velocity distribution of the metal-deficient stellar halo as a substitute for DM [109–111]. As more data becomes available, we anticipate that our understanding of this distribution will become more accurate.

2.2 Kinematics of DM scattering in direct detectors
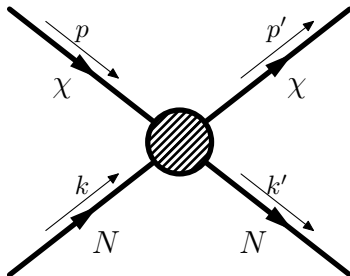
2.2.1 DM - nucleus scattering

Figure 2.1: Diagram representing schematically the scattering between a DM particle χ and a nucleus N.

An examination of the kinematics of DM-nucleus scattering can help identify the relevant physics. In direct detection experiments, the typical kinetic energy of a nucleus is proportional to the temperature T of the target, which is usually well below room temperature, allowing us to consider the nucleus to be initially at rest. Referring to the momentum labels in Fig. 2.1, the initial total momentum and energy of DM can be expressed as:

$$E_i = \frac{\mathbf{p}^2}{2m_\chi}, \quad \mathbf{p} = m_\chi \mathbf{v}, \tag{2.7}$$

where $\mathbf{v}$ is the DM velocity. In the collision, the DM particle exchanges a momentum $\mathbf{q} = \mathbf{p}' - \mathbf{p}$. The energy of the outgoing DM particle is

$$E_f = \frac{(\mathbf{p} - \mathbf{q})^2}{2m_\chi} + \frac{\mathbf{q}^2}{2m_N}, \tag{2.8}$$

while the recoil energy of the nucleus is

$$E_R = \mathbf{q}^2 / (2m_N). \tag{2.9}$$

Defining $\cos\theta = \hat{\mathbf{p}} \cdot \hat{\mathbf{q}}$, energy conservation gives the requirement that

$$\frac{|\mathbf{p}||\mathbf{q}|\cos\theta}{m_\chi} = \frac{\mathbf{q}^2}{2\mu_{\chi N}}, \tag{2.10}$$

where $\mu_{\chi N} = m_\chi m_N / (m_\chi + m_N)$ is the reduced mass for the DM-nucleus system. The maximum momentum transfer is limited to

$$|\mathbf{q}|_{\max} = \frac{2\mu_{\chi N}|\mathbf{p}|}{m_\chi} = 2\mu_{\chi N} v, \tag{2.11}$$

where $v = |\mathbf{v}| \sim 10^{-3}$ is the average DM speed in the laboratory frame. For a WIMP with a mass of the order of tens of GeV, and a typical nucleus used in direct detection, the value of $\mu_{\chi N}$ is approximately 10-100 GeV, and $|\mathbf{q}|_{\max}$ is approximately 20-200 MeV. This leads to a maximum recoil energy of:

$$E_R^{\max} = \frac{|\mathbf{q}|_{\max}^2}{2m_N} = \frac{2\mu_{\chi N}^2 v^2}{m_N} \simeq 20 - 200 \text{ keV}. \tag{2.12}$$

The energy threshold for direct detection experiments is of the order of the keV (1.6 for Xenon1T [70] and 1.1 keV for LUX [112]), therefore we see that we are sensitive to DM above the GeV. In this calculation, we have only considered the typical DM speed, however, it is possible for larger recoils to occur if the DM has greater speeds. In such cases, the minimum incoming speed for DM to produce a given recoil energy would be

$$v_{\min} = \sqrt{m_N E_R / 2\mu_{\chi N}^2}. \tag{2.13}$$

Nevertheless, the probability of DM with higher velocities decreases exponentially, and there is almost no DM with velocities greater than the local escape velocity, which corresponds to $v_{\text{esc}} \sim 3 \times 10^{-3}$ in the lab frame.

The energy and momentum scales are important in understanding the physics of DM-nucleus interactions. To determine the length scale of typical momentum transfer, we use $1/|\mathbf{q}| \sim 1 - 10$ fm, which is similar to the radius of the nuclei used in direct detection experiments. For this reason, we need to account for a form factor in DM-nucleus interactions. When $1/|\mathbf{q}| \gg 10$ fm, the DM interacts coherently with the entire nucleus, leading to a rate scaling as A^2 in the small $|\mathbf{q}|$ limit, where A is the atomic number. However, form factor suppression occurs at larger $|\mathbf{q}|$ depending on the target nucleus. It is assumed that the effect of exciting bound atomic or nuclear states can be neglected. Nuclear excited states have a splitting of $\sim 30 - 1000$ keV, leading to smaller rates for inelastic scattering compared to elastic recoils [113–116].

It is important to note that we have only considered the primary DM-nucleus interaction here, and the recoiling atom subsequently collides with other atoms in the target, leading to the detected signals in scintillation light, charge yield, or phonons.

DM-nucleus scattering can be approached through multiple steps. First, microscopic interactions are considered, and a suitable theory at the QCD scale is identified. The DM interaction operators with quarks and gluons are then matched with operators that act on the whole nucleon. The nucleons inside a nucleus can be treated non-relativistically because their momentum scale is much smaller than their mass and is set by the nuclear radius R_N, where $1/R_N \simeq 1 - 10$ MeV $\ll m_{n,p}$, and the scattering with a DM particle is at low energy ($q \ll m_\chi, m_N$). Because the scattering is at low energy, the mediator is integrated out. Nuclear matrix elements for non-relativistic nucleon operators are determined using nuclear form factors or response functions. Finally, the differential scattering cross section is integrated against the DM velocity distribution in the lab frame to determine the rate of nuclear recoils.

2.2.2 DM - electron scattering
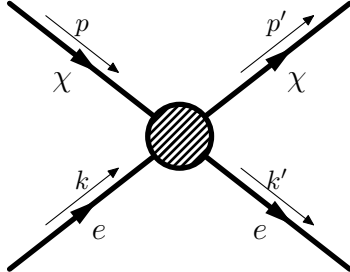
Figure 2.2: Diagram representing schematically the scattering between a DM particle χ and a electron e. The electron in this case is bound to the atom and has a non-zero momentum k.

While for DM-nucleus scattering we need a DM mass above the GeV to get a nucleus with enough recoil energy to be detected, DM-electron scattering offers a promising approach for identifying sub-GeV DM particles. In such a scenario, DM-electron scattering is inherently inelastic, which means that a greater fraction of the DM particle energy is transferred to the electron in the collision, resulting in ionization signals that can potentially be detected.

Let's consider a DM particle that collides with a bound electron, causing the electron to be excited to a higher-energy bound state or an ionized state. Unlike a nucleus, an electron in a bound state does not possess a specific momentum and could potentially have a limitless amount of momentum. Consequently, the kinematics in this scenario are vastly distinct from those in the previous section. Nonetheless, we can still determine the energy that the DM particle transferred to the electron in terms of the momentum that the DM particle lost $\mathbf{q} = \mathbf{p} - \mathbf{p}'$, where the labels for the momenta are shown in Fig. 2.2. The electron in this case is bound to the atom. The energy acquired by the electron is given by

$$\Delta E_e = -\Delta E_\chi - \Delta E_N, \tag{2.14}$$

where ΔE_χ and ΔE_N are respectively the difference in energy of the DM particle and the entire atom, which recoils after the scattering. The energy transfer for the DM particle is given by:

$$\Delta E_\chi = \frac{|m_\chi \mathbf{v} - \mathbf{q}|^2}{2m_\chi} - \frac{1}{2} m_\chi v^2. \tag{2.15}$$

We want now to study the recoil energy of the nucleus. In the case in which all the exchanged momentum is transferred to the nucleus, its recoil energy will be

$$\Delta E_N = \frac{q^2}{2m_N}. \tag{2.16}$$

In this case, we can write the difference in energy of the electron as

$$\begin{aligned}
\Delta E_e &= -\frac{|m_\chi \mathbf{v} - \mathbf{q}|^2}{2m_\chi} + \frac{1}{2}m_\chi v^2 - \frac{q^2}{2m_N} \\
&= \mathbf{q} \cdot \mathbf{v} - \frac{q^2}{2m_\chi} - \frac{q^2}{2m_N}.
\end{aligned} \tag{2.17}$$

In the case of light DM, we can neglect the term $\frac{q^2}{2m_N}$, which is smaller than $\frac{q^2}{2m_\chi}$. Therefore, we obtain

$$\Delta E_e = \mathbf{q} \cdot \mathbf{v} - \frac{q^2}{2m_\chi}. \tag{2.18}$$

We can find the maximum allowed energy transfer by maximizing this last equation with respect to $\mathbf{q}$. This would be the case in which all the kinetic energy of the collision is transferred to the electron.

$$\Delta E_e \leq \Delta E_e^{\text{max}} = \frac{1}{2}m_\chi v^2, \tag{2.19}$$

from which we can obtain a bound for the DM mass:

$$m_\chi \geq \frac{2\Delta E_e}{v^2}. \tag{2.20}$$

The energy transfer to the electron ΔE_e contributes to both the binding energy E_b^i of the electron in its initial bound state i, and to the electron recoil energy E_{er}

$$\Delta E_e = E_{er} + E_b^i. \tag{2.21}$$

Therefore, the bound for the mass becomes

$$m_\chi \geq \frac{2(E_{er} + E_b^i)}{v^2}. \tag{2.22}$$

The binding energy for the external shells of the atoms used in direct detection is of the order of tens of eV, and the typical electron recoil energy is on the order of tens of eV (see section 3.3.3). As said in the previous section, the typical DM velocity is on the order of 10^{-3}. By using these values inside Eq. (2.22), we obtain a minimum DM mass of the order of the MeV for Xe detectors.

We can substitute ΔE_e also in Eq. (2.18), and by taking the momentum transfer to be parallel to the initial DM velocity (so $\mathbf{q} \cdot \mathbf{v} = |\mathbf{q}||\mathbf{v}| \equiv qv$), we can find an expression for the minimum DM velocity required to obtain an electron recoil E_{er}.

$$E_{er} + E_b^i = q v_{\min} - \frac{q^2}{2m_\chi}. \tag{2.23}$$

Solving for $v_{\min}$ gives:

$$v_{\min} = \frac{E_{er} + E_b^i}{q} + \frac{q}{2m_\chi}. \tag{2.24}$$

Note from this equation that the minimum DM velocity required to excite an electron with recoil energy E_{er} depends on the bound-state energy of the target electron. This means that if we measure an electron with recoil energy E_{er}, this can be given by an interaction with a DM particle with velocity equal to $v_{\min}$ or bigger. Therefore, to compute the rate of DM interaction, we have to make an integral over the DM velocity distribution starting from $v_{\min}$.

2.3 Non-relativistic effective theory for DM - electron interaction

In direct detection of DM-e scattering, the scale of interaction is very small, because the DM particle that we consider is light ($m_\chi \gtrsim 1$ MeV/c^2) and non-relativistic, having a typical speed of the order of 10^{-3}, as mentioned in section 2.2.1. The electron is also non-relativistic, in fact the typical speed of electron bound in atoms is approximately αZ_{eff}, where $\alpha \simeq 1/137$ and $Z_{\text{eff}} \simeq 1$ for electrons in outer shells, which have a higher probability to be ionized from a DM scattering. Because the faster and lightest particle is the electron, we expect that the typical momentum transfer is approximately $Z_{\text{eff}}\alpha m_e$ [105]. Therefore, it can be useful to describe the DM - e scattering using a non-relativistic effective field theory (NREFT).

NREFT is different from relativistic EFT; in the latter, the operators are built by combining the known field content in a gauge and Lorentz invariant way. These relativistic operators $\mathcal{O}_i$ are then parametrized by their Wilson coefficients $c_{(j)}^i$, where j is the dimension of the associated operator, and then inserted in the SM Lagrangian:

$$\mathcal{L} = \mathcal{L}_{\text{SM}} + \sum_i \frac{c_{(5)}^i}{\Lambda} \mathcal{O}_i^{(5)} + \sum_i \frac{c_{(6)}^i}{\Lambda^2} \mathcal{O}_i^{(6)} + \dots, \tag{2.25}$$

where Λ is the scale of new physics. In the non-relativistic EFT the operators are defined using the relevant degrees of freedom that describe the particles, and are invariant under Galilean transformations and three-dimensional rotations, which, in a non-relativistic regime, replace Lorentz invariance.

In non-relativistic DM-electron scattering, the incoming (outgoing) electron and DM particle are characterized by their three-dimensional momenta k (k') and p (p'), respectively. However, due to momentum conservation and Galilean invariance, only two out of the four three-dimensional vectors are independent. Thus, a convenient choice for the independent momenta is given by the momentum transferred in the scattering $\mathbf{q}$, and the following velocity

$$
\begin{aligned}
\mathbf{v}^{\perp} &= \frac{(\mathbf{p} + \mathbf{p}')}{2m_\chi} - \frac{(\mathbf{k} + \mathbf{k}')}{2m_e} \\
&= \mathbf{v} - \frac{\mathbf{q}}{2\mu_e} - \frac{\mathbf{k}}{m_e},
\end{aligned}
\tag{2.26}
$$

where μ_e is the reduced mass of the DM particle and the electron, and $\mathbf{v}$ is the incoming DM velocity. In the case of elastic DM-electron scattering, $\mathbf{v}^{\perp} \cdot \mathbf{q} = 0$ because of energy conservation.

In addition to $\mathbf{q}$ and $\mathbf{v}^{\perp}$, the operators can also be built using the spin of the electron $\mathbf{S}_e$ and the spin of the DM particle $\mathbf{S}_\chi$ if it is not zero.

The resulting NREFT is then described in terms of a Lagrangian containing four-fermion non-relativistic operators $\mathcal{O}_i^{\mathrm{NR}}$, which account for the elastic scattering between a DM particle and a target electron,

$$
\mathcal{L}_{\mathrm{int}} = \sum_i c_i \mathcal{O}_i^{\mathrm{NR}} \chi^+ \chi^- N^+ N^-.
\tag{2.27}
$$

The non-relativistic fields $e^{\pm}$ and $\chi^{\pm}$ in this expression are simply constructed from quantum mechanical annihilation and creation operators, while the non-relativistic coefficients c_i are real parameters, that we need to match with the high energy coefficients. Using the degrees of freedom $\mathbf{q}$, $\mathbf{v}^{\perp}$, $\mathbf{S}_\chi$ and $\mathbf{S}_e$, the only NR operators $\mathcal{O}_i^{\mathrm{NR}}$ that we can build that are invariant under Galilean transformations and three-dimensional rotations are the following ones:

$$
\begin{aligned}
&\mathcal{O}_1^{\mathrm{NR}} = \mathbb{1}, \\
&\mathcal{O}_3^{\mathrm{NR}} = i\mathbf{S}_e \cdot \left(\mathbf{q} \times \mathbf{v}^{\perp}\right), \quad \mathcal{O}_4^{\mathrm{NR}} = \mathbf{S}_\chi \cdot \mathbf{S}_e, \\
&\mathcal{O}_5^{\mathrm{NR}} = i\mathbf{S}_\chi \cdot \left(\mathbf{q} \times \mathbf{v}^{\perp}\right), \quad \mathcal{O}_6^{\mathrm{NR}} = (\mathbf{S}_\chi \cdot \mathbf{q})(\mathbf{S}_e \cdot \mathbf{q}), \\
&\mathcal{O}_7^{\mathrm{NR}} = \mathbf{S}_e \cdot \mathbf{v}^{\perp}, \qquad\qquad \mathcal{O}_8^{\mathrm{NR}} = \mathbf{S}_\chi \cdot \mathbf{v}^{\perp}, \\
&\mathcal{O}_9^{\mathrm{NR}} = i\mathbf{S}_\chi \cdot (\mathbf{S}_e \times \mathbf{q}), \quad \mathcal{O}_{10}^{\mathrm{NR}} = i\mathbf{S}_e \cdot \mathbf{q}, \\
&\mathcal{O}_{11}^{\mathrm{NR}} = i\mathbf{S}_\chi \cdot \mathbf{q}, \qquad\qquad \mathcal{O}_{12}^{\mathrm{NR}} = \mathbf{v}^{\perp} \cdot (\mathbf{S}_\chi \times \mathbf{S}_e).
\end{aligned}
\tag{2.28}
$$

Since the non-relativistic fields are constructed with creation and annihilation operators, and since we are considering a 4-point interaction without propagators, the matrix element is given by

$$
\mathcal{M} = \sum_i c_i \mathcal{O}_i^{\mathrm{NR}}.
\tag{2.29}
$$

2.4 Matching the relativistic and non-relativistic theories

BSM models of DM are described by high energy physics, that we can approximate with relativistic EFT operators $\mathcal{O}_i$ at low energy. We therefore need to match these operators to the non-relativistic ones $\mathcal{O}_i^{NR}$ by taking the non-relativistic expansion of the first ones. In this way, we will be able to translate the constraints that we make on the relativistic coefficients c_i into the actual relativistic theory. We will study the case for scalar and fermion DM.

2.4.1 Effective relativistic operators for fermion DM

Using only Dirac neutral DM fields χ and electron fields e, it is possible to construct the following basis of effective operators at dimension six [117]:

$$
\begin{aligned}
&\mathcal{O}_1 = \bar{\chi}\chi\bar{e}e, &&\mathcal{O}_2 = \bar{\chi}i\gamma^5\chi\bar{e}e, \\
&\mathcal{O}_3 = \bar{\chi}\chi\bar{e}i\gamma^5 e, &&\mathcal{O}_4 = \bar{\chi}i\gamma^5\chi\bar{e}i\gamma^5 e, \\
&\mathcal{O}_5 = \bar{\chi}\gamma^\mu\chi\bar{e}\gamma_\mu e, &&\mathcal{O}_6 = \bar{\chi}\gamma^\mu\gamma^5\chi\bar{e}\gamma_\mu e, \\
&\mathcal{O}_7 = \bar{\chi}\gamma^\mu\chi\bar{e}\gamma_\mu\gamma^5 e, &&\mathcal{O}_8 = \bar{\chi}\gamma^\mu\gamma^5\chi\bar{e}\gamma_\mu\gamma^5 e, \\
&\mathcal{O}_9 = \bar{\chi}\sigma^{\mu\nu}\chi\bar{e}\sigma_{\mu\nu} e, &&\mathcal{O}_{10} = \bar{\chi}i\sigma^{\mu\nu}\gamma^5\chi\bar{e}\sigma_{\mu\nu} e.
\end{aligned}
\tag{2.30}
$$

The operators listed in Eq. (2.30) are the only non-zero operators that respect gauge and Lorentz symmetry. In this list, we omitted the operators

$$
\bar{\chi}\sigma^{\mu\nu}\chi\bar{e}i\sigma_{\mu\nu}\gamma^5 e, \quad \bar{\chi}i\sigma^{\mu\nu}\gamma^5\chi\bar{e}i\sigma_{\mu\nu}\gamma^5 e,
\tag{2.31}
$$

because, thanks to the identity $i\sigma^{\mu\nu}\gamma^5 = -\frac{1}{2}\varepsilon^{\mu\nu\rho\tau}\sigma_{\rho\tau}$, those operators are respectively equal to $\mathcal{O}_{10}$ and $-\mathcal{O}_9$.

In the case of Majorana DM, the only non-zero bilinears are:

$$
\bar{\chi}\chi, \qquad \bar{\chi}\gamma^5\chi, \qquad \bar{\chi}\gamma^\mu\gamma^5\chi,
\tag{2.32}
$$

as, by applying the charge conjugate operator, we can see that $\bar{\chi}\gamma^\mu\chi$ and $\bar{\chi}\sigma^{\mu\nu}\chi$ must be zero [118].

To get the non-relativistic operators from the ones in Eq. (2.30) we can expand the solution of the Dirac equation in the non-relativistic limit:

$$
\begin{aligned}
u^s(p) &= \begin{pmatrix} \sqrt{p^\mu\sigma_\mu}\xi^s \\ \sqrt{p^\mu\bar{\sigma}_\mu}\xi^s \end{pmatrix} = \frac{1}{\sqrt{2(p^0+m)}} \begin{pmatrix} (p^\mu\sigma_\mu + m)\,\xi^s \\ (p^\mu\bar{\sigma}_\mu + m)\,\xi^s \end{pmatrix} \\
&= \frac{1}{\sqrt{4m}} \begin{pmatrix} (2m - \mathbf{p}\cdot\sigma)\xi^s \\ (2m + \mathbf{p}\cdot\sigma)\xi^s \end{pmatrix} + \mathcal{O}\left(\mathbf{p}^2\right),
\end{aligned}
$$

where $\sigma^\mu = (\mathbb{1}, \sigma)$, $\bar{\sigma}^\mu = (\mathbb{1}, -\sigma)$ and we approximate $p^\mu = (m, \mathbf{p}) + \mathcal{O}(\mathbf{p}^2)$ in the non-relativistic limit. In this way, we can rewrite the fermion bilinears in terms of their velocity, momentum and spin. At first order in the three-momenta, we get the following:

$$
\begin{aligned}
\bar{u}(p')u(p) &\simeq 2m, \\
\bar{u}(p')i\gamma^5 u(p) &\simeq 2i\mathbf{q}\cdot\mathbf{S}, \\
\bar{u}(p')\gamma^\mu u(p) &\simeq \begin{pmatrix} 2m \\ \mathbf{P} + 2i\mathbf{q}\times\mathbf{S} \end{pmatrix}, \\
\bar{u}(p')\gamma^\mu\gamma^5 u(p) &\simeq \begin{pmatrix} 2\mathbf{P}\cdot\mathbf{S} \\ 4m\mathbf{S} \end{pmatrix}, \\
\bar{u}(p')\sigma^{\mu\nu}u(p) &\simeq \begin{pmatrix} 0 & i\mathbf{q} - 2\mathbf{P}\times\mathbf{S} \\ -i\mathbf{q} + 2\mathbf{P}\times\mathbf{S} & 4m\varepsilon_{ijk}s^k \end{pmatrix}, \\
\bar{u}(p')i\sigma^{\mu\nu}\gamma^5 u(p) &\simeq \begin{pmatrix} 0 & -4m\mathbf{S} \\ 4m\mathbf{S} & i\varepsilon_{ijk}q_k - 2P_i s^j + 2P_j s^i \end{pmatrix},
\end{aligned}
\tag{2.33}
$$

where $\mathbf{P} = \mathbf{p} + \mathbf{p}'$. The spin operator is $\mathbf{S} \equiv \xi'^\dagger\frac{\sigma}{2}\xi$, and when it is not present, a $\xi'^\dagger\xi$ is implicit.

We can finally substitute Eq. (2.33) in the expressions of the relativistic operators in Eq. (2.30). Contracting the bilinears and taking the leading order in the non-relativistic expansion, we can finally rewrite the relativistic operators in terms of the basis of non-relativistic operators shown in Eq. (2.28):

$$
\begin{aligned}
\langle\mathcal{O}_1\rangle = \langle\mathcal{O}_5\rangle &= 4m_\chi m_e \mathcal{O}_1^{\mathrm{NR}}, \\
\langle\mathcal{O}_2\rangle &= -4m_e \mathcal{O}_{11}^{\mathrm{NR}}, \\
\langle\mathcal{O}_3\rangle &= 4m_\chi \mathcal{O}_{10}^{\mathrm{NR}}, \\
\langle\mathcal{O}_4\rangle &= 4\mathcal{O}_6^{\mathrm{NR}}, \\
\langle\mathcal{O}_6\rangle &= 8m_\chi \left(m_e \mathcal{O}_8^{\mathrm{NR}} + \mathcal{O}_9^{\mathrm{NR}}\right), \\
\langle\mathcal{O}_7\rangle &= 8m_e \left(-m_\chi \mathcal{O}_7^{\mathrm{NR}} + \mathcal{O}_9^{\mathrm{NR}}\right), \\
\langle\mathcal{O}_8\rangle = -\frac{1}{2}\langle\mathcal{O}_9\rangle &= -16m_\chi m_e \mathcal{O}_4^{\mathrm{NR}}, \\
\langle\mathcal{O}_{10}\rangle &= 8\left(m_\chi \mathcal{O}_{11}^{\mathrm{NR}} - m_e \mathcal{O}_{10}^{\mathrm{NR}} - 4m_\chi m_e \mathcal{O}_{12}^{\mathrm{NR}}\right).
\end{aligned}
\tag{2.34}
$$

From Eq. (2.34) we can see that more than one relativistic operator corresponds to the same non-relativistic operator, as the case for $\mathcal{O}_1$ and $\mathcal{O}_5$. Those contributions are therefore indistinguishable in direct detection experiments, which are only sensitive to the coefficient associated with the non-relativistic operator. For this reason, the bounds on the coefficients of the relativistic operators $\mathcal{O}_1$ and $\mathcal{O}_5$ are the same. Moreover, if a model has both $\mathcal{O}_1$ and $\mathcal{O}_5$ operators, which are associated with a scalar and a vector-mediated DM, cancellations or enhancements of the scattering cross section could arise, because they both contribute to the same non-relativistic coefficient.

2.4.2 Effective relativistic operators for scalar DM

Using scalar neutral DM fields ϕ and electron fields e, we can build the following basis of effective operators [117]:

$$
\begin{aligned}
\mathcal{O}_1 &= \phi^* \phi \bar{e} e, & \mathcal{O}_2 &= \phi^* \phi \bar{e} i \gamma^5 e, \\
\mathcal{O}_3 &= i \left(\phi^* \overleftrightarrow{\partial_\mu} \phi \right) \bar{e} \gamma^\mu e, & \mathcal{O}_4 &= i \left(\phi^* \overleftrightarrow{\partial_\mu} \phi \right) \bar{e} \gamma^\mu \gamma^5 e.
\end{aligned}
\tag{2.35}
$$

In the first line, the operators have dimension five, while in the second line, the operators have dimension six, and are equal to zero for a real field ϕ. Note that we have not considered the operator $\partial_\mu(\phi^*\phi)\bar{e}\gamma^\mu e$ because if we integrate by parts it is proportional to the divergence of the conserved current $\bar{e}\gamma^\mu e$, that vanishes when the electron in an external particle, according to the equations of motion for a fermion. The operator $\partial_\mu(\phi^*\phi)\bar{e}\gamma^\mu\gamma^5 e$ instead can be reduced to $2m_e\phi^*\phi\bar{e}i\gamma^5 e$ by integrating by parts and using the equations of motion for the electron field. This operator is therefore proportional to $\mathcal{O}_2$, so we do not need to add it to the list of operators.

As we did in the fermion DM case, we can match the matrix element of the relativistic operators to the non-relativistic ones. At leading order in the non-relativistic expansion, we obtain the following expressions:

$$
\begin{aligned}
\langle \mathcal{O}_1 \rangle &= 2m_e \mathcal{O}_1^{\mathrm{NR}}, \\
\langle \mathcal{O}_2 \rangle &= 2\mathcal{O}_{10}^{\mathrm{NR}}, \\
\langle \mathcal{O}_3 \rangle &= 4m_\chi m_e \mathcal{O}_1^{\mathrm{NR}}, \\
\langle \mathcal{O}_4 \rangle &= -8m_\chi m_e \mathcal{O}_7^{\mathrm{NR}}.
\end{aligned}
\tag{2.36}
$$

2.5 DM induced electronic transitions

In order to translate the direct detection measured events into limits for the Lagrangian parameters, we need to understand how the detector materials respond to the DM interaction. This response, also called *atomic response function*, is a function that can be described in terms of the overlap between the initial and final wave functions that describe the atom before and after the scattering [99].

We take the initial state $|i\rangle \equiv |\mathbf{e_1}, \mathbf{p}\rangle = |\mathbf{e_1}\rangle \otimes |\mathbf{p}\rangle$ and the final state $|f\rangle \equiv |\mathbf{e_2}, \mathbf{p'}\rangle = |\mathbf{e_2}\rangle \otimes |\mathbf{p'}\rangle$, where $|\mathbf{p}\rangle$ and $|\mathbf{p'}\rangle$ are the initial and final state of the DM particle, while $|\mathbf{e_1}\rangle$ and $|\mathbf{e_2}\rangle$ are the initial and final electron state. The electron states are eigenstates of the electron energy with eigenvalue E_1 and E_2, but are not eigenvalues of the electron momentum, because the electron is in a bound state. Single particle states are normalized such that

$$
\langle \mathbf{p}, \mathbf{p} \rangle = \langle \mathbf{e}_1, \mathbf{e}_2 \rangle = (2\pi)^3 \delta^{(3)}(0) = \int \mathrm{d}^3 x \equiv V.
\tag{2.37}
$$

The divergent volume V will not appear in the expression of physical observables.

Let's now take the first non-trivial term of the Dyson expansion of the S-matrix element that describes the transition $|i\rangle \to |f\rangle$:

$$
\begin{aligned}
S_{fi} &= -i\langle f| \int \mathrm{d}^4 x\, \mathscr{H}_I(x)|i\rangle \\
&= -i \int \mathrm{d}^4 x\, \langle \mathbf{p}', \mathbf{e}_2 \left| e^{iH_0 t} \mathscr{H}_S(x) e^{-iH_0 t} \right| \mathbf{e}_1, \mathbf{p} \rangle \\
&= -i \int \mathrm{d}^3 x\, \langle \mathbf{p}', \mathbf{e}_2 \left| \mathscr{H}_S(x) \right| \mathbf{e}_1, \mathbf{p} \rangle \int \mathrm{d}t\, e^{i(E_f - E_i)t} \\
&= -i(2\pi)\delta\left(E_f - E_i\right) \int \mathrm{d}^3 x\, \langle \mathbf{p}', \mathbf{e}_2 \left| \mathscr{H}_S(x) \right| \mathbf{e}_1, \mathbf{p} \rangle \\
&= -i(2\pi)\delta\left(E_f - E_i\right) \int \mathrm{d}^3 x \int \frac{\mathrm{d}^3 k}{(2\pi)^3} \int \frac{\mathrm{d}^3 k'}{(2\pi)^3} \langle \mathbf{e}_2 \mid \mathbf{k}' \rangle \langle \mathbf{k}', \mathbf{p}' \left| \mathscr{H}_S(x) \right| \mathbf{p}, \mathbf{k} \rangle \langle \mathbf{k} \mid \mathbf{e}_1 \rangle,
\end{aligned}
$$

(2.38)

where $\mathscr{H}_I(x)$ ($\mathscr{H}_S(x)$) is the interaction Hamiltonian density in the interaction (Schrodinger) picture in the spacetime point x, and H_0 is the free DM-e Hamiltonian such that: $H_0 |i\rangle = E_i |i\rangle$ and $H_0 |f\rangle = E_f |f\rangle$. In Eq. (2.38) the identity

$$
\int \frac{\mathrm{d}^3 k}{(2\pi)^3} |\mathbf{k}\rangle\langle\mathbf{k}| = \mathbb{1},
$$

(2.39)

has been used, where $|\mathbf{k}\rangle$ are eigenstates of the free-electron Hamiltonian. We use the adiabatic hypothesis, so $\mathscr{H}_I$ is assumed different from 0 only for a finite time window; for this reason the asymptotic states $|i\rangle$ and $|f\rangle$ are eigenstates of H_0 with eigenvalues E_i and E_f, which in the non-relativistic limit are equal to:

$$
\begin{aligned}
E_i &= m_\chi + m_e + \frac{m_\chi}{2} v^2 + E_1, \\
E_f &= m_\chi + m_e + \frac{|m_\chi \mathbf{v} - \mathbf{q}|^2}{2m_\chi} + E_2.
\end{aligned}
$$

(2.40)

We can then define $\Delta E_{1\to 2} \equiv E_2 - E_1$ as the energy difference between the two bound states. In the non-relativistic limit, using Eq. (2.40), we get that the energy difference $E_f - E_i$ is equal to:

$$
E_f - E_i = \Delta E_{1\to 2} + \frac{q^2}{2m_\chi} - qv \cos\theta_{qv},
$$

(2.41)

where θ_{qv} is the angle between $\mathbf{q}$ and $\mathbf{v}$. Let's now consider the elastic scattering $|\mathbf{k}, \mathbf{p}\rangle \to |\mathbf{k}', \mathbf{p}'\rangle$, between a DM particle with initial (final) momentum $\mathbf{p}$ ($\mathbf{p}'$) and a free electron particle with initial (final) momentum $\mathbf{k}$ ($\mathbf{k}'$). Let's now take the first non-trivial term

in the Dyson expansion of the S-matrix element of this process:

$$S_{fi}^{\text{free}} = -i(2\pi)\delta\left(\tilde{E}_f - \tilde{E}_i\right)\int d^3x\, \langle \mathbf{p}', \mathbf{k}' | \mathscr{H}_S(x) | \mathbf{k}, \mathbf{p} \rangle, \tag{2.42}$$

where $\tilde{E}_f \equiv E_{\mathbf{k}'} + E_{\mathbf{p}'}$ and $\tilde{E}_i \equiv E_{\mathbf{k}} + E_{\mathbf{p}}$. The S-matrix element can equivalently be expressed as follows

$$\begin{aligned}
S_{fi}^{\text{free}} &= i(2\pi)^4\delta\left(\tilde{E}_f - \tilde{E}_i\right)\delta^{(3)}\left(\mathbf{p}' + \mathbf{k}' - \mathbf{p} - \mathbf{k}\right) \\
&\times \frac{1}{\sqrt{2E_{\mathbf{p}'}2E_{\mathbf{k}'}2E_{\mathbf{k}}2E_{\mathbf{p}}}}\mathcal{M}\left(\mathbf{k}, \mathbf{p}, \mathbf{k}', \mathbf{p}'\right),
\end{aligned} \tag{2.43}$$

where $\mathcal{M}$ is the amplitude for DM-e scattering in which the electron is a free particle. The factor $1/\sqrt{2E_{\mathbf{p}'}2E_{\mathbf{k}'}2E_{\mathbf{k}}2E_{\mathbf{p}}}$ comes from the normalization of single-particle states, introduced in Eq. (2.37). Comparing Eq. (2.42) with Eq. (2.43), we get the following equation

$$\begin{aligned}
\int d^3x\, \langle \mathbf{p}', \mathbf{k}' | \mathscr{H}_S(x) | \mathbf{k}, \mathbf{p} \rangle &= -(2\pi)^3\delta^{(3)}\left(\mathbf{p}' + \mathbf{k}' - \mathbf{p} - \mathbf{k}\right) \\
&\times \frac{\mathcal{M}\left(\mathbf{k}, \mathbf{p}, \mathbf{k}', \mathbf{p}'\right)}{\sqrt{2E_{\mathbf{p}'}2E_{\mathbf{k}'}2E_{\mathbf{k}}2E_{\mathbf{p}}}}.
\end{aligned} \tag{2.44}$$

By substituting the free scattering result that we have obtained in Eq. (2.44) into the general S-matrix element in Eq. (2.38) and going into the non-relativistic limit, so $2E_{\mathbf{p}'}2E_{\mathbf{k}'}2E_{\mathbf{k}}2E_{\mathbf{p}} = 16m_\chi^2 m_e^2$, we obtain

$$\begin{aligned}
S_{fi} &= (2\pi)\delta\left(E_f - E_i\right)\frac{1}{4m_\chi m_e}\int\frac{d^3k}{(2\pi)^3}\langle \mathbf{e}_2 | \mathbf{k} + \mathbf{q} \rangle\langle \mathbf{k} | \mathbf{e}_1 \rangle \\
&\times i\mathcal{M}(\mathbf{k}, \mathbf{p}, \mathbf{k} + \mathbf{q}, \mathbf{p} - \mathbf{q}),
\end{aligned} \tag{2.45}$$

Using the normalized electron wave functions

$$\begin{aligned}
\psi_1(\mathbf{k}) &= \langle \mathbf{k} | \mathbf{e}_1 \rangle/\sqrt{V}, \\
\psi_2^*(\mathbf{k} + \mathbf{q}) &= \langle \mathbf{e}_2 | \mathbf{k} + \mathbf{q} \rangle/\sqrt{V},
\end{aligned} \tag{2.46}$$

we can rewrite Eq. (2.45) as follows

$$\begin{aligned}
S_{fi} &= (2\pi)\delta\left(E_f - E_i\right)\frac{V}{4m_\chi m_e}\int\frac{d^3k}{(2\pi)^3}\psi_2^*(\mathbf{k} + \mathbf{q})\psi_1(\mathbf{k}) \\
&\times i\mathcal{M}(\mathbf{k}, \mathbf{p}, \mathbf{k} + \mathbf{q}, \mathbf{p} - \mathbf{q}).
\end{aligned} \tag{2.47}$$

The probability for the transition $|\mathbf{e}_1, \mathbf{p}\rangle \to |\mathbf{e}_2, \mathbf{p}'\rangle$, taking into account the normalization of the single-particle states from Eq. (2.37), is given by $|S_{fi}|^2/V^4$.

The probability, $\mathscr{P}(\mathbf{p})$, that a DM particle with initial momentum $\mathbf{p}$ scatters with a bound electron in the $|e_1\rangle$ state into an interval of final states in which the DM momenta $\in (\mathbf{p}', \mathbf{p}' + \mathrm{d}\mathbf{p}')$ and the electron is in the state $|e_2\rangle$ is then given by $|S_{fi}|^2/V^4$ multiplied by the number of states in the $(\mathbf{p}' + \mathrm{d}\mathbf{p}')$ interval:

$$
\begin{aligned}
\mathscr{P}(\mathbf{p}) &= \frac{|S_{fi}|^2}{V^4} \frac{V \, \mathrm{d}^3 p'}{(2\pi)^3} = \frac{|S_{fi}|^2}{V^4} \frac{V \, \mathrm{d}^3 q}{(2\pi)^3} \\
&= (2\pi)\delta\left(E_f - E_i\right) \frac{T \, \mathrm{d}^3 q}{(2\pi)^3 V} \frac{1}{16 m_\chi^2 m_e^2} \times \left| \int \frac{\mathrm{d}^3 k}{(2\pi)^3} \psi_2^*(\mathbf{k} + \mathbf{q}) \mathcal{M}(\mathbf{k}, \mathbf{p}, \mathbf{q}) \psi_1(\mathbf{k}) \right|^2
\end{aligned}
$$
$$(2.48)$$

where $T = \int \mathrm{d}t$ is a divergent factor that arises when squaring the one-dimensional Dirac delta in Eq. (2.47), but physical observables, for example the interaction rate, will not depend on it. In order to simplify the notation, we replace $\mathcal{M}(\mathbf{k}, \mathbf{p}, \mathbf{k} + \mathbf{q}, \mathbf{p} - \mathbf{q})$ with $\mathcal{M}(\mathbf{k}, \mathbf{p}, \mathbf{q})$.

Now we can compute the rate per unit DM number density for the transition $|\mathbf{e}_1, \mathbf{p}\rangle \to |\mathbf{e}_2, \mathbf{p}'\rangle$ with $\mathbf{p}'$ within $(\mathbf{p}', \mathbf{p}' + \mathrm{d}\mathbf{p}')$. In fact, the rate is simply equal to $\mathscr{P}(\mathbf{p})V/T$.

To get the total rate of transition from $|\mathbf{e}_1\rangle$ to $|\mathbf{e}_2\rangle$ we just need to integrate $\mathscr{P}(\mathbf{p})V/T$ over the DM particle velocity distribution f_χ and the transferred momentum $\mathbf{q}$, and multiply by the local DM number density, n_χ^3, obtaining:

$$
\mathscr{R}_{1\to 2} = \frac{n_\chi}{16 m_\chi^2 m_e^2} \times \int \frac{\mathrm{d}^3 q}{(2\pi)^3} \int \mathrm{d}^3 v f_\chi(\mathbf{v})(2\pi)\delta\left(E_f - E_i\right) \overline{|\mathcal{M}_{1\to 2}|^2}, \tag{2.49}
$$

where $\overline{|\mathcal{M}_{1\to 2}|^2}$ is the squared electron transition amplitude, defined as

$$
\overline{|\mathcal{M}_{1\to 2}|^2} \equiv \overline{\left| \int \frac{\mathrm{d}^3 k}{(2\pi)^3} \psi_2^*(\mathbf{k} + \mathbf{q}) \mathcal{M}(\mathbf{k}, \mathbf{p}, \mathbf{q}) \psi_1(\mathbf{k}) \right|^2}, \tag{2.50}
$$

where a bar denotes an average over initial spin states and a sum over final spin states.

2.6   DM and Atomic Response Functions

In Eq. (2.29) we showed that it is possible to write the amplitude $\mathcal{M}$ of DM-e interaction in the non-relativistic limit as the linear combination of the non-relativistic operators, therefore, the amplitude $\mathcal{M}$ is dependent on $\mathbf{q}$ and $\mathbf{v}^\perp$. It is possible to rewrite the amplitude $\mathcal{M}$ in the following way:

$$
\mathcal{M}\left(\mathbf{q}, \mathbf{v}^\perp\right) = \mathcal{M}\left(\mathbf{q}, \mathbf{v}^\perp\right)_{\mathbf{k}=0} + \left(\frac{\mathbf{k}}{m_e}\right) \cdot m_e \nabla_{\mathbf{k}} \mathcal{M}\left(\mathbf{q}, \mathbf{v}^\perp\right)_{\mathbf{k}=0}. \tag{2.51}
$$

This is an exact approximation, as Eq. (2.29) is at most linear in $\mathbf{v}^\perp$. If we now substitute Eq. (2.51) into the squared transition amplitude in Eq. (2.50), we find

$$\overline{|\mathcal{M}_{1\to 2}|^2} = \left\{ \overline{|\mathcal{M}(\mathbf{q}, \mathbf{v}^\perp)|^2} \, |f_{1\to 2}(\mathbf{q})|^2 \right.$$
$$+ 2m_e \overline{\Re\left[\mathcal{M}(\mathbf{q}, \mathbf{v}^\perp) f_{1\to 2}(\mathbf{q}) \nabla_{\mathbf{k}} \mathcal{M}^*(\mathbf{q}, \mathbf{v}^\perp) \cdot \mathbf{f}_{1\to 2}^*(\mathbf{q})\right]} \qquad (2.52)$$
$$\left. + m_e^2 \, \overline{|\nabla_{\mathbf{k}} \mathcal{M}(\mathbf{q}, \mathbf{v}^\perp) \cdot \mathbf{f}_{1\to 2}(\mathbf{q})|^2} \right\}_{\mathbf{k}=0}.$$

This is the most general expression for the squared transition amplitude, taking into account all the degrees of freedom of the DM-e interaction.

In the case in which the scattering amplitude depends only on $\mathbf{q}$, we can take out $\mathcal{M}(\mathbf{q})$ from the integral in Eq. (2.49), and only the first term in Eq. (2.52) contributes to the squared transition amplitude $\overline{|\mathcal{M}_{1\to 2}|^2}$. We can see that this standard assumption $\mathcal{M} = \mathcal{M}(\mathbf{q})$ is very convenient because it implies a factorization of atomic physics and DM physics. Following the notation of Ref. [105], for $\mathcal{M} = \mathcal{M}(\mathbf{q})$, we can define a scalar atomic form factor

$$f_{1\to 2}(\mathbf{q}) = \int \frac{\mathrm{d}^3 k}{(2\pi)^3} \psi_2^*(\mathbf{k} + \mathbf{q}) \psi_1. \qquad (2.53)$$

The transition amplitude, $\mathcal{M}_{1\to 2}(\mathbf{q})$, can be obtained by multiplying the free scattering amplitude by the form factor $f_{1\to 2}(\mathbf{q})$

$$\mathcal{M}_{1\to 2}(\mathbf{q}) = \mathcal{M}(\mathbf{q}) \times f_{1\to 2}(\mathbf{q}). \qquad (2.54)$$

The momentum space wave functions ψ_1 and ψ_2 have dimension $[\text{energy}]^{-3/2}$, therefore $f_{1\to 2}(\mathbf{q})$ is a dimensionless quantity.

In the general approach, in which the transition amplitude depends on both the transferred momentum and the velocity $\mathbf{v}_\perp$, we get both the scalar form factor of Eq. (2.53) and a vectorial atomic form factor, that appears in Eq. (2.52),

$$\mathbf{f}_{1\to 2}(\mathbf{q}) = \int \frac{\mathrm{d}^3 k}{(2\pi)^3} \psi_2^*(\mathbf{k} + \mathbf{q}) \left(\frac{\mathbf{k}}{m_e}\right) \psi_1(\mathbf{k}). \qquad (2.55)$$

The details of the evaluation of the scalar, $f_{1\to 2}$, and vectorial, $\mathbf{f}_{1\to 2}$, atomic form factors are presented in Ref. [99].

Until now we treated the DM-e scattering in a general way, in terms of initial and final state electron wave functions, ψ_1 and ψ_2, respectively. From now, however, we will focus on the case of DM-induced ionization of isolated atoms. This means that the initial state (formerly simply denoted by "1") is a bound state characterized by the principal, angular and magnetic quantum numbers (n, ℓ, m), while in the final state ("2") the electron is not bound to the atom, but still affected by the remaining ion's presence close by. The final state is defined by the quantum numbers (k', ℓ', m'), where k' is the asymptotic

momentum of the electron and ℓ', m' are its angular and magnetic quantum numbers.
In this case the total ionization rate $\mathscr{R}_{\text{ion}}^{n\ell}$ of a full atomic orbital (n, ℓ) can be obtained by summing the transition rate $\mathscr{R}_{1\to2}$ over all occupied initial electron states and by integrating over the allowed final electron states. For what concerns the sum over the initial electron states, the rate has to be summed over all values of the magnetic quantum number m and multiplied by 2 to account for the spin degeneracy. Then we need to sum over all the allowed electron final states; this is achieved by acting on $\mathscr{R}_{1\to2}$ with the integral operator [105]

$$\frac{V}{2} \sum_{\ell'=0}^{\infty} \sum_{m'=-\ell'}^{\ell'} \int \frac{k'^3 \, \mathrm{d}\ln E_e}{(2\pi)^3}. \tag{2.56}$$

where, $E_e = k'^2/(2m_e)$ is the ionized electron's final energy, and $V \, \mathrm{d}^3 k'/(2\pi)^3$ is the number of final states with asymptotic momentum between $\mathbf{k}'$ and $\mathbf{k}'+\mathrm{d}\mathbf{k}'$. Summarizing, the total ionization rate for the (n, ℓ) orbital is given by

$$\mathscr{R}_{\text{ion}}^{n\ell} = \sum_{m=-\ell}^{\ell} \sum_{\ell'=0}^{\infty} \sum_{m'=-\ell'}^{\ell'} \int \mathrm{d}\ln E_e \frac{V k'^3}{(2\pi)^3} \mathscr{R}_{1\to2}, \tag{2.57}$$

and the associated final state electron ionization energy spectrum by

$$\frac{\mathrm{d}\mathscr{R}_{\text{ion}}^{n\ell}}{\mathrm{d}\ln E_e} = \sum_{m=-\ell}^{\ell} \sum_{\ell'=0}^{\infty} \sum_{m'=-\ell'}^{\ell'} \frac{V k'^3}{(2\pi)^3} \mathscr{R}_{1\to2}. \tag{2.58}$$

It can be shown that the divergent factor V in Eq. (2.58) cancels with the $1/V$ factor that comes from the normalization of $\psi_{k'm'\ell'}$. Substituting Eq. (2.49), we can rewrite the rate as

$$\frac{\mathrm{d}\mathscr{R}_{\text{ion}}^{n\ell}}{\mathrm{d}\ln E_e} = \frac{n_\chi}{128\pi m_\chi^2 m_e^2} \times \int \mathrm{d}q \, q \int \frac{\mathrm{d}^3 v}{v} f_\chi(\mathbf{v}) \Theta(v - v_{\min}) \overline{|\mathcal{M}_{\text{ion}}^{n\ell}|^2}, \tag{2.59}$$

where $v_{\min}$ is defined in Eq. (2.24) and, following [105], we integrated over $\cos\theta_{qv}$ while assuming that $f_\chi(\mathbf{v}) = f_\chi(v)$, and then replaced $f_\chi(v)$ with $f_\chi(\mathbf{v})$ in the final expression[1]. The squared ionization amplitude, $\overline{|\mathcal{M}_{\text{ion}}^{n\ell}|^2}$, present in Eq. (2.59) is defined as

$$\overline{|\mathcal{M}_{\text{ion}}^{n\ell}|^2} \equiv V \frac{4k'^3}{(2\pi)^3} \sum_{m=-\ell}^{\ell} \sum_{\ell'=0}^{\infty} \sum_{m'=-\ell'}^{\ell'} \overline{|\mathcal{M}_{1\to2}|^2}. \tag{2.60}$$

We can express it explicitly in terms of the amplitude $\mathcal{M}(\mathbf{q}, \mathbf{v}^\perp)$ as follows

---

[1]In this way we get a simplified evaluation of Eq. (2.49). This is justified by the fact that we are not interested in a directional analysis of the predicted signal.

$$
\overline{\left|\mathcal{M}_{\text{ion}}^{n\ell}\right|^2} = \left\{ \left|\mathcal{M}\left(\mathbf{q}, \mathbf{v}^\perp\right)\right|^2 \left|f_{\text{ion}}^{n\ell}\left(k', q\right)\right|^2 \right.
$$

$$
+ V \frac{4k'^3}{(2\pi)^3} \sum_{m=-\ell}^{\ell} \sum_{\ell'=0}^{\infty} \sum_{m'=-\ell'}^{\ell'} \left[2m_e \overline{\Re\left[\mathcal{M}\left(\mathbf{q}, \mathbf{v}^\perp\right) f_{1\to2}(\mathbf{q}) \nabla_{\mathbf{k}} \mathcal{M}^*\left(\mathbf{q}, \mathbf{v}^\perp\right) \cdot \mathbf{f}_{1\to2}^*(\mathbf{q})\right]} \right.
$$

$$
\left. \left. + m_e^2 \overline{\left|\nabla_{\mathbf{k}} \mathcal{M}\left(\mathbf{q}, \mathbf{v}^\perp\right) \cdot \mathbf{f}_{1\to2}(\mathbf{q})\right|^2}\right] \right\}_{\mathbf{k}=0;\, \mathbf{v}\cdot\mathbf{q}/(qv)=\xi},
$$

(2.61)

where $\xi = \Delta E_{1\to2}/(qv) + q/(2m_\chi v)$ and $f_{\text{ion}}^{n\ell}\left(k', q\right)$ is the dimensionless ionization form factor

$$
\left|f_{\text{ion}}^{n\ell}\left(k', q\right)\right|^2 = V \frac{4k'^3}{(2\pi)^3} \sum_{\ell'=0}^{\infty} \sum_{m=-\ell}^{\ell} \sum_{m'=-\ell'}^{\ell'} \left|f_{1\to2}(q)\right|^2.
$$

(2.62)

This ionization form factor is shown in Fig. 2.3 for the outer shell of the xenon atom.
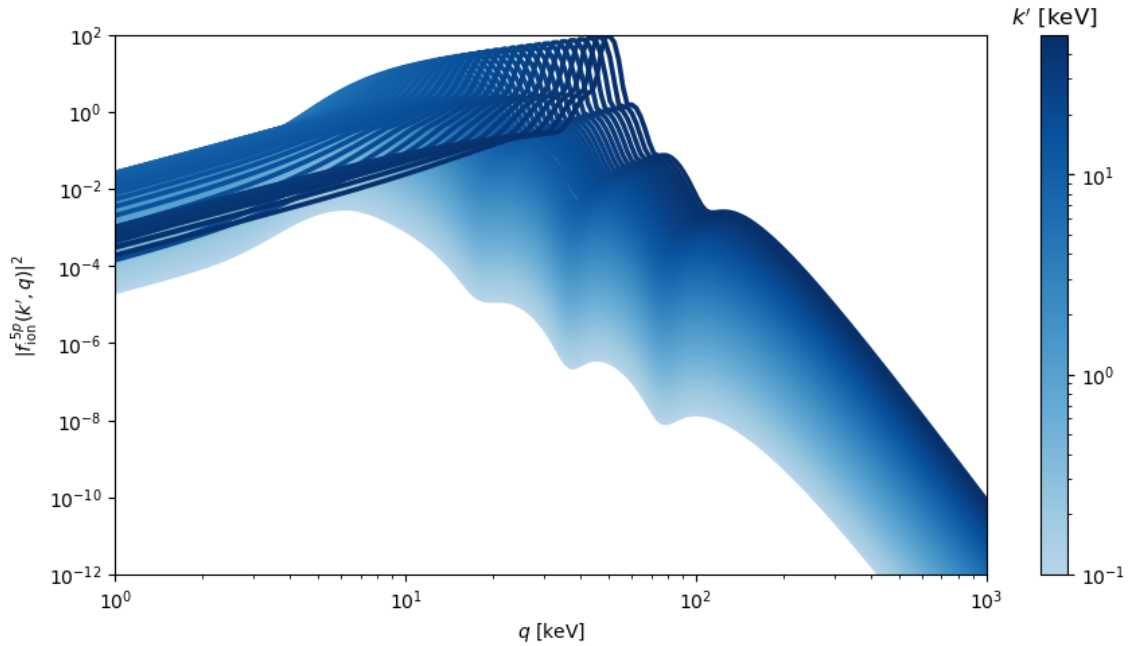

Figure 2.3: Ionization form factor $\left|f_{\text{ion}}^{n\ell}\left(k', q\right)\right|^2$ defined in Eq. (2.62) for the electron orbital 5p of xenon.

Note that, to compute the ionization form factor, the wave functions of the initial and final state electrons are expanded into spherical harmonics:

40

$$\psi_{n\ell m}(\mathbf{x}) = R_{n\ell}(r)Y_\ell^m(\theta, \phi),$$
$$\psi_{k'\ell'm'}(\mathbf{x}) = R_{k'\ell'}(r)Y_{\ell'}^{m'}(\theta, \phi),$$

(2.63)

where the radial parts $R_{n\ell}(r)$ and $R_{k'\ell'}(r)$ describe isolated argon and xenon atoms, and are given in Appendix B 4 of Ref. [99]. Notice that, even if those radial functions are not applicable to dense liquid argon and xenon systems, they are a good approximation and have been used in previous direct detection analysis of DM [89]. This is due to the fact that the electron binding energies in liquid nobles are smaller than those of the isolated atoms, so we expect the effect on theoretical predictions on DM rate to be negligible.

In order to use this framework for numerical applications, as we will do later in this thesis, we need to rewrite these equations in a more compact form. The squared ionization amplitude, $\overline{\left|\mathcal{M}_{\mathrm{ion}}^{n\ell}\right|^2}$, can be written in the following way:

$$\overline{\left|\mathcal{M}_{\mathrm{ion}}^{n\ell}\right|^2} = \sum_{i=1}^{4} R_i^{n\ell}\left(\mathbf{v}^\perp, \frac{\mathbf{q}}{m_e}\right) W_i^{n\ell}(k', \mathbf{q}).$$

(2.64)

Each term on the sum is factorized into two functions: $R_i^{n\ell}\left(\mathbf{v}_{\mathrm{el}}^\perp, \frac{\mathbf{q}}{m_e}\right)$ are the *DM response functions*. Those functions depend on the couplings of Eq. (2.29), therefore those are the pieces that contain all the information about the DM-electron interaction.

$W_i^{n\ell}(k', \mathbf{q})$ are called *atomic response functions*, and carry all the information regarding the electron initial and final state wave functions. Thanks to Eq. (2.64), we are able to disentangle the particle physics input from that of the atomic physics. The final expression of the four DM and atomic response functions is[2]:

---

[2]Their detailed derivations can be found in Appendixes A and B of Ref. [99].

$$R_1^{n\ell}\left(\mathbf{v}^\perp, \frac{\mathbf{q}}{m_e}\right) \equiv c_1^2 + \frac{c_3^2}{4}\left(\frac{\mathbf{q}}{m_e}\right)^2 (\mathbf{v}^\perp)^2 - \frac{c_3^2}{4}\left(\frac{\mathbf{q}}{m_e}\cdot\mathbf{v}^\perp\right)^2 + \frac{c_7^2}{4}(\mathbf{v}^\perp)^2 + \frac{c_{10}^2}{4}\left(\frac{\mathbf{q}}{m_e}\right)^2$$

$$+ \frac{j_\chi(j_\chi+1)}{12}\left\{3c_4^2 + c_6^2\left(\frac{\mathbf{q}}{m_e}\right)^4 + (4c_8^2 + 2c_{12}^2)(\mathbf{v}^\perp)^2 + \right.$$

$$\left(2c_9^2 + 4c_{11}^2 + 2c_4 c_6\right)\left(\frac{\mathbf{q}}{m_e}\right)^2 + (4c_5^2 + c_{13}^2 + c_{14}^2 - 2c_{12}c_{15})\left(\frac{\mathbf{q}}{m_e}\right)^2 (\mathbf{v}^\perp)^2$$

$$+ c_{15}^2\left(\frac{\mathbf{q}}{m_e}\right)^4 (\mathbf{v}^\perp)^2 - c_{15}^2\left(\frac{\mathbf{q}}{m_e}\right)^2\left(\mathbf{v}^\perp\cdot\frac{\mathbf{q}}{m_e}\right)^2$$

$$\left. + \left(-4c_5^2 + 2c_{13}c_{14} + 2c_{12}c_{15}\right)\left(\mathbf{v}^\perp\cdot\frac{\mathbf{q}}{m_e}\right)^2\right\},$$

$$R_2^{n\ell}\left(\mathbf{v}^\perp, \frac{\mathbf{q}}{m_e}\right) \equiv \left(\frac{\mathbf{q}}{m_e}\cdot\mathbf{v}^\perp\right)\left[-\frac{c_7^2}{2}\left(\frac{\mathbf{q}}{m_e}\right)^{-2} - \frac{j_\chi(j_\chi+1)}{6}\left\{(4c_8^2 + 2c_{12}^2)\left(\frac{\mathbf{q}}{m_e}\right)^{-2}\right.\right.$$

$$\left.\left. + (c_{13} + c_{14})^2\right\}\right],$$

$$R_3^{n\ell}\left(\mathbf{v}^\perp, \frac{\mathbf{q}}{m_e}\right) \equiv \frac{c_3^2}{4}\left(\frac{\mathbf{q}}{m_e}\right)^2 + \frac{c_7^2}{4} + \frac{j_\chi(j_\chi+1)}{12}\left\{4c_8^2 + 2c_{12}^2\right.$$

$$\left. + (4c_5^2 + c_{13}^2 + c_{14}^2 - 2c_{12}c_{15})\left(\frac{\mathbf{q}}{m_e}\right)^2 + c_{15}^2\left(\frac{\mathbf{q}}{m_e}\right)^4\right\},$$

$$R_4^{n\ell}\left(\mathbf{v}^\perp, \frac{\mathbf{q}}{m_e}\right) \equiv -\frac{c_3^2}{4} + \frac{j_\chi(j_\chi+1)}{12}\left\{-4c_5^2 - c_{15}^2\left(\frac{\mathbf{q}}{m_e}\right)^2 + 2c_{12}c_{15} + 2c_{13}c_{14}\right\},$$

$$\tag{2.65}$$

where c_i are the non-relativistic coefficients of Eq. (2.29). The dependence on the (n, ℓ) quantum numbers comes through the dependence of $v_{\rm el}^\perp$ on the binding energy of the shell: in fact, it is possible to see that, thanks to the conservation of energy and using Eq. (2.40), we obtain

$$\mathbf{v}\cdot\mathbf{q} = \Delta E_{1\to 2} + \frac{q^2}{2m_\chi}. \tag{2.66}$$

Replacing Eq. (2.66) into the definition of $\mathbf{v}_\perp$ (Eq. (2.26)), we get that

$$\left.(\mathbf{v}^\perp)^2\right|_{k=0} = v^2 + \frac{q^2}{4\mu_e^2}\frac{m_\chi - m_e}{m_e + m_\chi} - \frac{\Delta E_{1\to 2}}{\mu_e}, \tag{2.67}$$

where in this case $\Delta E_{1\to2} = E_B + k'^2/(2m_e)$. In the above expressions, $\mathbf{v}^\perp$ is evaluated at $\mathbf{k} = \mathbf{0}$ due to the non-relativistic expansion of $\mathcal{M}$.

The expression of the four atomic response functions is the following one:

$$W_1^{n\ell}(k',\mathbf{q}) \equiv V\frac{4k'^3}{(2\pi)^3}\sum_{m=-\ell}^{\ell}\sum_{\ell'=0}^{\infty}\sum_{m'=-\ell'}^{\ell'}|f_{1\to2}(q)|^2,$$

$$W_2^{n\ell}(k',\mathbf{q}) \equiv V\frac{4k'^3}{(2\pi)^3}\times\sum_{m=-\ell}^{\ell}\sum_{\ell'=0}^{\infty}\sum_{m'=-\ell'}^{\ell'}\frac{\mathbf{q}}{m_e}\cdot f_{1\to2}(\mathbf{q})\mathbf{f}_{1\to2}^*(\mathbf{q}),$$

$$W_3^{n\ell}(k',\mathbf{q}) \equiv V\frac{4k'^3}{(2\pi)^3}\sum_{m=-\ell}^{\ell}\sum_{\ell'=0}^{\infty}\sum_{m'=-\ell'}^{\ell'}|\mathbf{f}_{1\to2}(\mathbf{q})|^2,$$

$$W_4^{n\ell}(k',\mathbf{q}) \equiv V\frac{4k'^3}{(2\pi)^3}\times\sum_{m=-\ell}^{\ell}\sum_{\ell'=0}^{\infty}\sum_{m'=-\ell'}^{\ell'}\left|\frac{\mathbf{q}}{m_e}\cdot\mathbf{f}_{1\to2}(\mathbf{q})\right|^2.$$

(2.68)

The first atomic response function $W_1^{n\ell}(k',\mathbf{q})$ can be identified with the ionization form factor $\left|f_{\text{ion}}^{n\ell}(k',q)\right|^2$ that usually appears in sub-GeV DM detection literature [105]. Figure 2.6 shows the four atomic response functions, $W_j^{n\ell}, j = 1,\ldots,4$, for the xenon 5p atomic orbital.

The physical meaning of the atomic response functions can be understood by evaluating them in the plane wave limit, where we take the initial and final wave functions equal to the eigenstates of the electron momentum operator

$$\psi_1(\mathbf{x}) = \exp(i\mathbf{k}\cdot\mathbf{x})/\sqrt{V},$$
$$\psi_2(\mathbf{x}) = \exp(i\mathbf{k}'\cdot\mathbf{x})/\sqrt{V},$$

(2.69)

with eigenvalues $\mathbf{k}$ and $\mathbf{k}'$ respectively. In this limit, initial and final state electron states describe free particles, that are not bound to the atom. Substituting $\psi_1(\mathbf{x})$ and $\psi_2(\mathbf{x})$ in Eqs. (2.68), we obtain the following expressions

$$|f_{1\to2}(\mathbf{q})|^2 = \frac{(2\pi)^3}{V}\delta^{(3)}(\mathbf{q}+\mathbf{k}-\mathbf{k}'),\tag{2.70a}$$

$$\frac{\mathbf{q}}{m_e}\cdot f_{1\to2}(\mathbf{q})\mathbf{f}_{1\to2}(\mathbf{q}) = -\left(\frac{\mathbf{k}}{m_e}\cdot\frac{\mathbf{q}}{m_e}\right)\times\frac{(2\pi)^3}{V}\delta^{(3)}(\mathbf{q}+\mathbf{k}-\mathbf{k}'),\tag{2.70b}$$

$$|\mathbf{f}_{1\to2}(\mathbf{q})|^2 = \left|\frac{\mathbf{k}}{m_e}\right|^2\frac{(2\pi)^3}{V}\delta^{(3)}(\mathbf{q}+\mathbf{k}-\mathbf{k}'),\tag{2.70c}$$

$$\left|\frac{\mathbf{q}}{m_e}\cdot\mathbf{f}_{1\to2}(\mathbf{q})\right|^2 = \left|\frac{\mathbf{k}}{m_e}\cdot\frac{\mathbf{q}}{m_e}\right|^2\times\frac{(2\pi)^3}{V}\delta^{(3)}(\mathbf{q}+\mathbf{k}-\mathbf{k}').\tag{2.70d}$$
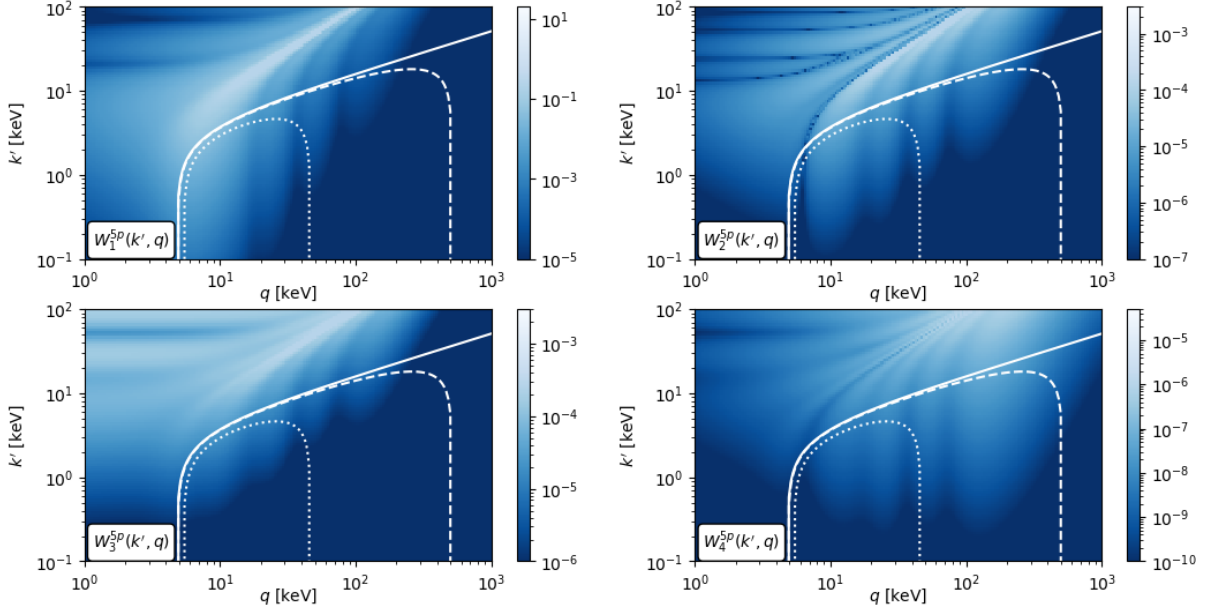
Figure 2.4: The four atomic responses for the outer atomic orbital of xenon. Over the atomic response, there are three white lines (dotted/dashed/solid) that delimit the region in which the minimum speed $v_{\min}$ in Eq. (2.24) exceeds the maximum speed $v_{\max} = v_{\text{earth}} + v_{\text{esc}}$ for a DM mass of respectively $10\text{MeV}/100\text{MeV}/ \rightarrow \infty$. The top left panel shows the same function as the left panel of Fig. 2.3, but now with the final state electron asymptotic momentum k' on the y-axis. Note the different colour bar scales in the four panels.

In the plane-wave limit, it is possible to define a laboratory frame in which $\mathbf{k} = 0$, meaning that the initial electron is at rest. In this frame, Eqs. (2.70b, 2.70c, 2.70d) are equal to 0, therefore $W_j^{n\ell}(k', \mathbf{q}) = 0$ for $j = 2, 3, 4$, and Eq. (2.64) reduces to the expression for the modulus squared of the amplitude for DM scattering by a point-like particle, as it is shown in Ref. [119] in the case of a proton target. So we see that the first atomic response function describes the contact interaction with the electron, which will be used in the rest of this thesis. The other three atomic response functions describe distortions in the ionization spectrum induced by the fact that the initial state electron is not at rest and obeys a momentum distribution with a finite dispersion, being the electron bound to an atom.

Chapter 3

Direct Detection of DM with MADDM

In the previous chapter, we saw how to compute the ionization rate caused by the interaction with a DM particle. To compute the rate, we need to know the coefficients c_i that describe the interacting Lagrangian in the non-relativistic limit, as shown in Eq. (2.27). The non-relativistic operators can be matched with the relativistic ones, as shown in section 2.4.

BSM theories that describe DM particles are written in terms of high energy theories that describe the DM-electron interaction through a mediator, and up to this date, a very large number of models has been proposed. The process of matching these models to EFTs, and then to NREFT in order to compute the rate of DM scattering as shown in the previous section would be extremely impractical for an analytical analysis of different DM models. In addition to that, in order to make constraints on the Lagrangian parameters, the ionization rate must be converted into the expected signal in direct detection experiment, that one can finally compare with the measured one by evaluating the p-value for each set of parameters of the assumed model. In order to make this type of analysis, the use of numerical tools is mandatory.

In this thesis, we focus on the numerical tool MADDM [120], in which we automatized the full procedure described above in the case of DM-electron scattering. In this chapter, we outline the full procedure that has been implemented.

We start with a brief introduction of MADDM, followed by the description of the projection operator method for extraction of low energy coefficients, used in MADDM to obtain the coefficients of the effective field theory that describes the full model inserted by the user in Unified FEYNRULES Output (UFO) format [121], that is a set of Python files that can be imported in MADGRAPH5_AMC@NLO. After that, we show how the rate is computed and transformed into the expected signal, taking into account the specifics of the XENON10 and XENON1T experiments. At the end of the chapter, we describe how the p-value evaluation was implemented using the number of events measured by those experiments, and how it is used to make exclusion limits on the Lagrangian parameters.

3.1 Introduction on MADDM

MADDM is a computational software capable of calculating observables related to DM for any DM model in UFO format. The initial version [122] allowed for the computation of the relic density. The second release [123] included the calculation of the DM-nucleon cross-section, as well as the double differential event rates of nuclear recoils in a generic Xe experiment. Additionally, it integrates the LUX experimental likelihoods [124].

The most recent version of MADDM includes an indirect detection module that enables the computation of observables related to DM annihilation and loop induced processes. This feature allows for the prediction of the fluxes of neutrinos and gamma rays originating from the annihilation of DM in the Milky Way or dwarf spheroidal galaxies. MADDM is used as a plugin for MADGRAPH5_AMC@NLO, thereby inheriting its capabilities. Moreover, MADDM has introduced a novel functionality known as the experiment module, which allows testing of different model points against experimental constraints for direct and indirect detection. For indirect detection, MADDM has incorporated the FERMI-LAT likelihood for prompt γ-rays detected in dwarf spheroidal galaxies analysis. In the case of direct detection for nuclear recoil, the exclusion limits include XENON1T and LUX for spin-independent cross-section, while for spin-dependent cross-section, the limits are set by LUX and Pico60, respectively. More detailed information regarding the capabilities of MADDM can be found in Ref. [120].

In this thesis, we add the capability to evaluate DM-e scattering in MADDM, and to produce limits based on XENON10 and XENON1T. In this way, we can analyse the region of light DM mass, opening the possibility to study a greater variety of theoretical models.

3.2 Computation of low energy coefficients

Given a Lagrangian that describes the interactions between DM and electrons, it is possible to rewrite it as a linear combination of effective orthogonal operators in the low-energy limit, where the exchanged momentum Q^2 goes to 0 [123], as follows:

$$\mathcal{L}_{Q^2=0} = \sum_i \alpha_i \mathcal{O}_i, \tag{3.1}$$

where the operators $\mathcal{O}_i$ stand for four point DM-e interactions and are defined in Table 3.1, while α_i are multiplicative coefficients. The list of operators is divided into even (e) and odd (o) operators: under the interchange of electrons with positrons (and vice versa) the odd operators changes sign, while the even operators do not change sign. Furthermore, we distinguish between spin-dependent (SI) and spin-independent (SD) operators, described in section 1.3.3. For DM-e interactions, the SD interactions are only suppressed by a multiplicative constant proportional to the spin of the interacting

	DM spin	Even	Odd
		scalar current	vector current
	0	$2M_\chi \phi\phi^* \bar{\psi}_e \psi_e$	$i\left(\partial_\mu\phi\phi^* - \phi\partial_\mu\phi^*\right)\bar{\psi}_e\gamma^\mu\psi_e$
SI	1/2	$\bar{\psi}_\chi\psi_\chi\bar{\psi}_e\psi_e$	$\bar{\psi}_\chi\gamma_\mu\psi_\chi\bar{\psi}_e\gamma^\mu\psi_e$
	1	$2M_\chi A^*_{\chi\mu}A^\mu_\chi\bar{\psi}_e\psi_e$	$i\left(A^{*\alpha}_\chi\partial_\mu A_{\chi\alpha} - A^\alpha_\chi\partial_\mu A^*_{\chi\alpha}\right)\bar{\psi}_e\gamma_\mu\psi_e$
		axial-vector current	tensor current
	1/2	$\bar{\psi}_\chi\gamma^\mu\gamma^5\psi_\chi\bar{\psi}_e\gamma_\mu\gamma_5\psi_e$	$-\frac{1}{2}\bar{\psi}_\chi\sigma_{\mu\nu}\psi_\chi\bar{\psi}_e\sigma^{\mu\nu}\psi_e$
SD	1	$\sqrt{6}\left(\partial_\alpha A^*_{\chi\beta}A_{\chi\nu} - A^*_{\chi\beta}\partial_\alpha A_{\chi\nu}\right)\epsilon^{\alpha\beta\nu\mu}\bar{\psi}_e\gamma_5\gamma_\mu\psi_e$	$i\frac{\sqrt{3}}{2}\left(A_{\chi\mu}A^*_{\chi\nu} - A^*_{\chi\mu}A_{\chi\nu}\right)\bar{\psi}_e\sigma^{\mu\nu}\bar{\psi}_e$

Table 3.1: Most relevant effective operators for scalar ϕ, fermion ψ_χ and vector A_χ DM fields [125].

particles. In the case of scalar DM, SD interactions are forbidden. The table only shows the operators that give relevant contributions at $Q^2 = 0$, and are the ones that will be considered in the rest of this analysis. We can rewrite Eq. (3.1) as:

$$\mathcal{L}_{Q^2=0} = (\mathcal{L}^e_{SI} + \mathcal{L}^o_{SI}) + (\mathcal{L}^e_{SD} + \mathcal{L}^o_{SD}) = \sum_s \alpha^{SI}_s \mathcal{O}^{SI}_{e,s} + \sum_s \alpha^{SD}_s \mathcal{O}^{SD}_{e,s}, \qquad (3.2)$$

where $s = e, o$. The matrix element $\mathcal{M}$ resulting from this Lagrangian can be projected via a Fiertz transformation into the set of effective operators, and we use this transformation to get the α_s coefficients. This procedure is equivalent to taking the interference term of the full matrix element $\mathcal{M}$ for DM-e scattering with an effective operator matrix element $\mathcal{M}_{\text{eff}}$ for the same process:

$$\alpha_e + \alpha_o = \frac{|\mathcal{M}^{f*} \cdot \mathcal{M}^{f,e}_{\text{eff}}|}{|\mathcal{M}^{f,e}_{\text{eff}}|^2}, \qquad (3.3)$$

where f stands for fermion (referred to the electron). We can use the even and odd propriety of the operators $\mathcal{O}_i$ inside $\mathcal{M}_{\text{eff}}$ to get the same expression but for DM-positron scattering:

$$\alpha_e - \alpha_o = \frac{|\mathcal{M}^{\bar{f}*} \cdot \mathcal{M}^{\bar{f},e}_{\text{eff}}|}{|\mathcal{M}^{\bar{f},e}_{\text{eff}}|^2}, \qquad (3.4)$$

where $\bar{f}$ stands for anti-fermion (referred to the positron). Since the basis of operators is orthogonal, the projection into the effective operators will also select either SI or SD

operators. Notice that the interference is computed only using the matrix element from the even effective operator. We could also compute the interference using the odd one. In this case, Eq. (3.3) remains the same (with $\mathcal{M}^{\bar{f},o}$ instead of $\mathcal{M}^{\bar{f},e}$), while Eq. (3.4) becomes

$$\alpha_o - \alpha_e = \frac{|\mathcal{M}^{\bar{f}*} \cdot \mathcal{M}_{\text{eff}}^{\bar{f},o}|}{|\mathcal{M}_{\text{eff}}^{\bar{f},o}|^2}. \tag{3.5}$$

By adding and subtracting Eq. (3.3) and (3.4) we finally obtain the effective coefficients:

$$\alpha_e = \frac{1}{2} \left(\frac{|\mathcal{M}^{f*} \cdot \mathcal{M}_{\text{eff}}^{f,e}|}{|\mathcal{M}_{\text{eff}}^{f,e}|^2} + \frac{|\mathcal{M}^{\bar{f}*} \cdot \mathcal{M}_{\text{eff}}^{\bar{f},e}|}{|\mathcal{M}_{\text{eff}}^{\bar{f},e}|^2} \right), \tag{3.6}$$

$$\alpha_o = \frac{1}{2} \left(\frac{|\mathcal{M}^{f*} \cdot \mathcal{M}_{\text{eff}}^{f,e}|}{|\mathcal{M}_{\text{eff}}^{f,e}|^2} - \frac{|\mathcal{M}^{\bar{f}*} \cdot \mathcal{M}_{\text{eff}}^{\bar{f},e}|}{|\mathcal{M}_{\text{eff}}^{\bar{f},e}|^2} \right). \tag{3.7}$$

3.3   Derivation of the expected signal with MADDM

The BSM models, including the even effective operators for fermion and scalar DM shown in Table 3.1 have been built in UFO format, that can be read by MADDM. The code implemented in this thesis has instructed MADDM to take the user model for DM-e and match it with the EFT model. Then the interference term shown in Eq. (3.3) is computed as:

$$\frac{|\mathcal{M}^{f*} \cdot \mathcal{M}_{\text{eff}}^{f,e}|}{|\mathcal{M}_{\text{eff}}^{f,e}|^2} = \frac{1}{2} \frac{|\mathcal{M}_{\text{tot}}^{f}|^2 - |\mathcal{M}^{f}|^2 - |\mathcal{M}_{\text{eff}}^{f,e}|^2}{|\mathcal{M}_{\text{eff}}^{f,e}|^2}, \tag{3.8}$$

where $\mathcal{M}^{f}$ is the matrix element of the full theory inserted by the user, $\mathcal{M}_{\text{eff}}^{f}$ is the matrix element of the effective operator, and $\mathcal{M}_{\text{tot}}^{f}$ is the matrix element of both the full theory and the effective one. Then, the effective coefficients α_i are obtained using Eqs. (3.6) and (3.7).

3.3.1   Derivation of the differential rate

Once we have obtained the effective (relativistic) coefficients α_i, following Eq. (2.34) we can directly write the non-relativistic coefficients c_i in terms of α_i. We are interested on the operators shown in Table 3.1 because these are the dominant terms as they are not suppressed by Q^2. These operators correspond to the relativistic operators $\mathcal{O}_1$, $\mathcal{O}_5$, $\mathcal{O}_8$, $\mathcal{O}_9$ in the fermion DM case and $\mathcal{O}_1$, $\mathcal{O}_3$ in the scalar DM case. Therefore, in the fermion DM case, the expression for the c_1 and c_4 coefficients is:

$$c_1 = 4m_\chi m_e(\alpha_e^{SI} + \alpha_o^{SI}),$$
$$c_4 = 16m_\chi m_e(-\alpha_e^{SD} + 2\alpha_o^{SD}),$$
(3.9)

while for the scalar DM case:

$$c_1 = 2m_e(\alpha_e + 2m_\chi \alpha_o). \tag{3.10}$$

For fermion DM, since c_1 and c_4 are the only non-zero coefficients, the DM response functions reported in Eq. (2.65) simplify to:

$$R_1 = c_1^2 + \frac{3}{16}c_4^2, \tag{3.11}$$

while for scalar DM we have:

$$R_1 = c_1^2. \tag{3.12}$$

Given that the only non-zero DM response function is the first one, the squared ionization amplitude shown in Eq. (2.64) becomes

$$\overline{\left|\mathcal{M}_{\text{ion}}^{n\ell}\right|^2} = R_1 \, W_1^{n\ell}(k', \mathbf{q}). \tag{3.13}$$

Because the DM response function is a constant, it factors out of the integrals in Eq. (2.59), and gives two factorized integrals

$$\frac{\mathrm{d}\mathscr{R}_{\text{ion}}^{n\ell}}{\mathrm{d}\ln E_e} = \frac{n_\chi}{128\pi m_\chi^2 m_e^2} \times R_1 \int \frac{\mathrm{d}^3 v}{v} f_\chi(\mathbf{v})\Theta\left(v - v_{\min}\right) \int \mathrm{d}q \, q \, W_1^{n\ell}(k', \mathbf{q}). \tag{3.14}$$

We already presented the analytic solution for the integral over the DM velocity distribution in Eq. (2.6), while for the second integral the integration is done numerically inside MADDM.

If we include other operators, the DM response function can acquire a dependence on $\mathbf{v}_\perp$, therefore we can not factorize it, and the integral over the DM velocity must be evaluated numerically.

3.3.2 XENON10 and XENON1T experiments

XENON10 and XENON1T are dual-phase liquid xenon detector time projection chambers (TPC) that contain respectively 25 and 2000 kg of pure liquid xenon (LXe) [94, 126]. Both experiments were installed at the Gran Sasso Underground Laboratory (LNGS). XENON10 data covers a period between October 6th 2006 to February 14th 2007, while its successor, XENON1T, took data between October 2016 and February 2018.
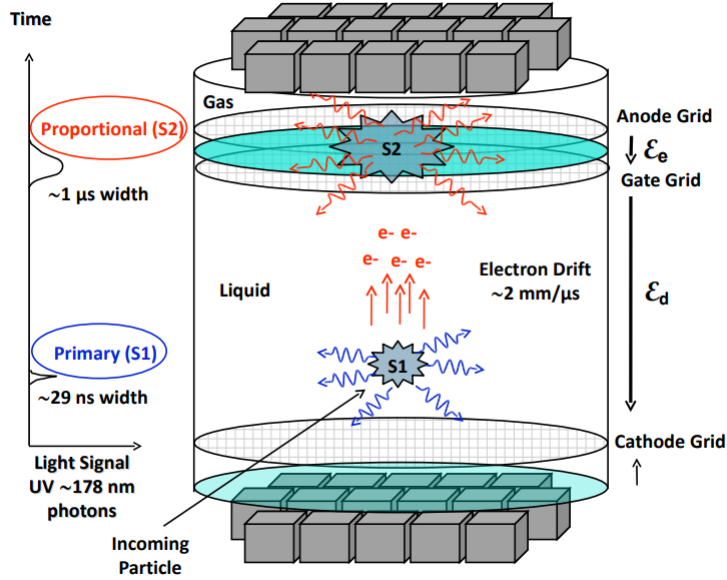The principle of operation of those TPC detectors is shown in Fig. 3.1.

Figure 3.1: Detection of a signal in the XENON10 two-phase TPC. Figure from [126].

The volume of liquid xenon acts both like a target and a scintillator: each interaction ionizes or excites the xenon atoms, and then ionization electrons and primary scintillation photons ($S1$) are produced. The $S1$ photons are produced by the de-excitation of excited Xe molecules (Xe_2^*) to the ground state (Xe_2) and have a wavelength of about 178 nm. The chamber is permeated with an electric field $\epsilon_d \simeq 1$ kV/cm. Under the effect of the electric field, the ionization electrons that escape the recombination with positive ions drift towards the liquid-gas interface with a drift velocity $v_d \simeq 2$ mm/μs. When the electrons reach the gas phase the electric field is stronger ($\epsilon_e \simeq 10$ kV/cm), and the electrons accelerate producing secondary scintillation photons ($S2$). To detect $S1$ and $S2$ signals, photomultiplier tubes (PMTs) are placed in the sensitive regions of the liquid and gas phases.

The number of secondary scintillation photons emitted in the gas is proportional to the number of electrons, which is proportional to the energy deposited in the liquid by the DM particle. One drifting electron produces enough secondary photons to be detected by the PMTs, so a two-phase detector is single-electron sensitive. The difference in the amplitudes of $S1$ and $S2$ signals helps in the discrimination between background (given by beta and gamma-rays) and nuclear recoil signal.

XENON10			XENON1T	
bin [S2]	obs. events		bin [S2]	obs. events
$[14, 41)$	126		$[150, 200)$	8
$[41, 68)$	60		$[200, 250)$	7
$[68, 95)$	12		$[250, 300)$	2
$[95, 122)$	3		$[300, 350)$	1
$[122, 149)$	2		—	—
$[149, 176)$	0		—	—
$[176, 203)$	2		—	—

Table 3.2: Observed signal at XENON10 (left) [91] and XENON1T (right) [94] in the given S2 bins.

3.3.3 From differential rate to S2 signal

Once we have computed the differential rate with Eq. (3.14), we want to translate it into the number of expected events that would be measured in XENON10 and XENON1T. In Table 3.2 we report the binned signal measured in $S2$ by XENON10 and XENON1T experiments, after the background discrimination and the efficiency cuts.

To better see how the rate is modelled into the $S2$ signal, we take, as an example, the differential rate of a benchmark model in which the only non-zero non-relativistic coefficient is c_1; therefore it could be the case of a scalar or vector (or both) mediated DM. The reference DM-e cross-section, in this case, is

$$\bar{\sigma}_e \equiv \frac{\mu_\chi^2 c_1^2}{16\pi m_\chi^2 m_e^2},\tag{3.15}$$

and, for this example, I take $\bar{\sigma}_e = 10^{-38}$ cm^2. Figure 3.2 shows the differential rate produced by the code implemented in this thesis.

Note that only the outer shells of Xe with principal quantum number $n \geq 4$ contribute to the rate. This is because the binding energy of inner shells is higher, and, following Eq. (2.24), for a light-DM particle and for $q > 0$ we get a minimum velocity that is above $v_{\text{esc}} + V_E$, therefore the integral over the DM velocity distribution is zero (see section 2.1). The values for the binding energies are shown in Table 3.3. A heavier DM particle could also ionize the inner shells, but the rate would be too small, given that it is proportional to $1/m_\chi^2$ (see Eq. (3.14)). For this reason, we focus only on light-DM with $m_\chi \leq 1$ GeV. As described in Section 3.3.2, each interaction produces a number n_q of quanta, which can be ionization electrons and/or scintillation photons. We want to compute the number n_e of electrons, which will then drift towards the upper part of the detector and produce the $S2$ signal. To compute n_e we need to use a probabilistic model based on both theoretical and empirical understanding of the electron yield of high-energy electronic recoils [127]. We start with the primary scattered electron, which produces a number N_i of ions and
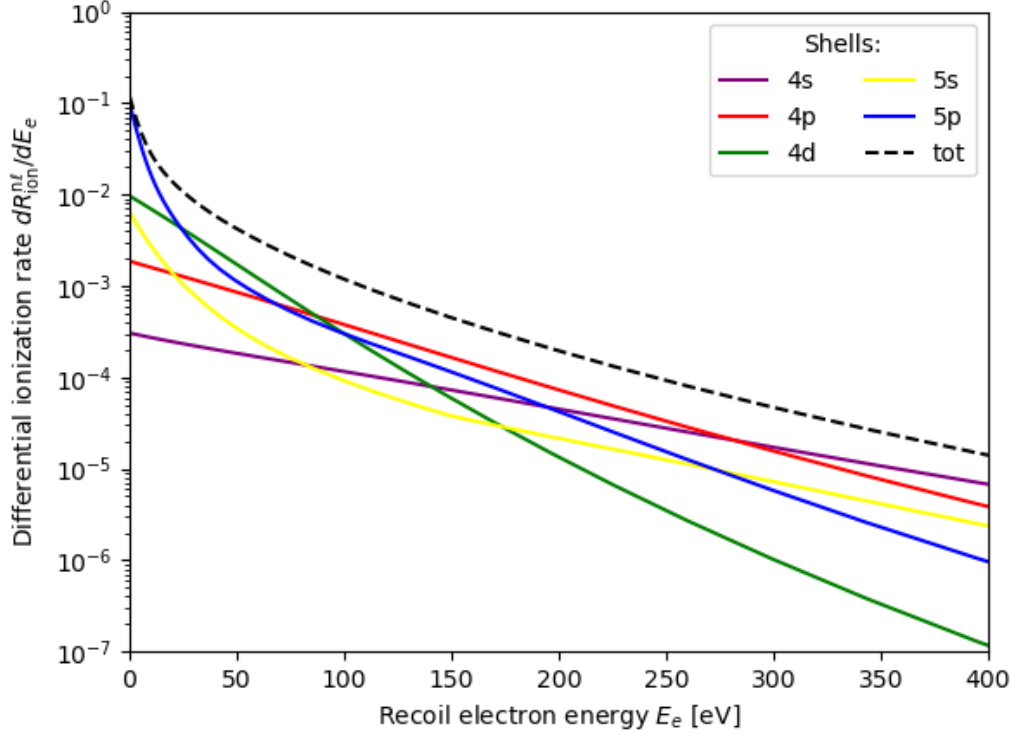
Figure 3.2: Differential ionization rate $d\mathscr{R}_{\rm ion}/dE_e$ for $\bar{\sigma}_e = 10^{-38} cm^2$ and $m_\chi = 1$ GeV. In the plot are shown the different contributions for each shell of xenon atoms and the total rate. Only the outer shells contribute to the rate, because for the inner shells with principal quantum number $n < 4$ the binding energy is bigger, and it would require too high DM velocity to ionize the Xe atom.

a number $N_{\rm ex}$ of excited atoms, whose initial ratio is determined to be $N_{\rm ex}/N_i \approx 0.2$ for a wide range of energies above a keV [128, 129]. Electron-ion recombination follows a modified Thomas-Imel recombination model [130, 131], so the fraction f_R of ions that recombine is basically zero at low energy, therefore $n_e = N_i$ and $n_\gamma = N_{\rm ex}$. Consequently, the fraction f_e of initial quanta observed as electrons is given by [131]

$$f_e = \frac{1 - f_R}{1 + N_{\rm ex}/N_i} \approx 0.83. \tag{3.16}$$

At high energy, the total number n_q of quanta is observed to be $n^{(1)} = \lfloor E_{\rm er}/W \rfloor$ [1], where

---

[1] $\lfloor x \rfloor$ is the floor function that takes as input a real number x and gives as output the greatest integer that is equal or less x.

Shell	$5p^6$	$5s^2$	$4d^{10}$	$4p^6$	$4s^2$
Binding Energy [eV]	12.4	25.7	75.6	163.5	213.8
Photon Energy [eV]	-	13.3	63.2	87.9	201.4
Additional Quanta	0	0	4	$6 - 10$	$3 - 15$

Table 3.3: Binding energies of xenon shells, energy difference from the outer shell $5p^6$ to the inner shell, and additional quanta produced in the de-excitation [133]. Note that the number of additional quanta is not a fixed number, but instead is a range: this takes into account the fact that there could be more than one available lower energy shell for the higher energy shell to de-excite into. In this thesis, I take the minimum of this range.

E_{er} is the energy of the initial scattered electron, and $W = 13.8$ eV is the average energy required to create a single quantum [132]. In addition, if the ionized shell is an inner shell, then an electron from one of the outer shells will de-excite into the ionized shell, emitting a photon that could then photoionize, producing a number $n^{(2)}$ of quanta. The binding energies of xenon shells and the number of quanta produced by the de-excitation are reported in Table 3.3.

Note that the values that are reported for f_R, N_{ex}/N_i and W were measured at energies higher than the ones in which we are interested in, therefore this adds theoretical uncertainty in the predicted rate.

To resume, the number of electrons n_e will be given by $n_e = n'_e + n''_e$, where n'_e represents the primary electron, thus is 0 or 1 with probability f_R or $1 - f_R$ respectively, while n''_e is the number of quanta observed as electrons, which has a mean value of $n_q/n_e = f_e \approx 0.83$, therefore n''_e follows a binomial distribution with success probability f_e and n_q trials. The number n_q of quanta is given by $n^{(1)} + n^{(2)}$, where $n^{(1)} = \lfloor E_{\mathrm{er}}/W \rfloor$ is the number of quanta given by the initial scattered electron, and $n^{(2)}$ is the number of quanta given by the de-excitation into inner shells.

All of these contributions can be condensed in one single function $P^{n\ell}(n_e|E_e)$ that gives the probability for n_e electrons to reach the gas phase of the TPC given an initial ionized electron with energy E_e. Therefore, to convert the rate over energy into the rate over the number of electrons, we need to apply the following equation:

$$\frac{\mathrm{d}\mathscr{R}_{\mathrm{ion}}^{n\ell}}{\mathrm{d}n_e} = \int \mathrm{d}E_e \mathrm{P}^{n\ell}\left(n_e \mid E_e\right) \frac{\mathrm{d}\mathscr{R}_{\mathrm{ion}}^{n\ell}}{\mathrm{d}E_e}. \tag{3.17}$$

In this way, given the rate shown in Fig. 3.2, we obtain the rate shown in Fig. 3.3

We need now to compute the rate over the number of secondary scintillation photons $S2$. As said before, after an event produces n_e electrons inside the TPC, those electrons drift towards the gas phase and then produce a number $S2$ of secondary scintillation photons. The $S2$ signal follows a Gaussian distribution [133–135] with mean $n_e\mu$ and width $\sqrt{n_e}\sigma$, where μ is the secondary-scintillation gain factor and σ is the associated with factor. Those two parameters depend on the experimental setup, and their reported values are
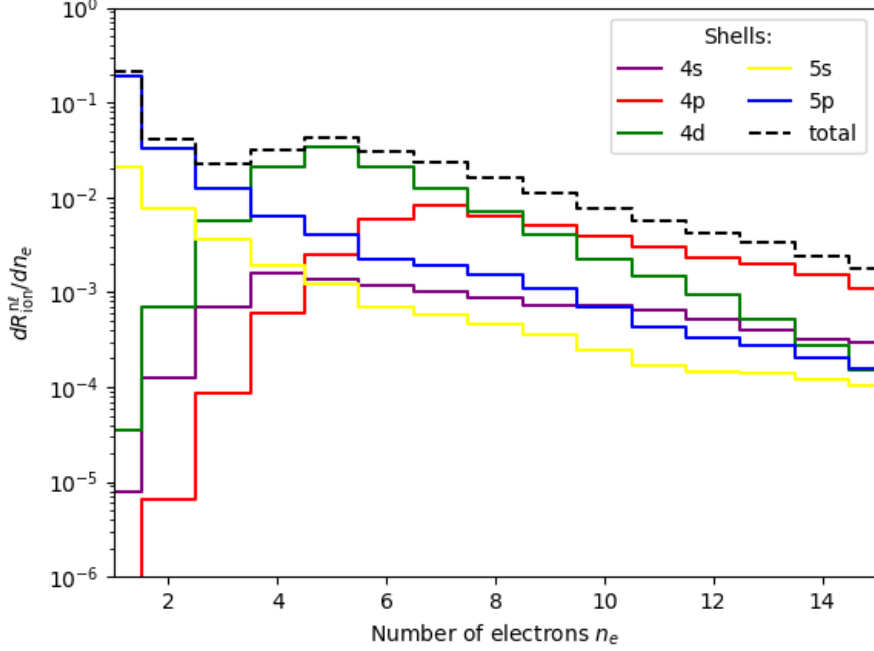
Figure 3.3: Differential rate over the number of produced electrons $\frac{\mathrm{d}\mathscr{R}_{\mathrm{ion}}^{n\ell}}{\mathrm{d}n_e}$ for $\bar{\sigma}_e = 10^{-38}cm^2$ and $m_\chi = 1$ GeV.

$\mu = 27$ (33) and $\sigma = 6.7$ (7) for XENON10 (XENON1T) [76, 94, 133, 136]. Therefore, the rate in terms of $S2$ is given by the following expression

$$\frac{\mathrm{d}\mathscr{R}_{\mathrm{ion}}^{n\ell}}{\mathrm{d}S2} = \varepsilon(S2) \sum_{n_e=1}^{\infty} \mathrm{P}\left(S2 \mid n_e\right) \frac{\mathrm{d}\mathscr{R}_{\mathrm{ion}}^{n\ell}}{\mathrm{d}n_e}, \tag{3.18}$$

where $\mathrm{P}\left(S2 \mid n_e\right)$ is the probability to produce $S2$ photo-electrons given n_e drift electrons, that is equal to

$$\mathrm{P}\left(S2 \mid n_e\right) = \mathrm{Gauss}\left(S2 \mid n_e g_2, \sqrt{n_e}\sigma_{S2}\right), \tag{3.19}$$

and we also multiplied for the efficiency $\varepsilon(S2)$. For XENON10 the efficiency is the product of a flat cut efficiency of 92% multiplied by the trigger efficiency shown in Fig. 1 of [127]. For XENON1T the efficiency is given by the products of all the cuts[2] shown in Fig. 3 of [94] and a flat efficiency of 93%.

Finally, to compute the signal, we need to multiply the rate with the exposure of the two experiments. For XENON10 the exposure is 15 kg days [127], while for XENON1T the exposure $\mathcal{E}$ is given by

---

[2]Note that the "radius" efficiency needs to be squared

$$\mathcal{E} = R^2 \pi \times \Delta z \times \rho_{\mathrm{Xe}} \times \Delta t, \tag{3.20}$$

where $R = 47.9$ cm is the target's radius, $\Delta z = 20$ cm is the height of the search's volume (corresponding to $z \in [-30 \text{ cm}, -10 \text{ cm}]$), $\rho_{\mathrm{Xe}} = 3.1$ g cm^{-3} is the density of liquid xenon, and $\Delta t = 180.7$ days is the time of the search data [94]. This gives an exposure of ~ 80755 kg days. The signal $\mathrm{d}N_{\mathrm{ion}}/\mathrm{d}S2$ for our benchmark example, for both XENON10 and XENON1T, is shown in Fig. 3.4. The straight lines indicate the $S2$ bins used to report the signal. The signal events are given by integrating the signal over each bin. The binned signal is reported in Table 3.4.
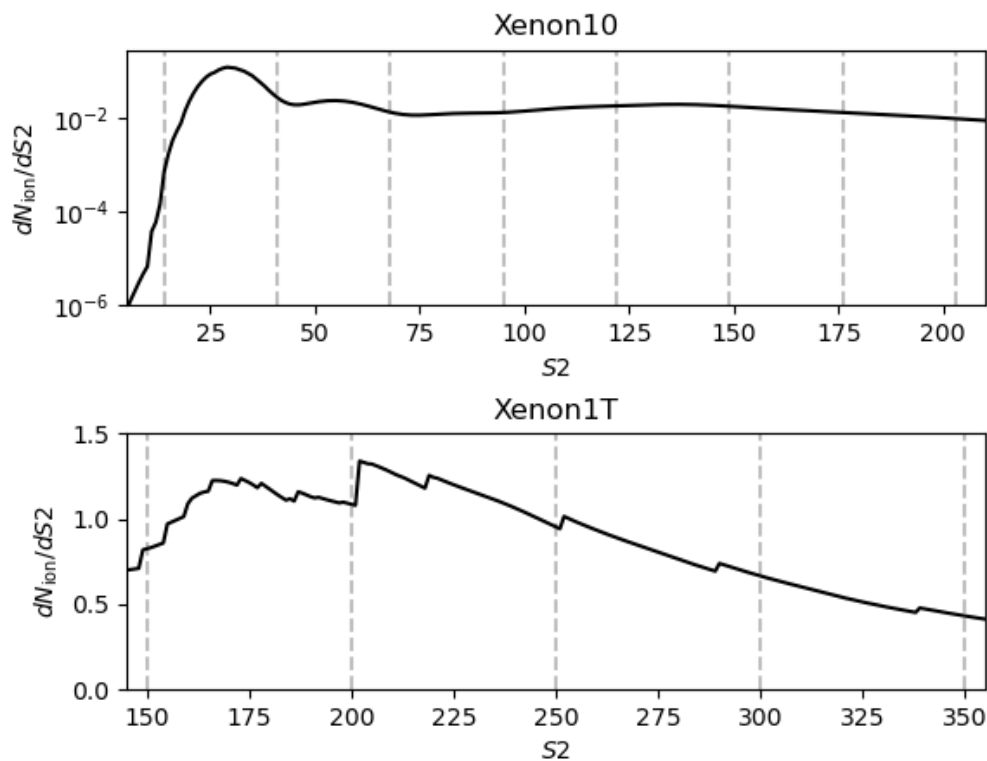

Figure 3.4: Signal over the number of photo-electron for XENON10 (above) and XENON1T (below) for $\bar{\sigma}_e = 10^{-38} cm^2$ and $m_\chi = 1$ GeV. The vertical gray lines indicate the $S2$ values for the bins used to report the signal, as shown in Table 3.2. For XENON1T, only the signal above 150 S2 events has been reported.

We can now compare these results to the measured signal shown in Table 3.2. We can see that, for the benchmark point, in the case of XENON10 the expected signal is smaller than the measured signal, while XENON1T the expected signal is way bigger than the

XENON10		XENON1T	
bin [S2]	obs. events	bin [S2]	obs. events
$[14, 41)$	1.72	$[150, 200)$	55.45
$[41, 68)$	0.58	$[200, 250)$	58.35
$[68, 95)$	0.34	$[250, 300)$	41.01
$[95, 122)$	0.44	$[300, 350)$	26.53
$[122, 149)$	0.53	—	—
$[149, 176)$	0.43	—	—
$[176, 203)$	0.32	—	—

Table 3.4: Predicted signal for XENON10 (left) and XENON1T (right) for a DM particle with mass $m_\chi = 1$ GeV and a reference cross section $\bar{\sigma}_e = 10^{-38}$ cm^2.

measured one. The case in which the expected signal is smaller than the measured one can be due to unknown background, so the expected signal is compatible with the data. In the case in which the expected signal is larger than the experimental signal, we can say instead that the model taken into account is not compatible with the data, so we discard it.

Here we made only qualitative assumptions, the next section shows how to use the results on Table 3.4 to get a quantitative understanding of the agreement of our model with experimental data, and also how to produce exclusion limits on the parameters of a given model.

3.4 Derivation of exclusion limits from XENON10 and XENON1T data

In this section, we describe how to obtain the level of agreement of our model to the experimental data, that is described by the p-value, and present the exclusion limits on the non-relativistic coefficients c_1 and c_4 studied in this thesis.

3.4.1 Evaluation of the p-value

The p-value p is a statistical measure used to determine the probability of observing the outcome of an experiment as extreme as the measured one, assuming that the null hypothesis is true. A p-value smaller than the significance level (usually set to 0.05 or 0.01) indicates that the observed difference is statistically significant, and the null hypothesis is rejected. In our case, we want to see if our model is excluded or not, so we take the null hypothesis to be our DM model, that produces the expected signal μ shown in Table 3.4, where μ is the sum of the signal in each bin. The p-value is then given

by the probability to measure a signal s' as extreme as the measured signal s shown in Table 3.2, where s is the sum of the measured signal in each bin[3].

With "as extreme as", we mean that, if $s \leq \mu$, the "more extreme" measures are the ones lower than s, therefore the p-value p is given by the sum of the probabilities to measure a signal s' lower or equal than the measured one s, that means:

$$p = P_0(\mu) + P_1(\mu) + P_2(\mu) + \cdots + P_s(\mu) = \sum_{i=0}^{s} P_i(\mu), \qquad (3.21)$$

where $P_i(\mu)$ stands for the probability to measure $s' = i$ given an expected value μ. If instead $s \geq \mu$, we take the sum of probabilities to measure a signal s' bigger or equal than the measured one s:

$$p = P_s(\mu) + P_{s+1}(\mu) + P_{s+2}(\mu) + \cdots + P_\infty(\mu) = \sum_{i=s}^{\infty} P_i(\mu). \qquad (3.22)$$

But as said in the previous section, we are not interested in the case in which $s \geq \mu$, because we are only interested into excluding DM models that give us a signal bigger than the measured one. Therefore, in this thesis, we will only consider Eq. (3.21), therefore obtaining a one-sided upper bound on the parameters of the DM model.

To get a robust upper bound, we can treat each bin independently and compute the p-value for each one of them. To compute the p-value $p^{(j)}$ associated to the j-th bin, we assume that the signal follows a Poisson distribution with mean $\mu^{(j)}$ equal to the expected DM signal on the j-th bin. Therefore, the probability $P_i(\mu^{(j)})$ to measure a signal equal to i, given an expected value $\mu^{(j)}$, is equal to the Poisson density function

$$P_i(\mu) = f_{\text{Poiss}}(i; \mu) = \frac{e^{-\mu}\mu^i}{i!}, \qquad (3.23)$$

and the p-value for the j-th bin is given by

$$p^{(j)} = P_0(\mu^{(j)}) + P_1(\mu^{(j)}) + P_2(\mu^{(j)}) + \cdots + P_{s^{(j)}}(\mu^{(j)}) = F_{\text{Poiss}}(s^{(j)}; \mu^{(j)}), \qquad (3.24)$$

where F_{Poiss} is the Poisson cumulative density function

$$F_{\text{Poiss}}(n; \mu) = \sum_{i=0}^{n} \frac{e^{-\mu}\mu^i}{i!}. \qquad (3.25)$$

We assume a Poisson distribution because it is commonly used to model the distribution of counts or frequencies of rare events, where each event is independent of the others and occurs at a fixed average rate. Therefore, the Poisson distribution is a natural choice for

---

[3]We consider the case in which the signal measured by the XENON collaboration is entirely given by DM scattering, therefore the background is assumed to be zero.

modelling the distribution of entries in a histogram, particularly when the bin contents are low and the probability of observing multiple counts in a single bin is small.

Once we have computed the p-values $p^{(j)}$ for each bin, we take the final p-value to be equal to the lowest one. This is due to the fact that some bins have reported way fewer events than others, therefore they are more sensitive than others to detect possible DM candidates, so we consider only the p-value associated to the most sensitive bin.

If we apply this procedure using as signal s the data reported in Table 3.2 and as expected signal μ the data reported in Table 3.4, we obtain a minimum p-value equal to 0.65 for XENON10 and 2.36×10^{-17} for XENON1T. Therefore, using a significance level equal to 0.01, we can say that for XENON10 the expected signal is compatible with the measured one, while this is not true for XENON1T, so we reject the model point.

MADDM has the capability to make scans on the parameter space of the DM model inserted by the user. In this way, it is possible to obtain the p-value for any region of the parameter space. By plotting all the points with p-value above a certain quantity α, it is possible to get the exclusion limits with confidence level $C.L. = 1 - \alpha$.

Chapter 4

Analysis of DM models

In this chapter, we first study different simplified models for a Dirac DM particle that interacts with a SM particle through a scalar, vector or pseudo-scalar mediator. We then study the case of scalar dark QED model of DM, in which the scalar DM particle φ couples to a massive "dark photon" that mixes kinetically with the SM photon. In this last case, we compute as well the model parameter space that leads to the measured relic density and confront it with the upper bounds from XENON10 and XENON1T.

Those models were implemented in UFO format using FEYNRULES, and then loaded into MADDM to validate the analytic result of the scattering amplitudes. We also use them to verify the correct projection into the effective operators of Table 3.1.

We show how the non-relativistic coefficients c_1 and c_4 are linked to the Lagrangian parameters, and we present the exclusion limits of c_1 and c_4 computed with MADDM.

4.1 Scattering amplitude of simplified Dirac DM-e models

4.1.1 Vector mediated DM

The Lagrangian for vector mediated DM is:

$$
\begin{aligned}
\mathcal{L} &= \mathcal{L}_{kin} + \mathcal{L}_{int} + \mathcal{L}_{mass} + \mathcal{L}_{SM} \\
&= -\frac{1}{4} F^{\mu\nu} F_{\mu\nu} + (g_e^V \bar{e}\gamma^\mu e + g_\chi^V \bar{\chi}\gamma^\mu \chi)V_\mu + \frac{M_V^2}{2} V^\mu V_\mu - m_\chi \bar{\chi}\chi + \mathcal{L}_{SM},
\end{aligned}
\tag{4.1}
$$

where χ is the Dirac DM particle with mass m_χ, V_μ is the vector mediator with mass M_V and $F^{\mu\nu} = \partial^\mu V^\nu - \partial^\nu V^\mu$ is the field strength for V^μ. The matrix element of DM-e interaction is:
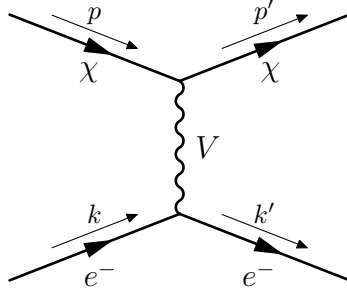
Figure 4.1: Vector mediated scattering between DM and electrons

$$i\mathcal{M} = (-ig_\chi^V)\bar{u}_3\gamma^\mu u_1 \frac{-ig_{\mu\nu}}{t - M_V^2}(-ig_e^V)\bar{u}_4\gamma^\nu u_2. \tag{4.2}$$

We compute the unpolarized squared amplitude, averaging on the polarizations of the initial particles:

$$|\bar{A}|^2 = \frac{1}{4}\sum_{spin}|\mathcal{M}|^2 = \frac{1}{4}g_\chi^{V\,2}g_e^{V\,2}\frac{1}{(t - M_V^2)^2}\sum_{spin}\bar{u}_3\gamma^\mu u_1\bar{u}_4\gamma_\mu u_2\bar{u}_1\gamma^\nu u_3\bar{u}_2\gamma_\nu u_4. \tag{4.3}$$

Rearranging the spinor products in order to get a trace and using the fermion completeness relations, we obtain:

$$\begin{aligned}
|\bar{A}|^2 = \frac{1}{4}g_\chi^{V\,2}g_e^{V\,2}\frac{1}{(t - M_V^2)^2}\,\mathrm{Tr}\left[(\not{p} + m_\chi)\gamma^\nu(\not{p}' + m_\chi)\gamma^\mu\right] \\
\cdot\,\mathrm{Tr}\left[(\not{k} + m_e)\gamma_\nu(\not{k}' + m_e)\gamma_\mu\right].
\end{aligned} \tag{4.4}$$

We compute the trace of the gamma matrices, and we rewrite the amplitude squared in terms of the 4-momenta of the particles:

$$\begin{aligned}
|\bar{A}|^2 = 8g_\chi^{V\,2}g_e^{V\,2}\frac{1}{(t - M_V^2)^2}\Big[(p \cdot k')(p' \cdot k) + (p \cdot k)(p' \cdot k') \\
- m_e^{\,2}p \cdot p' - m_\chi^{\,2}k \cdot k' + 2m_e^{\,2}m_\chi^{\,2}\Big].
\end{aligned} \tag{4.5}$$

We analyse the case in which the incoming DM has an initial energy E_χ and it scatters with an electron loosely bound to a nucleus, so we can assume it to be at rest. After the scattering, the electron acquires a recoil energy E_R. So we can write the 4-momenta of the particles as:

$$p = (E_\chi, \mathbf{p}_\chi), \qquad k = (m_e, \mathbf{0}), \qquad p' = (E_\chi', \mathbf{p}'), \qquad k' = (E_R, \mathbf{p}_e). \tag{4.6}$$

Substituting those 4-momenta inside Eq. (4.5) we obtain the following result:

$$|\bar{A}|^2 = g_\chi^{V2} g_e^{V2} \frac{1}{(t-M_V^2)^2} 8 \Big\{ m_e \big[m_e(2E_\chi^2 - 2E_\chi E_R + E_R^2)$$
$$- (3m_e^2 + m_\chi^2)E_R \big] + 2m_e^3 E_\chi + 2m_e^4 + m_\chi^2 m_e^2 \Big\}. \tag{4.7}$$

The value of the amplitude squared was validated using MADDM. In the low energy limit, the interaction Lagrangian can be written as an effective field theory

$$(\mathcal{L}_{int})_{M_V^2 \gg t} = G_V \bar{e} \gamma^\mu e \bar{\chi} \gamma^\mu \chi, \tag{4.8}$$

where $G_V = g_e^V g_\chi^V / M_V^2$. Given that the effective Lagrangian of Eq. (4.8) is proportional to the SI odd operator shown in Table 3.1, the projection of this Lagrangian is non-zero only for this operator, and the only non-zero relativistic coefficient is

$$\alpha_o^{SI} = G_V = \frac{g_e^V g_\chi^V}{M_V^2}. \tag{4.9}$$

This expression has been validated analytically and numerically with MADDM.

4.1.2 Scalar mediated DM

The Lagrangian for scalar-mediated DM is:

$$\mathcal{L} = \mathcal{L}_{kin} + \mathcal{L}_{int} + \mathcal{L}_{mass} + \mathcal{L}_{SM}$$
$$= (\partial^\mu \phi)^*(\partial_\mu \phi) + (g_e^\phi \bar{e}e + g_\chi^\phi \bar{\chi}\chi)\phi - M_\phi^2 \phi^* \phi - m_\chi \bar{\chi}\chi + \mathcal{L}_{SM}, \tag{4.10}$$

where χ is the Dirac DM particle with mass m_χ and ϕ is the scalar mediator with mass M_ϕ. The matrix element of DM-e interaction is:
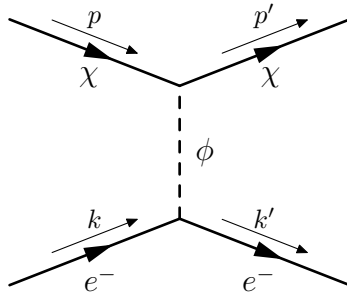

Figure 4.2: Scalar mediated scattering between DM and electrons

$$i\mathcal{M} = (-ig_\chi^\phi)\bar{u}_3 u_1 \frac{i}{t - M_\phi^2} (-ig_e^\phi)\bar{u}_4 u_2. \tag{4.11}$$

We compute the unpolarized squared amplitude:

$$|\bar{A}|^2 = \frac{1}{4}\sum_{spin}|\mathcal{M}|^2 = \frac{1}{4}g_\chi^{\phi 2}g_e^{\phi 2}\frac{1}{(t-M_\phi^2)^2}\sum_{spin}\bar{u}_3 u_1 \bar{u}_4 u_2 \bar{u}_1 u_3 \bar{u}_2 u_4$$
$$= \frac{1}{4}g_\chi^{\phi 2}g_e^{\phi 2}\frac{1}{(t-M_\phi^2)^2}\text{Tr}\left[(\not{p}+m_\chi)(\not{p}'+m_\chi)\right]\text{Tr}\left[(\not{k}+m_e)(\not{k}'+m_e)\right] \qquad (4.12)$$
$$= 4g_\chi^{\phi 2}g_e^{\phi 2}\frac{1}{(t-M_\phi^2)^2}(p\cdot p'+m_\chi^2)(k\cdot k'+m_e^2).$$

Using the 4-momenta of Eq. (4.6), we obtain the following result:

$$|\bar{A}|^2 = g_\chi^{\phi 2}g_e^{\phi 2}\frac{1}{(t-M_\phi^2)^2}4m_e(2m_\chi^2-m_e^2+m_e E_R)(E_R+m_e). \qquad (4.13)$$

The value of the amplitude squared was validated using MADDM. In the low energy limit, the interaction Lagrangian can be written as an effective field theory

$$(\mathcal{L}_{int})_{M_\phi^2 \gg t} = G_S \bar{e}e\bar{\chi}\chi, \qquad (4.14)$$

where $G_S = g_e^\phi g_\chi^\phi/M_\phi^2$. Given that the effective Lagrangian of Eq. (4.14) is proportional to the SI even operator shown in Table 3.1, the projection of this Lagrangian is non-zero only for this operator, and the only non-zero relativistic coefficient is

$$\alpha_e^{SI} = G_S = \frac{g_e^\phi g_\chi^\phi}{M_\phi^2}. \qquad (4.15)$$

This expression has been validated analytically and numerically with MADDM.

4.1.3 Pseudo-scalar mediated DM

The Lagrangian for pseudo-scalar mediated DM is:

$$\mathcal{L} = \mathcal{L}_{kin} + \mathcal{L}_{int} + \mathcal{L}_{mass} + \mathcal{L}_{SM}$$
$$= (\partial^\mu a)^*(\partial_\mu a) + (g_e^a \bar{e}\gamma^5 e + g_\chi^a \bar{\chi}\gamma^5 \chi)a - M_a^2 a^* a - m_\chi \bar{\chi}\chi + \mathcal{L}_{SM}, \qquad (4.16)$$

where χ is the Dirac DM with mass m_χ and a is the pseudo-scalar propagator with mass M_a. The matrix element of DM-e interaction is:
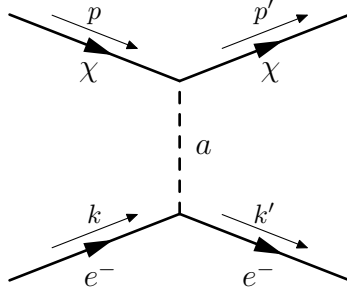
Figure 4.3: Pseudo-scalar mediated scattering between DM and electrons

$$i\mathcal{M} = (-ig_\chi^a)\bar{u}_3\gamma^5 u_1 \frac{i}{t - M_a^2}(-ig_e^a)\bar{u}_4\gamma^5 u_2. \tag{4.17}$$

We compute the unpolarized squared amplitude:

$$
\begin{aligned}
|\bar{A}|^2 &= \frac{1}{4}\sum_{spin}|\mathcal{M}|^2 = \frac{1}{4}g_\chi^{a\,2}g_e^{a\,2}\frac{1}{(t - M_a^2)^2}\sum_{spin}\bar{u}_3\gamma^5 u_1\bar{u}_4\gamma^5 u_2\bar{u}_1\gamma^5 u_3\bar{u}_2\gamma^5 u_4 \\
&= \frac{1}{4}g_\chi^{a\,2}g_e^{a\,2}\frac{1}{(t - M_a^2)^2}\,\mathrm{Tr}\left[(\not{p} + m_\chi)\gamma^5(\not{p}' + m_\chi)\gamma^5\right]\mathrm{Tr}\left[(\not{k} + m_e)\gamma^5(\not{k}' + m_e)\gamma^5\right] \\
&= 4g_\chi^{a\,2}g_e^{a\,2}\frac{1}{(t - M_a^2)^2}(m_\chi^2 - p\cdot p')(m_e^2 - k\cdot k').
\end{aligned}
\tag{4.18}
$$

Using the 4-momenta of Eq. (4.6), we obtain the following result:

$$|\bar{A}|^2 = g_\chi^{a\,2}g_e^{a\,2}\frac{1}{(t - M_a^2)^2}4(m_e^2 - m_e E_R)^2. \tag{4.19}$$

The value of the amplitude squared was validated using MADDM. In the low energy limit, the interaction Lagrangian can be written as an effective field theory

$$(\mathcal{L}_{int})_{M_a^2 \gg t} = G_{PS}\bar{e}\gamma^5 e\bar{\chi}\gamma^5\chi, \tag{4.20}$$

where $G_{PS} = g_e^a g_\chi^a / M_a^2$. The effective Lagrangian of Eq. (4.8) does not correspond to any operator shown in Table 3.1, so the projection of this Lagrangian is zero for each one of them. This is due to the fact that the scattering amplitude in Eq. (4.19), at low energy, is proportional to Q^4.

$$
\begin{aligned}
|\bar{A}|^2 &\propto \left(m_e^2 - m_e E_R\right)^2 = \left(m_e^2 - m_e\sqrt{m_e^2 + p_e^2}\right)^2 = m_e^4\left(1 - \sqrt{1 + \frac{p_e^2}{m_e^2}}\right)^2 \\
&\xrightarrow{\mathbf{p}_e \to 0} m_e^4\left(1 - 1 - \frac{p_e^2}{2m_e^2}\right)^2 = \frac{1}{4}p_e^4 = \frac{1}{4}Q^4,
\end{aligned}
\tag{4.21}
$$

63

where the last equivalence is justified by the fact that the final electron momentum p_e is equal to the exchanged momentum, given that the electron is initially assumed at rest. Because the amplitude is proportional to Q^4, the interference with the operators of Table 3.1, which are independent on Q, is always zero in the low energy limit. This was also verified numerically with MADDM.

We can repeat the same procedure for axial and tensorial mediated Dirac DM, and we verified both analytically and numerically that the only non-zero relativistic coefficient in these cases are respectively

$$\alpha_e^{SD} = \frac{g_\chi^{\mathrm{ax}} g_e^{\mathrm{ax}}}{M_{\mathrm{ax}}^2}, \qquad \alpha_o^{SD} = \frac{g_\chi^{\mathrm{t}} g_e^{\mathrm{t}}}{M_{\mathrm{t}}^2}. \tag{4.22}$$

4.2 Exclusion limits on non-relativistic coefficients

Thanks to Eq. (3.9) and Eq. (3.10) we can write the non-relativistic coefficients c_1 and c_4 in terms of the relativistic ones, that we can link to the Lagrangian parameters as seen in the previous chapter. For fermion DM we obtain:

$$c_1 = 4m_\chi m_e \left(\frac{g_\chi^\phi g_e^\phi}{M_\phi^2} + \frac{g_\chi^V g_e^V}{M_V^2} \right),$$

$$c_4 = 16 m_\chi m_e \left(-\frac{g_\chi^{\mathrm{ax}} g_e^{\mathrm{ax}}}{M_{\mathrm{ax}}^2} + 2\frac{g_\chi^{\mathrm{t}} g_e^{\mathrm{t}}}{M_{\mathrm{t}}^2} \right), \tag{4.23}$$

while for a scalar DM particle φ, we obtain:

$$c_1 = 2m_e \left(\frac{g_\varphi^\phi g_e^\phi}{M_\phi^2} + 2m_\chi \frac{g_\varphi^V g_e^V}{M_V^2} \right). \tag{4.24}$$

Using MADDM we can make scans on the Lagrangian parameters, and then make exclusion limits on c_1 and c_4. In Fig. 4.4 we show the exclusion limits at $C.L. = 95\%$ for the individual couplings c_1 and c_4 for a DM mass $m_\chi \in [1, 1000]$ MeV.

In this case, the exclusion limits between c_1 and c_4 are quite similar because, as shown in section 3.3.1, they appear both in the DM response function just as constants multiplied by a number. If we consider only c_1 the DM response function is simply $R_1^{n\ell}\left(\mathbf{v}^\perp, \frac{\mathbf{q}}{m_e}\right) = c_1^2$, while if we consider only c_4 we get $R_1^{n\ell}\left(\mathbf{v}^\perp, \frac{\mathbf{q}}{m_e}\right) = \frac{3}{16}c_4^2$.

In the case in which we consider the other suppressed operators, the DM response function becomes more complex and acquires a dependence on $\mathbf{v}_{\mathrm{el}}^\perp$ and/or $\mathbf{q}$, therefore the exclusion limits will have a different shape.
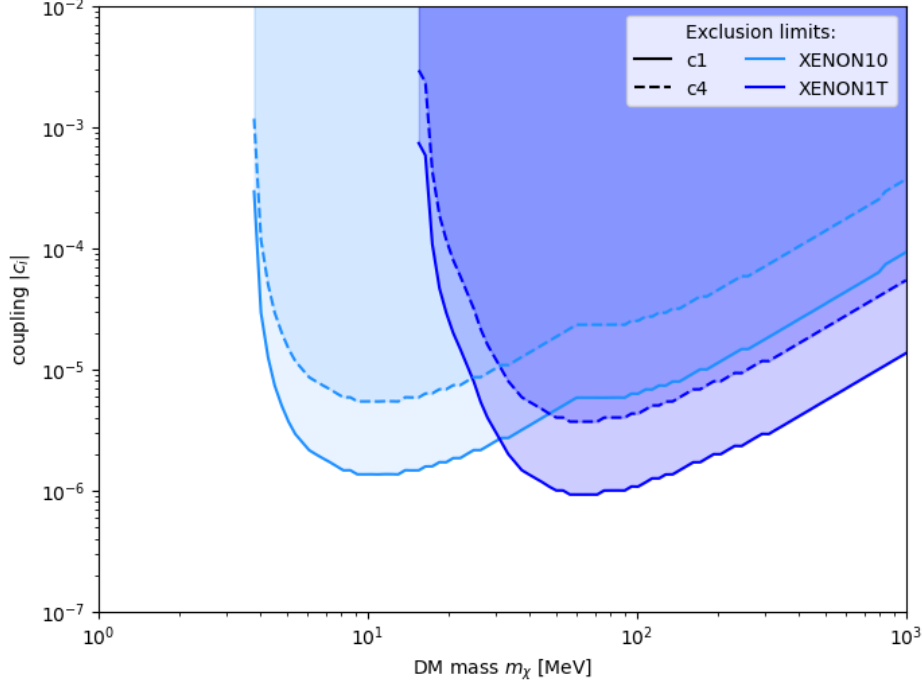
Figure 4.4: Exclusion limits at 95% C.L. on the non-relativistic coefficients c_1 (continuous line) and c_4 (dashed line) for $m_\chi \in [1, 1000]$ MeV. The exclusion limits are computed using XENON10 and XENON1T data, which exclude respectively the light blue and blue regions of the plot.

4.3 Scalar dark QED model

We start by introducing the most generic Lagrangian of two Abelian gauge bosons A_a and A_b, described by two gauge groups $U(1)_a$ and $U(1)_b$, that couples respectively to the DM particle and to SM fermions with coupling g_D and e, where $g_D \equiv \sqrt{4\pi\alpha_D}$ is a new "dark" coupling and e is the QED coupling [137]. The two gauge bosons are kinematically mixed, and the mixing is controlled by a parameter ϵ. This Lagrangian, considering only the kinetic and interaction terms, is:

$$\mathcal{L} = \mathcal{L}_{\text{kin}} + \mathcal{L}_{\text{int}} = -\frac{1}{4}F_{a\mu\nu}F_{a\mu\nu} - \frac{1}{4}F_b{}^{\mu\nu}F_{b\mu\nu} - \frac{\epsilon}{2}F_b{}^{\mu\nu}F_{a\mu\nu} + e\mathcal{J}_\mu A_b{}^\mu + g_D\mathcal{J}_{D\mu}A_a{}^\mu, \quad (4.25)$$

where F_a and F_b are respectively the A_a and A_b field strengths:

$$F_a{}^{\mu\nu} = \partial^\mu A_a{}^\nu - \partial^\nu A_a{}^\mu,$$
$$F_b{}^{\mu\nu} = \partial^\mu A_b{}^\nu - \partial^\nu A_b{}^\mu. \tag{4.26}$$

while $\mathcal{J}_\mu$, $\mathcal{J}_{D\mu}$ are the SM and DM currents:

$$\mathcal{J}_\mu = \sum_f \bar{\psi}_f \gamma^\mu \psi_f,$$
$$\mathcal{J}_D^\mu = i\varphi^* \partial^\mu \varphi + c.c. \ . \tag{4.27}$$

We diagonalize the kinetic terms in Eq. (4.25) by redefining the two gauge fields A_a and A_b:

$$\begin{pmatrix} A_a^\mu \\ A_b^\mu \end{pmatrix} = \begin{pmatrix} \frac{1}{\sqrt{1-\varepsilon^2}} & 0 \\ -\frac{\varepsilon}{\sqrt{1-\varepsilon^2}} & 1 \end{pmatrix} \begin{pmatrix} A'^\mu \\ A^\mu \end{pmatrix}, \tag{4.28}$$

where we identify A_μ with the SM photon and A'^μ with the dark photon. In this new basis, the interaction Lagrangian becomes:

$$\mathcal{L}_{\text{int}} = \left[\frac{g_D}{\sqrt{1-\varepsilon^2}} \mathcal{J}'_\mu - \frac{e\varepsilon}{\sqrt{1-\varepsilon^2}} \mathcal{J}_\mu \right] A'^\mu + e\mathcal{J}_\mu A^\mu. \tag{4.29}$$

Thanks to the kinematic mixing, the SM current couples to the dark photon with a coupling $e\varepsilon/\sqrt{1-\varepsilon^2}$, therefore DM particles can interact with SM fermions by exchanging a dark photon. Because experimentally we have not measured this mixing, we assume ϵ to be small, therefore the coupling between the SM particles and the dark photon can be approximated to εe. Using the same approximation also for the coupling between the DM particle and the dark photon, we can rewrite the interaction Lagrangian as:

$$\mathcal{L}_{\text{int}} = \left(g_D \mathcal{J}'_\mu - e\varepsilon \mathcal{J}_\mu \right) A'^\mu + e\mathcal{J}_\mu A^\mu. \tag{4.30}$$

We constrain the parameters of this DM model using the relic abundance of DM and direct detection analysis.

4.3.1 Evaluating the relic density

In general, DM particles freeze out around $x \sim 20$, and the $\langle \sigma v \rangle$ value that provides the correct relic abundance is $\langle \sigma v \rangle \sim 1 \times 10^{-26}$ cm^3 s^{-1}, therefore, the parameters of our model must satisfy this condition.
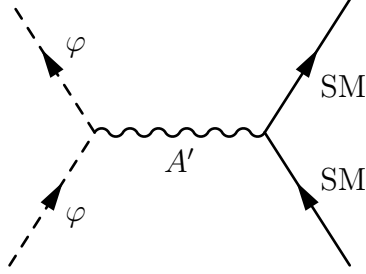
Figure 4.5: DM annihilation into two SM particles mediated by a dark photon A'.

For light-DM ($m_\varphi < 1$ GeV), freeze-out happens at a temperature $T \sim m_\varphi/20 < 0.1$ GeV, that is lower than the temperature of QCD phase transition [138], so we can no more describe the relevant SM particles as free quarks, but as hadrons. For this reason, to compute the annihilation cross section we should use chiral perturbation theory, but in the case of this dark QED model, we can avoid that, since this model has the same structure as QED. To compute the cross section for $\varphi^*\varphi \to$ hadrons, we can use the R-ratio, defined as

$$R_{\text{had}}^\gamma(\sqrt{s}) \equiv \frac{\sigma\left(e^+e^- \to \text{ hadrons }\right)}{\sigma\left(e^+e^- \to \mu^+\mu^-\right)}. \tag{4.31}$$

This ratio is determined experimentally and tabulated in Ref. [139]. We can use it to determine the dark matter annihilation cross section to hadrons

$$\sigma(\varphi^*\varphi \to \text{ hadrons }) = \sigma\left(\varphi^*\varphi \to \mu^+\mu^-\right) R(\sqrt{s}). \tag{4.32}$$

The annihilation cross section into two SM particles is therefore given by

$$\begin{aligned}
\sigma\left(\varphi^*\varphi \to \overline{\text{SM}}\,\text{SM}\right) &= \sum_{\ell=e,\mu,\tau} \sigma\left(\varphi^*\varphi \to \ell^+\ell^-\right) + \sigma\left(\varphi^*\varphi \to \text{ hadrons}\right) \\
&= \sum_{\ell=e,\mu,\tau} \sigma\left(\varphi^*\varphi \to \ell^+\ell^-\right) + \sigma\left(\varphi^*\varphi \to \mu^+\mu^-\right) R(\sqrt{s}),
\end{aligned} \tag{4.33}$$

where the annihilation cross section of DM into two fermions f can be computed analytically [140], and is equal to

$$\sigma = \frac{n_c g_D^2 s}{12\pi\left[(m_{A'}^2 - s)^2 + \Gamma_{A'}^2 m_{A'}^2\right]} \sqrt{1 - \frac{4m_\varphi^2}{s}} \sqrt{1 - \frac{4m_f^2}{s}} \left[(\epsilon e)^2 \left(1 + \frac{2m_f^2}{s}\right)\right], \tag{4.34}$$

where n_c is the number of colours, therefore $n_c = 1$ for leptons, and the dark photon width is given by

$$\Gamma_{A'} \equiv \sum_f \Gamma(A' \to f\bar{f}) = \sum_f \frac{n_c m_{A'}}{12\pi S} \sqrt{1 - \frac{4m_f^2}{m_{A'}^2}} \left[(\epsilon e)^2 \left(1 + 2\frac{m_f^2}{m_{A'}^2} \right) \right], \qquad (4.35)$$

where $S \equiv 1(2)$ for (in)distinguishable final states particles. We can now compute the thermally averaged cross section $\langle \sigma v \rangle$ shown in Eq. (1.20) using the annihilation cross section in Eq. (4.33) for a range of DM masses m_φ, mediator masses $m_{A'}$, coupling g_D and mixing parameter ϵ. We select all the combinations of parameters that satisfy the condition $\langle \sigma v \rangle = 1 \times 10^{-26}$ cm^3 s^{-1} and we use those parameters to compute the reference cross section σ_e for DM annihilation into e^+e^-:

$$\bar{\sigma}_e = \frac{\mu_{\varphi,e}^2}{\pi m_{A'}^4} (\epsilon e g_D)^2, \qquad (4.36)$$

where $\mu_{\varphi,e}$ is the DM-e reduced mass. The dashed line in Fig. 4.7 shows the reference cross sections σ_e that satisfies the condition $\langle \sigma v \rangle = 1 \times 10^{-26}$ cm^3 s^{-1}. This cross section is equal to the one for DM-e scattering, thanks to the crossing symmetry propriety of the scattering amplitude, so we can confront it to the one computed in direct detection analysis.

In the region above the dashed line, the resulting DM relic abundance would be lower than the measured one, but a hidden-sector/multi-component DM scenario, could still complete the DM abundance, see for example Ref. [141]. In this scenario, the DM particle that couples to SM fermions is a sub-dominant component of the DM particle content, therefore the relic abundance associate to this particle can be lower than the measured one.

Below the dashed line, the abundance is larger than the measured one, thus leading to overclosure of the Universe, so we exclude this region.

4.3.2 Exclusion limits from direct detection

Using MADDM is it possible to make scans on the parameters m_φ, $m_{A'}$, g_D and ϵ of this theory, obtaining the p-value p for each combination. We can select the combinations of coefficients that satisfy the condition $p > 1 - C.L.$, and then use those parameters to compute the reference DM-e cross section shown in Eq. (4.36), similarly as we have done in the previous section.
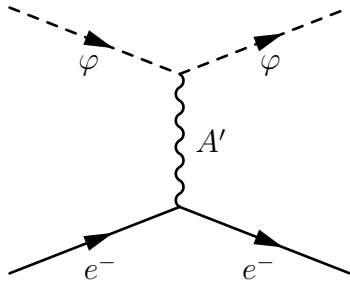
Figure 4.6: DM-e scattering mediated via a dark photon A'.

To compute the exclusion limits, we could also use the ones that we already made on c_1, shown in Fig. 4.4. In fact, in the case of a scalar dark QED model, the full theory at low energy can be described by the odd SI relativistic operator of Table (2.30), and the only non-zero non-relativistic coefficient is c_1. In this case, the cross section σ_e, is defined as:

$$\bar{\sigma}_e \equiv \frac{\mu_{\varphi,e}^2 c_1^2}{16\pi m_\varphi^2 m_e^2}, \tag{4.37}$$

Notice that, using Eq. (3.10) and using a similar procedure to the one shown in section 4.1.1, we can compute analytically c_1, obtaining

$$c_1 = 4m_\chi m_e \alpha_o^{SI} = 4m_\chi m_e \frac{\epsilon e g_D}{m_{A'}^2}. \tag{4.38}$$

By substituting c_1 to Eq. (4.37), we obtain Eq. (4.36), so the two procedures are indeed equivalent.

The exclusion limits considering $m_\varphi \in [1, 1000]$ MeV are shown in Fig. 4.7.

Other constraints for the parameters of this model arise from different types of analysis, as collider experiments like BaBar, in which the process $e^+ e^- \to \gamma +$ *invisible* is studied [142–144], or electroweak precision tests (EWPT) [145, 146]. Constraints for g_D come from DM self interaction, that requires $\sigma_{\text{self-int}} \lesssim 1$ cm^2/g for clusters [147], or from perturbative consistency [148], while constraints for ϵ, g_D and $m_{A'}$ come from beam-dump analysis [149].

Future direct detection experiments, like LZ [75], XENONnT [76], DARWIN [77]) or DarkSide20k [78], with their improved sensitivity and lower background levels, could probe the region that describes the correct DM relic abundance, therefore leading to a potential discovery or excluding this model for a certain range of DM mass m_φ.
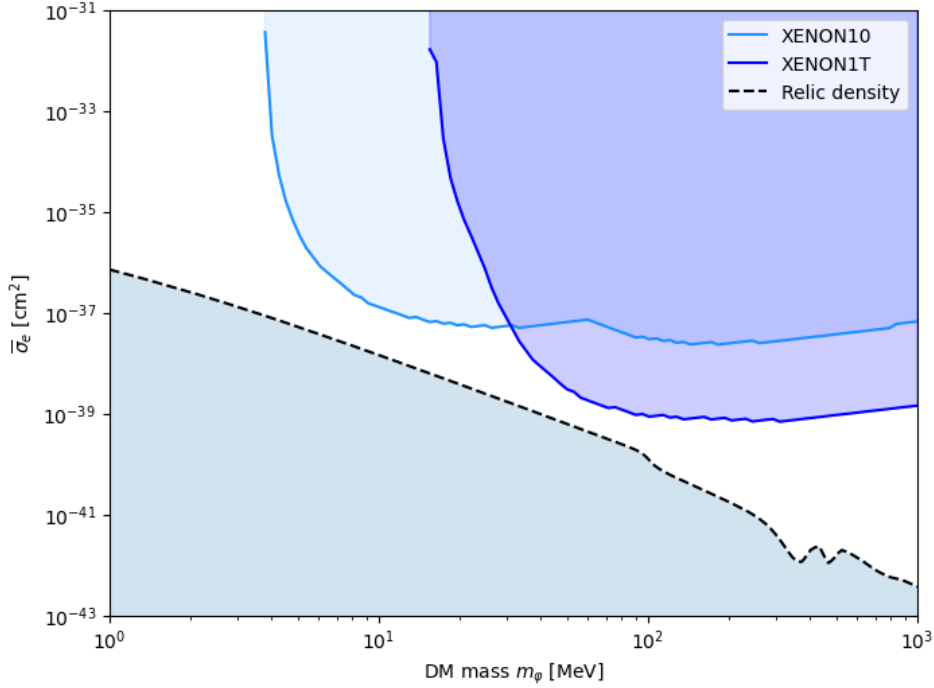
Figure 4.7: Exclusion limits at 95% C.L. on the cross section of scalar DM-e interaction mediated via a dark photon vs DM mass. The exclusion limits are computed using XENON10 and XENON1T data, which exclude respectively the light blue and blue regions of the plot. The dashed line shows the cross section for which the correct relic abundance is obtained from freeze-out. Above this line, the relic abundance is lower than the measured one; this region could be associated to a multi-component DM scenario, in which the DM particle considered in this model is a subdominant component of the DM particle content. Below this line (gray region), the relic abundance is bigger than the measured one, leading to overclosure of the Universe, therefore we exclude this region. The white region represents unconstrained parameter space.

Conclusions and outlook

As presented in Chapter 1, DM is a mysterious entity that we discovered more than a hundred years ago, however, its nature still remains unknown, even if its presence influences the Universe since its beginning. By studying the effects of DM on the evolution of the Universe, we can assume that DM must be a fundamental particle that the current SM does not describe.

We pointed out the current experimental effort that has been made in order to detect this elusive particle, and in Chapter 2, we described DM interactions with ordinary matter, focusing on DM-e interactions. In order to describe these interactions, being at low energy, we used a NREFT approach, and we showed how this can be linked with the high energy theories that could describe DM particles. In direct detection experiments, the electron that interacts with DM particles is bound to an atom; if the interaction with the DM particle is strong enough, the atom ionizes, and the scattered electron produces a measurable signal. To compute the ionization rate, we considered the effect of the atomic shells of xenon atoms, used in many direct detection experiments, described by the atomic response functions.

In order to produce exclusion limits on the parameters of the theory that describes DM particles, the use of a numerical tool is needed, and in Chapter 3 we introduced MaDDM, a numerical tool capable of calculating numerous DM observables for any given DM model. In this thesis, we expanded the MaDDM software, by implementing the computation of DM induced ionization rates, and the evaluation of the associated expected signal in XENON10 and XENON1T experiments. By comparing this signal with XENON10 and XENON1T experimental data for each point of the parameter space of the BSM theory, we obtain exclusion limits on such parameters.

In Chapter 4 we finally analysed simplified DM models for fermionic DM mediated by a vector, a scalar and a pseudo-scalar mediator, and we presented the exclusion limits on the non-relativistic coefficients that describe these type of interactions. We then described the scalar dark QED model, in which a scalar DM particle interacts with SM particles through a dark photon mediator. We evaluated the relic density of this model, from which we obtain a lower limit on the DM-e cross section, that is presented together with the upper limits on the DM-e cross section computed with MaDDM.

In this thesis we focused only on the relevant EFTs that describes the DM-e interaction,

which are the ones that are not suppressed by factors proportional to the exchanged momenta q, which is a very small quantity in direct detection experiments. Future prospects of this work may revolve into implementing the suppressed operators in MADDM, allowing to consider a wider choice of DM-e interactions.

In the next future, many new experiments with higher sensitivity to DM interactions will start to operate, and by adding these results to our analysis we will be able to constrain wider regions of the parameter space of DM models. This will lead to the rejection of many DM models, helping us to get closer to the solution of the DM problem.

Acknowledgments

I would like to express my deepest appreciation and gratitude to Professor Fabio Maltoni, for giving me the opportunity to work on this thesis at the *Centre for Cosmology, Particle Physics and Phenomenology* (CP3) with his research group.

I'm also deeply grateful to my supervisor at CP3 Chiara Arina, for the patience and immense support that gave me throughout these months. Your constant guidance and feedback were essential during this work.

My gratitude goes also to Olivier Mattelaer, for his invaluable assistance with MadGraph5_aMC@NLO and MadDM.

I want also to thank all the MadDM research group: Andrew Cheek, Daniele Massaro and Jan Heisig, for their precious contributions and insightful discussions throughout my project. Especially thanks to Andrew for all the support, insights and effort dedicated to me during this work, and Daniele, for patiently guiding me through the MadDM code.

I want to thank all the CP3 staff, and all the friends that I made during the time that I spent at CP3. I want to thank also Ivan and Malko, for the wonderful hospitality and friendship. This was a wonderful experience that I will always remember.

Vorrei anche ringraziare i miei amici di sempre. Nonostante la distanza e i periodi in cui sono stato lontano, la nostra amicizia è sempre rimasta la stessa di un tempo.

Ringrazio anche tutti gli amici che ho incontrato lungo questo percoso, con i quali ho condiviso sia triennale a Perugia che la magistrale a Bologna. Grazie per le risate a lezione, per gli esami preparati assieme nelle estati più torride, per tutti i pranzi in via Mazzini, e per tutti i momenti passati assieme. Questa esperienza non sarebbe stata la stessa senza di voi.

Grazie a Martina, per essere stata al mio fianco in questi anni intensi. Grazie per tutto il sostegno e l'incoraggiamento che mi hai dato durante questo percorso. Sei il motivo per cui non vedevo l'ora di tornare a casa ogni volta che partivo.

Vorrei ringraziare infine la mia famiglia, che mi è stata sempre vicino durante questi anni. Grazie per aver festeggiato con me i miei successi, ma soprattuto per avermi dato conforto nei momenti più difficili. Grazie nonna Lilla, per ogni tua preghiera prima di un esame, e per le merende che mi preparavi per festeggiare quando tornavo a casa. Non dimenticherò mai il tuo sostegno.

Bibliography

[1] Lord Kelvin. "Baltimore Lectures on Molecular Dynamics and the Wave Theory of Light". In: *Cambridge Library Collection - Physical Sciences* (1884).

[2] M. Schwarzschild. "Mass distribution and mass-luminosity ratio in galaxies". In: *Astronomical Journal* 59 (Sept. 1954), p. 273.

[3] F. Zwicky. "Die Rotverschiebung von extragalaktischen Nebeln". In: *Helv. Phys. Acta* 6 (1933), pp. 110–127. DOI: 10.1007/s10714-008-0707-4.

[4] V C Rubin and W K Ford Jr. "Rotation of the Andromeda nebula from a spectroscopic survey of emission regions". In: *Astrophys. J. 159: 379-403(Feb 1970).* (Jan. 1970). DOI: 10.1086/150317. URL: https://www.osti.gov/biblio/4148861.

[5] Albert Bosma. "The distribution and kinematics of neutral hydrogen in spiral galaxies of various morphological types". PhD thesis. University of Groningen, 1978.

[6] R. H. Miller, K. H. Prendergast, and William J. Quirk. "Numerical Experiments on Spiral Structure". In: *Astrophysical Journal* 161 (Sept. 1970), p. 903. DOI: 10.1086/150593.

[7] Frank Hohl. "Numerical Experiments with a Disk of Stars". In: *Astrophysical Journal* 168 (Sept. 1971), p. 343. DOI: 10.1086/151091.

[8] J. P. Ostriker and P. J. E. Peebles. "A Numerical Study of the Stability of Flattened Galaxies: or, can Cold Galaxies Survive?" In: *Astrophysical Journal* 186 (Dec. 1973), pp. 467–480. DOI: 10.1086/152513.

[9] S. M. Faber and J. S. Gallagher. "Masses and Mass-To-Light Ratios of Galaxies". In: *Annual Review of Astronomy and Astrophysics* 17.1 (1979), pp. 135–187. DOI: 10.1146/annurev.aa.17.090179.001031. eprint: https://doi.org/10.1146/annurev.aa.17.090179.001031. URL: https://doi.org/10.1146/annurev.aa.17.090179.001031.

[10] M. Milgrom. "A modification of the Newtonian dynamics as a possible alternative to the hidden mass hypothesis." In: *Astrophysical Journal* 270 (July 1983), pp. 365–370. DOI: 10.1086/161130.

[11] M. Milgrom. "A modification of the Newtonian dynamics - Implications for galaxies." In: *Astrophysical Journal* 270 (July 1983), pp. 371–383. DOI: 10.1086/161131.

[12] Richard Massey, Thomas Kitching, and Johan Richard. "The dark matter of gravitational lensing". In: *Reports on Progress in Physics* 73.8 (July 2010), p. 086901. DOI: 10.1088/0034-4885/73/8/086901. URL: https://doi.org/10.1088%2F0034-4885%2F73%2F8%2F086901.

[13] J. D. Bekenstein. "Relativistic gravitation theory for the MOND paradigm". In: *Phys. Rev.* D70 (2004), p. 083509.

[14] R. H. Sanders. "Clusters of galaxies with modified Newtonian dynamics". In: *Monthly Notices of the Royal Astronomical Society* 342.3 (July 2003), pp. 901–908. DOI: 10.1046/j.1365-8711.2003.06596.x. URL: https://doi.org/10.1046%2Fj.1365-8711.2003.06596.x.

[15] Douglas Clowe et al. "A Direct Empirical Proof of the Existence of Dark Matter". In: *The Astrophysical Journal* 648.2 (Aug. 2006), pp. L109–L113. ISSN: 1538-4357. DOI: 10.1086/508162. URL: http://dx.doi.org/10.1086/508162.

[16] David Harvey et al. "Looking for dark matter trails in colliding galaxy clusters". In: *Monthly Notices of the Royal Astronomical Society* 464.4 (Oct. 2016), pp. 3991–3997. DOI: 10.1093/mnras/stw2671. URL: https://doi.org/10.1093%2Fmnras%2Fstw2671.

[17] T. Lasserre. "Not enough stellar mass machos in the galactic halo". In: *Astron. Astrophys.* 355 (2000), pp. L39–L42. arXiv: astro-ph/0002253.

[18] Max Tegmark et al. "Dimensionless constants, cosmology, and other dark matters". In: *Physical Review D* 73.2 (Jan. 2006). DOI: 10.1103/physrevd.73.023505. URL: https://doi.org/10.1103%2Fphysrevd.73.023505.

[19] Edward W. Kolb and Michael S. Turner. *The Early Universe*. Vol. 69. 1990. ISBN: 978-0-201-62674-2. DOI: 10.1201/9780429492860.

[20] R. A. Alpher, H. Bethe, and G. Gamow. "The Origin of Chemical Elements". In: *Phys. Rev.* 73 (7 Apr. 1948), pp. 803–804. DOI: 10.1103/PhysRev.73.803. URL: https://link.aps.org/doi/10.1103/PhysRev.73.803.

[21] K.A. Olive. "Review of Particle Physics". In: *Chinese Physics C* 38.9 (Aug. 2014), p. 090001. DOI: 10.1088/1674-1137/38/9/090001. URL: https://doi.org/10.1088%2F1674-1137%2F38%2F9%2F090001.

[22] J. Beringer et al. "Review of Particle Physics". In: *Phys. Rev. D* 86 (1 July 2012), p. 010001. DOI: 10.1103/PhysRevD.86.010001. URL: https://link.aps.org/doi/10.1103/PhysRevD.86.010001.

[23] and P. A. R. Ade et al. "Planck 2015 results". In: *Astronomy & Astrophysics* 594 (Sept. 2016), A13. DOI: 10.1051/0004-6361/201525830. URL: `https://doi.org/10.1051%2F0004-6361%2F201525830`.

[24] Ryan J. Cooke et al. "PRECISION MEASURES OF THE PRIMORDIAL ABUNDANCE OF DEUTERIUM". In: *The Astrophysical Journal* 781.1 (Jan. 2014), p. 31. DOI: 10.1088/0004-637x/781/1/31. URL: `https://doi.org/10.1088%2F0004-637x%2F781%2F1%2F31`.

[25] P. J. E. Peebles. "Recombination of the Primeval Plasma". In: *Astrophysical Journal* 153 (July 1968), p. 1. DOI: 10.1086/149628.

[26] Victor S. Alpher. *Ralph A. Alpher, George Antonovich Gamow, and the Prediction of the Cosmic Microwave Background Radiation*. 2014. arXiv: 1411.0172 [physics.hist-ph].

[27] and N. Aghanim et al. "Planck 2018 results". In: *Astronomy & Astrophysics* 641 (Sept. 2020), A6. DOI: 10.1051/0004-6361/201833910. URL: `https://doi.org/10.1051%2F0004-6361%2F201833910`.

[28] C. L. Bennett et al. "Nine-year Wilkinson Microwave Anisotropy Probe (WMAP) Observations: Final Maps and Results". In: *The Astrophysical Journal Supplement Series* 208.2 (Sept. 2013), p. 20. DOI: 10.1088/0067-0049/208/2/20. URL: `https://doi.org/10.1088%2F0067-0049%2F208%2F2%2F20`.

[29] G. Hinshaw et al. "Nine-year Wilkinson Microwave Anisotropy Probe (WMAP) Observations: Cosmological Parameter Results". In: *The Astrophysical Journal Supplement Series* 208.2 (Sept. 2013), p. 19. DOI: 10.1088/0067-0049/208/2/19. URL: `https://doi.org/10.1088%2F0067-0049%2F208%2F2%2F19`.

[30] Wayne Hu, Naoshi Sugiyama, and Joseph Silk. "The physics of microwave background anisotropies". In: *Nature* 386.6620 (Mar. 1997), pp. 37–43. DOI: 10.1038/386037a0. URL: `https://doi.org/10.1038%2F386037a0`.

[31] M. Markevitch et al. "Direct Constraints on the Dark Matter Self-Interaction Cross Section from the Merging Galaxy Cluster 1E 0657-56". In: *The Astrophysical Journal* 606.2 (May 2004), pp. 819–824. DOI: 10.1086/383178. URL: `https://doi.org/10.1086%2F383178`.

[32] Simon D. M. White et al. "Clusters, Filaments, and Voids in a Universe Dominated by Cold Dark Matter". In: *Astrophysical Journal* 313 (Feb. 1987), p. 505. DOI: 10.1086/164990.

[33] Adrian L. Melott et al. "Cluster Analysis of the Nonlinear Evolution of Large-Scale Structure in an Axion/Gravitino/Photino-Dominated Universe". In: *Phys. Rev. Lett.* 51 (10 Sept. 1983), pp. 935–938. DOI: 10.1103/PhysRevLett.51.935. URL: `https://link.aps.org/doi/10.1103/PhysRevLett.51.935`.

[34] Andrew Cheek. "Preparing for Dark Matter: Maximising our discrimination power in the event of detection". PhD thesis. Durham University, 2019.

[35] Paolo Gondolo and Graciela Gelmini. "Cosmic abundances of stable particles: Improved analysis". In: *Nuclear Physics B* 360.1 (1991), pp. 145–179. ISSN: 0550-3213. DOI: `https://doi.org/10.1016/0550-3213(91)90438-4`. URL: `https://www.sciencedirect.com/science/article/pii/0550321391904384`.

[36] Susanne Mertens. "Direct Neutrino Mass Experiments". In: *Journal of Physics: Conference Series* 718 (May 2016), p. 022013. DOI: `10.1088/1742-6596/718/2/022013`. URL: `https://doi.org/10.1088%2F1742-6596%2F718%2F2%2F022013`.

[37] Benjamin W. Lee and Steven Weinberg. "Cosmological Lower Bound on Heavy-Neutrino Masses". In: *Phys. Rev. Lett.* 39 (4 July 1977), pp. 165–168. DOI: `10.1103/PhysRevLett.39.165`. URL: `https://link.aps.org/doi/10.1103/PhysRevLett.39.165`.

[38] P. Hut. "Limits on masses and number of neutral weakly interacting particles". In: *Physics Letters B* 69.1 (1977), pp. 85–88. ISSN: 0370-2693. DOI: `https://doi.org/10.1016/0370-2693(77)90139-3`. URL: `https://www.sciencedirect.com/science/article/pii/0370269377901393`.

[39] Kim Griest and Marc Kamionkowski. "Unitarity limits on the mass and radius of dark-matter particles". In: *Phys. Rev. Lett.* 64 (6 Feb. 1990), pp. 615–618. DOI: `10.1103/PhysRevLett.64.615`. URL: `https://link.aps.org/doi/10.1103/PhysRevLett.64.615`.

[40] Kaustubh Agashe et al. "(In)direct detection of boosted dark matter". In: *Journal of Cosmology and Astroparticle Physics* 2014.10 (Oct. 2014), pp. 062–062. DOI: `10.1088/1475-7516/2014/10/062`. URL: `https://doi.org/10.1088%2F1475-7516%2F2014%2F10%2F062`.

[41] C. Bœhm and P. Fayet. "Scalar dark matter candidates". In: *Nuclear Physics B* 683.1-2 (Apr. 2004), pp. 219–263. DOI: `10.1016/j.nuclphysb.2004.01.015`. URL: `https://doi.org/10.1016%2Fj.nuclphysb.2004.01.015`.

[42] John McDonald. "Thermally Generated Gauge Singlet Scalars as Self-Interacting Dark Matter". In: *Physical Review Letters* 88.9 (Feb. 2002). DOI: `10.1103/physrevlett.88.091304`. URL: `https://doi.org/10.1103%2Fphysrevlett.88.091304`.

[43] Lawrence J. Hall et al. "Freeze-in production of FIMP dark matter". In: *Journal of High Energy Physics* 2010.3 (Mar. 2010). DOI: `10.1007/jhep03(2010)080`. URL: `https://doi.org/10.1007%2Fjhep03%282010%29080`.

[44] Saniya Heeba, Felix Kahlhoefer, and Patrick Stöcker. "Freeze-in production of decaying dark matter in five steps". In: *Journal of Cosmology and Astroparticle Physics* 2018.11 (Nov. 2018), pp. 048–048. DOI: 10.1088/1475-7516/2018/11/048. URL: https://doi.org/10.1088%2F1475-7516%2F2018%2F11%2F048.

[45] Jonathan L. Feng, Arvind Rajaraman, and Fumihiro Takayama. "Superweakly Interacting Massive Particles". In: *Physical Review Letters* 91.1 (July 2003). DOI: 10.1103/physrevlett.91.011302. URL: https://doi.org/10.1103%2Fphysrevlett.91.011302.

[46] M. Ackermann et al. "Searching for Dark Matter Annihilation from Milky Way Dwarf Spheroidal Galaxies with Six Years of Fermi Large Area Telescope Data". In: *Physical Review Letters* 115.23 (Nov. 2015). DOI: 10.1103/physrevlett.115.231301. URL: https://doi.org/10.1103%2Fphysrevlett.115.231301.

[47] A. A. Abdo et al. "OBSERVATIONS OF MILKY WAY DWARF SPHEROIDAL GALAXIES WITH THE FERMI-LARGE AREA TELESCOPE DETECTOR AND CONSTRAINTS ON DARK MATTER MODELS". In: *The Astrophysical Journal* 712.1 (Feb. 2010), pp. 147–158. ISSN: 1538-4357. DOI: 10.1088/0004-637x/712/1/147. URL: http://dx.doi.org/10.1088/0004-637X/712/1/147.

[48] A. Abramowski et al. "Search for Photon-Linelike Signatures from Dark Matter Annihilations with H.E.S.S." In: *Physical Review Letters* 110.4 (Jan. 2013). DOI: 10.1103/physrevlett.110.041301. URL: https://doi.org/10.1103%2Fphysrevlett.110.041301.

[49] A. U. Abeysekara et al. "Sensitivity of HAWC to high-mass dark matter annihilations". In: *Physical Review D* 90.12 (Dec. 2014). DOI: 10.1103/physrevd.90.122002. URL: https://doi.org/10.1103%2Fphysrevd.90.122002.

[50] M. G. Aartsen et al. "Search for neutrinos from dark matter self-annihilations in the center of the Milky Way with 3 years of IceCube/DeepCore". In: *The European Physical Journal C* 77.9 (Sept. 2017). DOI: 10.1140/epjc/s10052-017-5213-y. URL: https://doi.org/10.1140%2Fepjc%2Fs10052-017-5213-y.

[51] Nadège Iovine et al. *Combined Search for Neutrinos from Dark Matter Annihilation in the Galactic Centre using ANTARES and IceCube.* 2019. arXiv: 1908.07300 [astro-ph.HE].

[52] Mark Srednicki, Keith A. Olive, and Joseph Silk. "High-energy neutrinos from the sun and cold dark matter". In: *Nuclear Physics B* 279.3 (1987), pp. 804–823. ISSN: 0550-3213. DOI: https://doi.org/10.1016/0550-3213(87)90020-4. URL: https://www.sciencedirect.com/science/article/pii/0550321387900204.

[53] Andrei Kounine. "The Alpha Magnetic Spectrometer on the International Space Station". In: *Int. J. Mod. Phys. E* 21.08 (2012), p. 1230005. DOI: 10.1142/S0218301312300056.

[54] O. Adriani et al. "An anomalous positron abundance in cosmic rays with energies 1.5–100 GeV". In: *Nature* 458.7238 (Apr. 2009), pp. 607–609. DOI: 10.1038/nature07942. URL: https://doi.org/10.1038%2Fnature07942.

[55] "Constraints on mediator-based dark matter and scalar dark energy models using $\sqrt{s} = 13$ TeV pp collision data collected by the ATLAS detector". In: *Journal of High Energy Physics* 2019.5 (May 2019). DOI: 10.1007/jhep05(2019)142. URL: https://doi.org/10.1007%2Fjhep05%282019%29142.

[56] Adish Vartak. "Dark matter search in CMS". In: (2017). Ed. by Etienne Auge, Jacques Dumarchez, and Jean Tran Thanh Van, pp. 225–233.

[57] Mark W. Goodman and Edward Witten. "Detectability of Certain Dark Matter Candidates". In: *Phys. Rev. D* 31 (1985). Ed. by M. A. Srednicki, p. 3059. DOI: 10.1103/PhysRevD.31.3059.

[58] Joel R. Primack, David Seckel, and Bernard Sadoulet. "Detection of Cosmic Dark Matter". In: *Ann. Rev. Nucl. Part. Sci.* 38 (1988), pp. 751–807. DOI: 10.1146/annurev.ns.38.120188.003535.

[59] Jocelyn Monroe and Peter Fisher. "Neutrino backgrounds to dark matter searches". In: *Physical Review D* 76.3 (Aug. 2007). DOI: 10.1103/physrevd.76.033007. URL: https://doi.org/10.1103%2Fphysrevd.76.033007.

[60] Louis E Strigari. "Neutrino coherent scattering rates at direct dark matter detectors". In: *New Journal of Physics* 11.10 (Oct. 2009), p. 105011. DOI: 10.1088/1367-2630/11/10/105011. URL: https://doi.org/10.1088%2F1367-2630%2F11%2F10%2F105011.

[61] J. Billard, E. Figueroa-Feliciano, and L. Strigari. "Implication of neutrino backgrounds on the reach of next generation dark matter direct detection experiments". In: *Physical Review D* 89.2 (Jan. 2014). DOI: 10.1103/physrevd.89.023524. URL: https://doi.org/10.1103%2Fphysrevd.89.023524.

[62] Xiangyi Cui et al. "Dark Matter Results from 54-Ton-Day Exposure of PandaX-II Experiment". In: *Physical Review Letters* 119.18 (Oct. 2017). DOI: 10.1103/physrevlett.119.181302. URL: https://doi.org/10.1103%2Fphysrevlett.119.181302.

[63] R. Agnese et al. "Search for low-mass dark matter with CDMSlite using a profile likelihood fit". In: *Physical Review D* 99.6 (Mar. 2019). DOI: 10.1103/physrevd.99.062001. URL: https://doi.org/10.1103%2Fphysrevd.99.062001.

[64] C. Amole et al. "Dark Matter Search Results from the PICO$-$60 C_3F_8 Bubble Chamber". In: *Phys. Rev. Lett.* 118 (25 June 2017), p. 251301. DOI: 10.1103/PhysRevLett.118.251301. URL: https://link.aps.org/doi/10.1103/PhysRevLett.118.251301.

[65] P. Agnes et al. "DarkSide-50 532-day dark matter search with low-radioactivity argon". In: *Physical Review D* 98.10 (Nov. 2018). DOI: `10.1103/physrevd.98.102006`. URL: `https://doi.org/10.1103%2Fphysrevd.98.102006`.

[66] A. H. Abdelhameed et al. "First results from the CRESST-III low-mass dark matter program". In: *Phys. Rev. D* 100 (10 Nov. 2019), p. 102002. DOI: `10.1103/PhysRevD.100.102002`. URL: `https://link.aps.org/doi/10.1103/PhysRevD.100.102002`.

[67] L. Hehn et al. "Improved EDELWEISS-III sensitivity for low-mass WIMPs using a profile likelihood approach". In: *The European Physical Journal C* 76.10 (Oct. 2016). DOI: `10.1140/epjc/s10052-016-4388-y`. URL: `https://doi.org/10.1140%2Fepjc%2Fs10052-016-4388-y`.

[68] P. Agnes et al. "Low-Mass Dark Matter Search with the DarkSide-50 Experiment". In: *Physical Review Letters* 121.8 (Aug. 2018). DOI: `10.1103/physrevlett.121.081307`. URL: `https://doi.org/10.1103%2Fphysrevlett.121.081307`.

[69] D. S. Akerib et al. "Results from a Search for Dark Matter in the Complete LUX Exposure". In: *Physical Review Letters* 118.2 (Jan. 2017). DOI: `10.1103/physrevlett.118.021303`. URL: `https://doi.org/10.1103%2Fphysrevlett.118.021303`.

[70] E. Aprile et al. "Search for Coherent Elastic Scattering of Solar ^{8}**B** neutrinos in the XENON1T Dark Matter Experiment". In: *Physical Review Letters* 126.9 (Mar. 2021). DOI: `10.1103/physrevlett.126.091301`. URL: `https://doi.org/10.1103%2Fphysrevlett.126.091301`.

[71] R. Ajaj et al. "Search for dark matter with a 231-day exposure of liquid argon using DEAP-3600 at SNOLAB". In: *Physical Review D* 100.2 (July 2019). DOI: `10.1103/physrevd.100.022004`. URL: `https://doi.org/10.1103%2Fphysrevd.100.022004`.

[72] Ciaran A. J. O'Hare. "New Definition of the Neutrino Floor for Direct Dark Matter Searches". In: *Physical Review Letters* 127.25 (Dec. 2021). DOI: `10.1103/physrevlett.127.251802`. URL: `https://doi.org/10.1103%2Fphysrevlett.127.251802`.

[73] D. S. Akerib et al. *Snowmass2021 Cosmic Frontier Dark Matter Direct Detection to the Neutrino Fog.* 2022. arXiv: `2203.08084` `[hep-ex]`.

[74] E. Aprile et al. "Dark Matter Search Results from a One Ton-Year Exposure of XENON1T". In: *Physical Review Letters* 121.11 (Sept. 2018). DOI: `10.1103/physrevlett.121.111302`. URL: `https://doi.org/10.1103%2Fphysrevlett.121.111302`.

[75] D. S. Akerib et al. "Projected WIMP sensitivity of the LUX-ZEPLIN dark matter experiment". In: *Physical Review D* 101.5 (Mar. 2020). DOI: `10.1103/physrevd.101.052002`. URL: `https://doi.org/10.1103%2Fphysrevd.101.052002`.

[76] E. Aprile et al. "Physics reach of the XENON1T dark matter experiment." In: *Journal of Cosmology and Astroparticle Physics* 2016.04 (Apr. 2016), pp. 027–027. DOI: `10.1088/1475-7516/2016/04/027`. URL: `https://doi.org/10.1088%2F1475-7516%2F2016%2F04%2F027`.

[77] J. Aalbers et al. "DARWIN: towards the ultimate dark matter detector". In: *Journal of Cosmology and Astroparticle Physics* 2016.11 (Nov. 2016), pp. 017–017. DOI: `10.1088/1475-7516/2016/11/017`. URL: `https://doi.org/10.1088%2F1475-7516%2F2016%2F11%2F017`.

[78] C. E. Aalseth et al. "DarkSide-20k: A 20 tonne two-phase LAr TPC for direct dark matter detection at LNGS". In: *The European Physical Journal Plus* 133.3 (Mar. 2018). DOI: `10.1140/epjp/i2018-11973-4`. URL: `https://doi.org/10.1140%2Fepjp%2Fi2018-11973-4`.

[79] K. Schneck et al. "Dark matter effective field theory scattering in direct detection experiments". In: *Physical Review D* 91.9 (May 2015). DOI: `10.1103/physrevd.91.092004`. URL: `https://doi.org/10.1103%2Fphysrevd.91.092004`.

[80] Q. Arnaud et al. "First results from the NEWS-G direct dark matter search experiment at the LSM". In: *Astroparticle Physics* 97 (Jan. 2018), pp. 54–62. DOI: `10.1016/j.astropartphys.2017.10.009`. URL: `https://doi.org/10.1016%2Fj.astropartphys.2017.10.009`.

[81] L. Balogh et al. "The NEWS-G detector at SNOLAB". In: *Journal of Instrumentation* 18.02 (Feb. 2023), T02005. DOI: `10.1088/1748-0221/18/02/t02005`. URL: `https://doi.org/10.1088%2F1748-0221%2F18%2F02%2Ft02005`.

[82] Michael Crisler et al. "SENSEI: First Direct-Detection Constraints on Sub-GeV Dark Matter from a Surface Run". In: *Phys. Rev. Lett.* 121 (6 Aug. 2018), p. 061803. DOI: `10.1103/PhysRevLett.121.061803`. URL: `https://link.aps.org/doi/10.1103/PhysRevLett.121.061803`.

[83] Orr Abramoff et al. "SENSEI: Direct-Detection Constraints on Sub-GeV Dark Matter from a Shallow Underground Run Using a Prototype Skipper CCD". In: *Phys. Rev. Lett.* 122 (16 Apr. 2019), p. 161801. DOI: `10.1103/PhysRevLett.122.161801`. URL: `https://link.aps.org/doi/10.1103/PhysRevLett.122.161801`.

[84] Liron Barak et al. "SENSEI: Direct-Detection Results on sub-GeV Dark Matter from a New Skipper CCD". In: *Phys. Rev. Lett.* 125 (17 Oct. 2020), p. 171802. DOI: `10.1103/PhysRevLett.125.171802`. URL: `https://link.aps.org/doi/10.1103/PhysRevLett.125.171802`.

[85]   R. Agnese et al. "First Dark Matter Constraints from a SuperCDMS Single-Charge Sensitive Detector". In: *Phys. Rev. Lett.* 121 (5 Aug. 2018), p. 051301. DOI: `10.1103/PhysRevLett.121.051301`. URL: `https://link.aps.org/doi/10.1103/PhysRevLett.121.051301`.

[86]   D. W. Amaral et al. "Constraints on low-mass, relic dark matter candidates from a surface-operated SuperCDMS single-charge sensitive detector". In: *Phys. Rev. D* 102 (9 Nov. 2020), p. 091101. DOI: `10.1103/PhysRevD.102.091101`. URL: `https://link.aps.org/doi/10.1103/PhysRevD.102.091101`.

[87]   A. Aguilar-Arevalo et al. "Constraints on Light Dark Matter Particles Interacting with Electrons from DAMIC at SNOLAB". In: *Phys. Rev. Lett.* 123 (18 Oct. 2019), p. 181802. DOI: `10.1103/PhysRevLett.123.181802`. URL: `https://link.aps.org/doi/10.1103/PhysRevLett.123.181802`.

[88]   Q. Arnaud et al. "First Germanium-Based Constraints on Sub-MeV Dark Matter with the EDELWEISS Experiment". In: *Phys. Rev. Lett.* 125 (14 Oct. 2020), p. 141301. DOI: `10.1103/PhysRevLett.125.141301`. URL: `https://link.aps.org/doi/10.1103/PhysRevLett.125.141301`.

[89]   P. Agnes et al. "Constraints on Sub-GeV Dark-Matter–Electron Scattering from the DarkSide-50 Experiment". In: *Physical Review Letters* 121.11 (Sept. 2018). DOI: `10.1103/physrevlett.121.111303`. URL: `https://doi.org/10.1103%2Fphysrevlett.121.111303`.

[90]   Rouven Essig et al. "First Direct Detection Limits on Sub-GeV Dark Matter from XENON10". In: *Physical Review Letters* 109.2 (July 2012). DOI: `10.1103/physrevlett.109.021301`. URL: `https://doi.org/10.1103%2Fphysrevlett.109.021301`.

[91]   J. Angle et al. "Search for Light Dark Matter in XENON10 Data". In: *Physical Review Letters* 107.5 (July 2011). DOI: `10.1103/physrevlett.107.051301`. URL: `https://doi.org/10.1103%2Fphysrevlett.107.051301`.

[92]   Rouven Essig, Jeremy Mardon, and Tomer Volansky. "Direct detection of sub-GeV dark matter". In: *Physical Review D* 85.7 (Apr. 2012). DOI: `10.1103/physrevd.85.076007`. URL: `https://doi.org/10.1103%2Fphysrevd.85.076007`.

[93]   E. Aprile et al. "Low-mass dark matter search using ionization signals in XENON100". In: *Phys. Rev. D* 94 (9 Nov. 2016), p. 092001. DOI: `10.1103/PhysRevD.94.092001`. URL: `https://link.aps.org/doi/10.1103/PhysRevD.94.092001`.

[94]   E. Aprile et al. "Light Dark Matter Search with Ionization Signals in XENON1T". In: *Physical Review Letters* 123.25 (Dec. 2019). DOI: `10.1103/physrevlett.123.251801`. URL: `https://doi.org/10.1103%2Fphysrevlett.123.251801`.

[95] E. Aprile et al. "Emission of single and few electrons in XENON1T and limits on light dark matter". In: *Phys. Rev. D* 106 (2 July 2022), p. 022001. DOI: `10.1103/PhysRevD.106.022001`. URL: `https://link.aps.org/doi/10.1103/PhysRevD.106.022001`.

[96] Chen Cheng et al. "Search for Light Dark Matter–Electron Scattering in the PandaX-II Experiment". In: *Phys. Rev. Lett.* 126 (21 May 2021), p. 211803. DOI: `10.1103/PhysRevLett.126.211803`. URL: `https://link.aps.org/doi/10.1103/PhysRevLett.126.211803`.

[97] Carlos Blanco et al. "Dark matter-electron scattering from aromatic organic targets". In: *Phys. Rev. D* 101 (5 Mar. 2020), p. 056001. DOI: `10.1103/PhysRevD.101.056001`. URL: `https://link.aps.org/doi/10.1103/PhysRevD.101.056001`.

[98] Rouven Essig et al. *Snowmass2021 Cosmic Frontier: The landscape of low-threshold dark matter direct detection in the next decade.* 2023. arXiv: `2203.08297 [hep-ph]`.

[99] Riccardo Catena et al. "Atomic responses to general dark matter-electron interactions". In: *Physical Review Research* 2.3 (Aug. 2020). DOI: `10.1103/physrevresearch.2.033195`. URL: `https://doi.org/10.1103%2Fphysrevresearch.2.033195`.

[100] Timon Emken. *Dark Atomic Response Tabulator (DarkART)[Code, v0.1.0]*. The code can be found under `https://github.com/temken/darkart`. Version v0.1.0. 2021. DOI: `DOI:10.5281/zenodo.6046225`. URL: `https://doi.org/10.5281/zenodo.6046225`.

[101] J I Read. "The local dark matter density". In: *Journal of Physics G: Nuclear and Particle Physics* 41.6 (May 2014), p. 063101. DOI: `10.1088/0954-3899/41/6/063101`. URL: `https://doi.org/10.1088%2F0954-3899%2F41%2F6%2F063101`.

[102] F. J. Kerr and D. Lynden-Bell. "Review of galactic constants." In: *Monthly Notices of the Royal Astronomical Society* 221 (Aug. 1986), pp. 1023–1038. DOI: `10.1093/mnras/221.4.1023`.

[103] M. C. Smith et al. "The RAVE survey: constraining the local Galactic escape speed". In: *Monthly Notices of the Royal Astronomical Society* 379.2 (Aug. 2007), pp. 755–772. DOI: `10.1111/j.1365-2966.2007.11964.x`. URL: `https://doi.org/10.1111%2Fj.1365-2966.2007.11964.x`.

[104] Timon Emken. *Dark Matter in the Earth and the Sun – Simulating Underground Scatterings for the Direct Detection of Low-Mass Dark Matter.* 2019. arXiv: `1906.07541 [hep-ph]`.

[105] Rouven Essig et al. *Direct Detection of sub-GeV Dark Matter with Semiconductor Targets.* 2016. arXiv: `1509.01598 [hep-ph]`.

[106] Michael Kuhlen et al. "Dark matter direct detection with non-Maxwellian velocity structure". In: *Journal of Cosmology and Astroparticle Physics* 2010.02 (Feb. 2010), pp. 030–030. DOI: 10.1088/1475-7516/2010/02/030. URL: https://doi.org/10.1088%2F1475-7516%2F2010%2F02%2F030.

[107] Michael Kuhlen, Mariangela Lisanti, and David N. Spergel. "Direct detection of dark matter debris flows". In: *Physical Review D* 86.6 (Sept. 2012). DOI: 10.1103/physrevd.86.063505. URL: https://doi.org/10.1103%2Fphysrevd.86.063505.

[108] Lina Necib et al. "Under the FIRElight: Stellar Tracers of the Local Dark Matter Velocity Distribution in the Milky Way". In: *The Astrophysical Journal* 883.1 (Sept. 2019), p. 27. DOI: 10.3847/1538-4357/ab3afc. URL: https://doi.org/10.3847%2F1538-4357%2Fab3afc.

[109] Jonah Herzog-Arbeitman et al. "Empirical Determination of Dark Matter Velocities Using Metal-Poor Stars". In: *Physical Review Letters* 120.4 (Jan. 2018). DOI: 10.1103/physrevlett.120.041102. URL: https://doi.org/10.1103%2Fphysrevlett.120.041102.

[110] Jonah Herzog-Arbeitman, Mariangela Lisanti, and Lina Necib. "The metal-poor stellar halo in RAVE-TGAS and its implications for the velocity distribution of dark matter". In: *Journal of Cosmology and Astroparticle Physics* 2018.04 (Apr. 2018), pp. 052–052. DOI: 10.1088/1475-7516/2018/04/052. URL: https://doi.org/10.1088%2F1475-7516%2F2018%2F04%2F052.

[111] Lina Necib, Mariangela Lisanti, and Vasily Belokurov. "Inferred Evidence for Dark Matter Kinematic Substructure with SDSS-Gaia". In: *The Astrophysical Journal* 874.1 (Mar. 2019), p. 3. DOI: 10.3847/1538-4357/ab095b. URL: https://doi.org/10.3847%2F1538-4357%2Fab095b.

[112] D. S. Akerib et al. "Improved Limits on Scattering of Weakly Interacting Massive Particles from Reanalysis of 2013 LUX Data". In: *Physical Review Letters* 116.16 (Apr. 2016). DOI: 10.1103/physrevlett.116.161301. URL: https://doi.org/10.1103%2Fphysrevlett.116.161301.

[113] E.A. Paschos, A. Pilaftsis, and K. Zioutas. "On the possibility of improving the sensitivity of dark-matter detection". In: *Physics Letters B* 236.3 (1990), pp. 321–326. ISSN: 0370-2693. DOI: https://doi.org/10.1016/0370-2693(90)90990-N. URL: https://www.sciencedirect.com/science/article/pii/037026939090990N.

[114] L. Baudis et al. "Signatures of dark matter scattering inelastically off nuclei". In: *Physical Review D* 88.11 (Dec. 2013). DOI: 10.1103/physrevd.88.115014. URL: https://doi.org/10.1103%2Fphysrevd.88.115014.

[115] Christopher McCabe. "Prospects for dark matter detection with inelastic transitions of xenon". In: *Journal of Cosmology and Astroparticle Physics* 2016.05 (May 2016), pp. 033–033. DOI: 10.1088/1475-7516/2016/05/033. URL: https://doi.org/10.1088%2F1475-7516%2F2016%2F05%2F033.

[116] XMASS Collaboration et al. *Direct dark matter searches with the full data set of XMASS-I.* 2022. arXiv: 2211.06204 [astro-ph.CO].

[117] Marco Cirelli, Eugenio Del Nobile, and Paolo Panci. "Tools for model-independent bounds in direct dark matter searches". In: *Journal of Cosmology and Astroparticle Physics* 2013.10 (Oct. 2013), pp. 019–019. DOI: 10.1088/1475-7516/2013/10/019. URL: https://doi.org/10.1088%2F1475-7516%2F2013%2F10%2F019.

[118] M Nowakowski, E A Paschos, and J M Rodriguez. "All electromagnetic form factors". In: *European Journal of Physics* 26.4 (Apr. 2005), pp. 545–560. DOI: 10.1088/0143-0807/26/4/001. URL: https://doi.org/10.1088%2F0143-0807%2F26%2F4%2F001.

[119] Nikhil Anand, A. Liam Fitzpatrick, and W. C. Haxton. "Weakly interacting massive particle-nucleus elastic scattering response". In: *Physical Review C* 89.6 (June 2014). DOI: 10.1103/physrevc.89.065501. URL: https://doi.org/10.1103%2Fphysrevc.89.065501.

[120] Federico Ambrogi et al. "MadDM v.3.0: A comprehensive tool for dark matter studies". In: *Physics of the Dark Universe* 24 (Mar. 2019), p. 100249. DOI: 10.1016/j.dark.2018.11.009. URL: https://doi.org/10.1016%2Fj.dark.2018.11.009.

[121] Céline Degrande et al. "UFO – The Universal FeynRules Output". In: *Computer Physics Communications* 183.6 (June 2012), pp. 1201–1214. DOI: 10.1016/j.cpc.2012.01.022. URL: https://doi.org/10.1016%2Fj.cpc.2012.01.022.

[122] Mihailo Backović, Kyoungchul Kong, and Mathew McCaskey. "MadDM v.1.0: Computation of dark matter relic abundance using MadGraph 5". In: *Physics of the Dark Universe* 5-6 (Dec. 2014), pp. 18–28. DOI: 10.1016/j.dark.2014.04.001. URL: https://doi.org/10.1016%2Fj.dark.2014.04.001.

[123] Mihailo Backović et al. "Direct detection of dark matter with MadDM v.2.0". In: *Physics of the Dark Universe* 9-10 (Sept. 2015), pp. 37–50. DOI: 10.1016/j.dark.2015.09.001. URL: https://doi.org/10.1016%2Fj.dark.2015.09.001.

[124] Carlos Faham. *First Dark Matter Search Results from the Large Underground Xenon (LUX) Experiment.* 2014. arXiv: 1405.5906 [hep-ex].

[125] G. Bélanger et al. "Dark matter direct detection rate in a generic model with micrOMEGAs_2.2". In: *Computer Physics Communications* 180.5 (May 2009), pp. 747–767. DOI: 10.1016/j.cpc.2008.11.019. URL: https://doi.org/10.1016%2Fj.cpc.2008.11.019.

[126] E. Aprile et al. "Design and performance of the XENON10 dark matter experiment". In: *Astroparticle Physics* 34.9 (Apr. 2011), pp. 679–698. DOI: `10.1016/j.astropartphys.2011.01.006`. URL: `https://doi.org/10.1016%2Fj.astropartphys.2011.01.006`.

[127] Rouven Essig et al. "First Direct Detection Limits on Sub-GeV Dark Matter from XENON10". In: *Physical Review Letters* 109.2 (July 2012). DOI: `10.1103/physrevlett.109.021301`. URL: `https://doi.org/10.1103%2Fphysrevlett.109.021301`.

[128] Tadayoshi Doke et al. "Absolute Scintillation Yields in Liquid Argon and Xenon for Various Particles". In: *Jap. J. Appl. Phys.* 41 (2002), pp. 1538–1545. DOI: `10.1143/JJAP.41.1538`.

[129] E. Aprile et al. "Observation of anticorrelation between scintillation and ionization for MeV gamma rays in liquid xenon". In: *Physical Review B* 76.1 (July 2007). DOI: `10.1103/physrevb.76.014115`. URL: `https://doi.org/10.1103%2Fphysrevb.76.014115`.

[130] Carl Eric Dahl. "The physics of background discrimination in liquid xenon, and first results from Xenon10 in the hunt for WIMP dark matter". PhD thesis. Princeton U., 2009.

[131] Peter Sorensen and Carl Eric Dahl. "Nuclear recoil energy scale in liquid xenon with application to the direct detection of dark matter". In: *Physical Review D* 83.6 (Mar. 2011). DOI: `10.1103/physrevd.83.063501`. URL: `https://doi.org/10.1103%2Fphysrevd.83.063501`.

[132] T. Shutt et al. "Performance and fundamental processes at low energy in a two-phase liquid xenon dark matter detector". In: *Nuclear Instruments and Methods in Physics Research Section A: Accelerators, Spectrometers, Detectors and Associated Equipment* 579.1 (Aug. 2007), pp. 451–453. DOI: `10.1016/j.nima.2007.04.104`. URL: `https://doi.org/10.1016%2Fj.nima.2007.04.104`.

[133] Rouven Essig, Tomer Volansky, and Tien-Tien Yu. "New constraints and prospects for sub-GeV dark matter scattering off electrons in xenon". In: *Physical Review D* 96.4 (Aug. 2017). DOI: `10.1103/physrevd.96.043017`. URL: `https://doi.org/10.1103%2Fphysrevd.96.043017`.

[134] E Aprile et al. "Observation and applications of single-electron charge signals in the XENON100 experiment". In: *Journal of Physics G: Nuclear and Particle Physics* 41.3 (Feb. 2014), p. 035201. DOI: `10.1088/0954-3899/41/3/035201`. URL: `https://doi.org/10.1088%2F0954-3899%2F41%2F3%2F035201`.

[135] E. Aprile et al. "XENON1T dark matter data analysis: Signal and background models and statistical inference". In: *Physical Review D* 99.11 (June 2019). DOI: `10.1103/physrevd.99.112009`. URL: `https://doi.org/10.1103%2Fphysrevd.99.112009`.

[136] Rouven Essig et al. "Relation between the Migdal Effect and Dark Matter-Electron Scattering in Isolated Atoms and Semiconductors". In: *Physical Review Letters* 124.2 (Jan. 2020). DOI: `10.1103/physrevlett.124.021801`. URL: `https://doi.org/10.1103%2Fphysrevlett.124.021801`.

[137] Marco Fabbrichesi, Emidio Gabrielli, and Gaia Lanfranchi. "The Physics of the Dark Photon". In: *SpringerBriefs in Physics* (2021). ISSN: 2191-5431. DOI: `10.1007/978-3-030-62519-1`. URL: `http://dx.doi.org/10.1007/978-3-030-62519-1`.

[138] Olaf Kaczmarek et al. *QCD phase transition in the chiral limit.* 2020. arXiv: `2003.07920 [hep-lat]`.

[139] R. L. Workman et al. "Review of Particle Physics". In: *PTEP* 2022 (2022), p. 083C01. DOI: `10.1093/ptep/ptac097`.

[140] Asher Berlin, Dan Hooper, and Samuel D. McDermott. "Simplified dark matter models for the Galactic Center gamma-ray excess". In: *Physical Review D* 89.11 (June 2014). DOI: `10.1103/physrevd.89.115022`. URL: `https://doi.org/10.1103%2Fphysrevd.89.115022`.

[141] Daniel Feldman et al. "Multicomponent dark matter in supersymmetric hidden sector extensions". In: *Physical Review D* 81.9 (May 2010). DOI: `10.1103/physrevd.81.095017`. URL: `https://doi.org/10.1103%2Fphysrevd.81.095017`.

[142] The BaBar Collaboration and B. Aubert. *Search for Invisible Decays of a Light Scalar in Radiative Transitions Upsilon(3S) -> gamma A0.* 2008. arXiv: `0808.0017 [hep-ex]`.

[143] Rouven Essig et al. "Constraining light dark matter with low-energy e+e- colliders". In: *Journal of High Energy Physics* 2013.11 (Nov. 2013). DOI: `10.1007/jhep11(2013)167`. URL: `https://doi.org/10.1007%2Fjhep11%282013%29167`.

[144] Eder Izaguirre et al. "New electron beam-dump experiments to search for MeV to few-GeV dark matter". In: *Physical Review D* 88.11 (Dec. 2013). DOI: `10.1103/physrevd.88.114015`. URL: `https://doi.org/10.1103%2Fphysrevd.88.114015`.

[145] David Curtin et al. "Illuminating dark photons with high-energy colliders". In: *Journal of High Energy Physics* 2015.2 (Feb. 2015). DOI: `10.1007/jhep02(2015)157`. URL: `https://doi.org/10.1007%2Fjhep02%282015%29157`.

[146] Anson Hook, Eder Izaguirre, and Jay G. Wacker. *Model Independent Bounds on Kinetic Mixing*. 2010. arXiv: `1006.0973 [hep-ph]`.

[147] Scott W. Randall et al. "Constraints on the Self-Interaction Cross Section of Dark Matter from Numerical Simulations of the Merging Galaxy Cluster 1E 0657-56". In: *The Astrophysical Journal* 679.2 (June 2008), pp. 1173–1180. DOI: `10.1086/587859`. URL: `https://doi.org/10.1086%2F587859`.

[148] Hooman Davoudiasl and William J. Marciano. "Running of the U(1) coupling in the dark sector". In: *Physical Review D* 92.3 (Aug. 2015). DOI: `10.1103/physrevd.92.035008`. URL: `https://doi.org/10.1103%2Fphysrevd.92.035008`.

[149] Marco Fabbrichesi, Emidio Gabrielli, and Gaia Lanfranchi. *The Physics of the Dark Photon*. Springer International Publishing, 2021. DOI: `10.1007/978-3-030-62519-1`. URL: `https://doi.org/10.1007%2F978-3-030-62519-1`.